JAEA-Review
2011-040

JAEA-Review

JAEA-Tokai Tandem Annual Report 2010
April 1, 2010 – March 31, 2011

Department of Research Reactor and Tandem Accelerator

Nuclear Science Research Institute
Tokai Research and Development Center

December 2011

Japan Atomic Energy Agency | 日本原子力研究開発機構

本レポートは独立行政法人日本原子力研究開発機構が不定期に発行する成果報告書です。
本レポートの入手並びに著作権利用に関するお問い合わせは、下記あてにお問い合わせ下さい。
なお、本レポートの全文は日本原子力研究開発機構ホームページ（http://www.jaea.go.jp）
より発信されています。

独立行政法人日本原子力研究開発機構　研究技術情報部　研究技術情報課
〒319-1195　茨城県那珂郡東海村白方白根 2 番地 4
電話 029-282-6387, Fax 029-282-5920, E-mail:ird-support@jaea.go.jp

This report is issued irregularly by Japan Atomic Energy Agency
Inquiries about availability and/or copyright of this report should be addressed to
Intellectual Resources Section, Intellectual Resources Department,
Japan Atomic Energy Agency
2-4 Shirakata Shirane, Tokai-mura, Naka-gun, Ibaraki-ken 319-1195 Japan
Tel +81-29-282-6387, Fax +81-29-282-5920, E-mail:ird-support@jaea.go.jp

JAEA-Review 2011-040

JAEA-Tokai Tandem Annual Report 2010
April 1, 2010 – March 31, 2011

Department of Research Reactor and Tandem Accelerator

Nuclear Science Research Institute
Tokai Research and Development Center
Japan Atomic Energy Agency
Tokai-mura, Naka-gun, Ibaraki-ken

(Received October 20, 2011)

The JAEA-Tokai tandem accelerator complex has been used in various research fields such as nuclear science and material science by researchers not only of JAEA but also from universities, research institutes and industrial companies. This annual report covers developments of accelerators and research activities carried out using the tandem accelerator, superconducting booster, and radioactive nuclear beam accelerator, from April 1, 2010 to March 31, 2011. Thirty-six summary reports were categorized into seven research/development fields:

(1) accelerator operation and development
(2) nuclear structure
(3) nuclear reaction
(4) nuclear chemistry
(5) nuclear theory
(6) atomic physics and solid state physics
(7) radiation effects in materials.

This report also lists publications, meetings, personnel, committee members, cooperative researches and common use programs.

Keywords : JAEA-Tokai Tandem Accelerator, Operation Results, Nuclear Structure, Nuclear Reaction, Nuclear Chemistry, Nuclear Theory, Atomic Physics, Solid State Physics, Radiation Effects in Materials, Progress Report

---

Editors: Makoto MATSUDA, Satoshi CHIBA, Norito ISHIKAWA, Shin-ichi MITSUOKA, Yosuke TOH, Kazuaki TSUKADA and Suehiro TAKEUCHI

JAEA-Review 2011-040

原子力機構東海タンデム加速器2010年度年次報告

日本原子力研究開発機構
東海研究開発センター原子力科学研究所
研究炉加速器管理部

(2011年10月 20日受理)

原子力機構東海タンデム加速器施設は、原子核科学や物質科学などの様々な分野において、原子力機構を始めとして、大学や公立研究機関、民間企業に利用されている。本年次報告書は、タンデム加速器、ブースター加速器、放射性核種加速装置を利用し、2010年4月1日から2011年3月31日までの期間に実施された研究活動の英文要約をまとめたものである。総数36件の要約を下記の7部門に分類した。

（1）加速器の運転状況と開発
（2）原子核構造
（3）原子核反応
（4）核化学
（5）原子核理論
（6）原子物理及び固体物理
（7）材料の照射効果

また、発表論文と会議での口頭発表、タンデム加速器に関与した職員、タンデム加速器専門部会委員、大学等との共同研究課題、及び施設共用課題のリストを掲載した。

原子力科学研究所：〒319-1195　茨城県那珂郡東海村白方白根2-4
編集者：松田　誠、千葉　敏、石川　法人、光岡　真一、藤　暢輔、塚田　和明、
竹内　末広

Foreword

This report covers research and development activities with the tandem accelerator, its superconducting booster and TRIAC radioactive ion accelerator at JAEA Tokai, for the period of FY 2010 (April 1, 2010 to March 31, 2011). The tandem accelerator was operated over a total of 171 days and delivered 27 different ion beams to experiments in the fields of nuclear physics, nuclear chemistry, atomic physics, solid state physics and radiation effects in materials. A massive earthquake of magnitude 9.0, named *"The 2011 off the Pacific coast of Tohoku Earthquake",* hit us on March 11. The accelerator building quaked at a magnitude of 1000 gal on the top floor. The accelerator column withstood the earthquake with the help of quake-absorbers attached to its bottom, and no acceleration tubes were damaged. However, about thirty column posts out of 240 had a crack, a vacuum leak happened at the terminal ion source, and the beam line of the booster lost its proper alignment (†).

The following are the highlights in FY 2010:
In the field of accelerator development: A xenon beam of 1.3 GeV was accelerated by the tandem accelerator with the terminal voltage of 18.5 MV and the booster. This terminal voltage was the highest value the tandem accelerator ever had with beam. Carbon cluster beams of C_2^+, C_3^+ and C_4^+ were accelerated from the in-terminal ECR ion source. Hydrogen analysis by the NRA method was demonstrated by using a low energy ^{15}N beam.

With the TRIAC, an experiment of Coulomb excitation of a stable ^{130}Ba nucleus at 1.1 MeV/nucleon was successfully performed as a test of all equipments. At the charge breeder, residual activities of ^{111}In were measured to understand the process of the charge breeding with a mesh grid at the exit of the deceleration electrode. TRIAC is scheduled to move out of the tandem building at the end of 2011. New beam lines of the tandem accelerator, which will be placed at the accelerator room of TRIAC, were designed, and a switching magnet and other beam-line components for these lines were prepared.

In the field of nuclear structure: The property of the N=126 magic number at far off the β-stability line was studied by searching for a very proton-rich nucleus of ^{216}U. Using the ^{138}Ba (^{82}Kr, 4n) ^{216}U reaction and the recoil mass separator, an upper-limit cross-section of 65 pb for ^{216}U was obtained. In order to study single-particle states in very heavy nuclei, an alpha fine-structure measurement was developed. The assignment of spin-parities and single-particle configurations to levels in ^{253}Fm was demonstrated through this measurement.

In the field of nuclear reactions: The reaction mechanism for the synthesis of super-heavy nuclei has been studied. By measuring the fission fragment properties in the $^{48}Ca + ^{238}U$ reaction, the excitation function of the fusion probability was determined. This helps the fluctuation dissipation model to estimate the cross section for the super-heavy production.

In the field of nuclear chemistry: Mendelevium was successfully reduced from Md^{3+} to Md^{2+} on an atom-at-a-time scale and the redox potential of Md was determined to be -0.18 ± 0.03 V. A new program to determine the 1st ionization potential of Lr has been started using the surface ionization comparison technique. The basic research on the production and purification of radioisotopes, ^{95m}Tc and ^{211}At, for medical use has been conducted.

In the field of nuclear theory: A new dynamical model to describe the whole process of surrogate reactions, namely, the nucleon transfer, formation of compound nuclei and their decay, was completed. By using this model, it became possible to investigate spin and mass distributions of compound nuclei populated in surrogate reactions. Furthermore, a new computational algorithm was developed to overcome difficulty in treating large model-space in the Monte Carlo shell model.

In the field of atomic physics and solid-state physics: Equilibrium and non-equilibrium charge state distributions were measured for penetration of 2 MeV/u C^{q+} (q=2-6) ions through 0.9-100 μ g/cm^2 in thickness. Electronic sputtering yields (Ye) for CuO by swift heavy ions were measured. The Ye were much larger than those for Cu_2O and exceptionally close to liner dependence on electronic stopping power.

In the field of radiation effects in materials: Elongation of metal nanoparticles (NPs) due to irradiation of swift heavy ions was studied. This result suggests that the overlap of ion-tracks does not play an important role in the elongation of Zn NPs in silica, and the creation of single ion-track can induce the elongation. The damage evolution of UO_2 irradiated with high energy fission fragments was characterized by X-ray diffraction (XRD) analysis. The detection of the radiation damage by XRD at relatively low fluence of 10^{12} Xe-ions/cm^2 can be explained by the introduction of nm-sized ion-tracks. It was found that the occupancy of ion-tracks in the specimen affects the damage behavior.

(†) The tandem accelerator recovered and opened for experiment on September 15, 2011. We would like to express sincere thanks for your kind support and encouragement in this severe time.

Tetsuro Ishii

Tetsuro ISHII, Deputy Director, Department of Research Reactor and Tandem Accelerator

Contents

1. ACCELERATOR OPERATION AND DEVELOPMENT ····· 1
1.1 Operation and usage of tandem accelerator and booster ····· 3
A. Osa, Y. Tsukihashi, S. Hanashima, S. Abe, T. Ishii, N. Ishizaki, H. Tayama, M. Matsuda, T. Nakanoya, H. Kabumoto, M. Nakamura, K. Kutsukake, Y. Otokawa and T. Asozu
1.2 KEK-JAEA joint RNB project ····· 5
S.C. Jeong on behalf of TRIAC collaboration
1.3 Design of the new beam lines ····· 7
T. Asozu, H. Kabumoto and N. Ishizaki
1.4 Preliminary experiment of the hydrogen analysis by the NRA method using ^{15}N beam from TIS ····· 9
M. Matsuda, T. Asozu, M. Nakamura and M. Sataka

2. NUCLEAR STRUCTURE ····· 11
2.1 In-beam γ-ray spectroscopy of neutron-deficient actinide nuclei using heavy-ion induced transfer reactions ····· 13
M. Asai, T. Ishii, R. Takahashi, H. Makii, K. Tsukada and N. Sato
2.2 Development of a gas cell for on-line laser spectroscopy of refractory elements ····· 14
H. Iimura, M. Koizumi, M. Miyabe and M. Oba
2.3 Development of high-resolution α fine-structure spectroscopy for the heaviest nuclei ····· 16
M. Asai, Y. Shima, N. Sato, K. Tsukada, A. Toyoshima, T.K. Sato, T. Ishii and M. Shibata
2.4 Coulomb excitation experiment of ^{126}Xe ····· 18
M. Koizumi, Y. Toh, A. Kimura, Y. Hatsukawa, K. Furutaka, H. Harada, F. Kitatani, S. Nakamura, M. Sugawara and E. Ideguchi
2.5 Experiment for synthesis of a new isotope ^{216}U ····· 20
Y. Wakabayashi, K. Nishio, S. Mitsuoka, I. Nishinaka, H. Makii, R. Takahashi, S. Yan and H. Miyatake
2.6 Development of an electrodeposited target for a surrogate reaction ····· 22
T. Ishii, H. Makii, I. Nishinaka, M. Asai, K. Tsukada and R. Takahashi
2.7 Development of spin-polarized radioactive nuclear beam for nuclear spectroscopy through β-delayed decay of spin-polarized nuclei around doubly magic nucleus ^{132}Sn ····· 24
Y. Hirayama, M. Mihara, Y.X. Watanabe, N. Imai, S.C. Jeong, K. Matsuta, H. Miyatake, S. Momota, H. Ishiyama, T. Izumikawa, I. Nishinaka, K. Nishio, H. Makii, S. Mitsuoka, Y. Otokawa, T.K. Sato and Y. Wakabayashi

3. NUCLEAR REACTION ····· 27
3.1 Influence of the reaction Q-value on heavy-ion induced fission ····· 29
K. Nishio, S. Mitsuoka, I. Nishinaka, H. Makii, Y. Wakabayashi, H. Ikezoe,

T. Ohtsuki and K. Hirose

3.2 Fission fragment anisotropy in heavy-ion-induced fission of actinides ····· 31

I. Nishinaka, K. Nishio, M. Tanikawa, H. Makii, S. Mitsuoka,
Y. Wakabayashi and A. Yokoyama

3.3 Measurement of the $^{12}C(\alpha,\gamma)^{16}O$ cross sections by using TRIAC ····· 33

H. Makii, H. Miyatake, Y. Wakabayashi, K. Niki, M. Okada,
H. Ishiyama, Y. Hirayama, N. Imai, S.C. Jeong, T. Shima,
S. Mitsuoka, K. Nishio, I. Nishinaka and S. Chiba

3.4 Development of Si ΔE-E detector for detection of light ions ····· 35

H. Makii, T. Ishii, R. Takahashi, Y. Wakabayashi, I. Nishinaka, S. Mitsuoka,
S. Chiba, H. Miyatake, S.C. Jeong, N. Imai and Y. Hirayama

4. NUCLEAR CHEMISTRY ····· 37

4.1 Determination of the reduction potential of mendelevium between 2+ and 3+ states using an electrochemistry apparatus ····· 39

A. Toyoshima, M. Asai, Z.J. Li, N. Sato, T.K. Sato, K. Ooe, T. Kikuchi,
Y. Kaneya, Y. Kitatsuji, K. Tsukada, Y. Nagame, M. Schädel, Y. Kasamatsu,
Y. Kogama, A. Shinohara, H. Haba and J. Even

4.2 Development of a surface-ionization-type ion-source for the measurement of the first ionization potential of Lr ····· 41

N. Sato, T.K. Sato, M. Asai, S. Ichikawa, K. Tsukada, A. Toyoshima,
Z.J. Li, T. Kikuchi, Y. Kaneya, Y. Nagame and M. Schädel

4.3 On-line isothermal gas chromatographic behavior of group-5 elements as homologues of Db ····· 43

T.K. Sato, K. Tsukada, M. Asai, A. Toyoshima, Y. Kasamatsu,
Z.J. Li, N. Sato, T. Kikuchi, Y. Nagame and M. Schädel

4.4 Studies on volatile behavior of Zr and Hf chlorides ····· 45

S. Goto, H. Murayama, T. Kojima, M. Murakami, H. Kudo,
K. Tsukada, M. Asai, T.K. Sato, N. Sato, A. Toyoshima and Y. Nagame

4.5 Anion-exchange behavior of the group-6 elements in HF/HNO_3 mixed solutions - Towards the study of ion-exchange behavior of $_{106}Sg$ - ····· 46

X.H. Liang, K. Tsukada, Z.J. Li, A. Toyoshima, M. Asai,
T.K. Sato, N. Sato, T. Kikuchi, Y. Kaneya and Y. Nagame

4.6 Solvent extraction of Bk and Md into HDEHP from HNO_3 solution ····· 48

Y. Kasamatsu, Y. Kogama, R. Takayama, H. Kikunaga, A. Toyoshima,
K. Tsukada, M. Asai, T.K. Sato, Z.J. Li, N. Sato, T. Kikuchi, Y. Kaneya,
Y. Nagame, K. Ooe, Y. Komori, T. Yoshimura, N. Takahashi and A. Shinohara

4.7 Production of radioactive astatine isotopes using lithium ion beams ····· 50

I. Nishinaka, A. Yokoyama, K. Washiyama, R. Amano,
N. Yamada, R. Ishiguro, H. Makii and K. Hashimoto

4.8 Production of medical radio isotopes ^{95m}Tc ····· 52
Y. Hatsukawa, K. Hashimoto, K. Tsukada, M. Asai, T.K. Sato, T. Kin and Y. Nagai

5. NUCLEAR THEORY ····· 55
5.1 Methodological and technical development in the Monte Carlo shell model ····· 57
Y. Utsuno, N. Shimizu, T. Otsuka, T. Abe, T. Mizusaki and M. Honma
5.2 Calculation of fission barrier in the heavy and superheavy mass region by using a spherical-basis method ····· 59
H. Koura
5.3 Spin and mass distributions of compound nucleus in surrogate reaction ····· 61
Y. Aritomo, S. Chiba and K. Nishio
5.4 Analysis of various cross sections in deuteron induced reaction with CDCC and eikonal reaction theory ····· 63
S. Hashimoto, M. Yahiro, K. Ogata, K. Minomo and S. Chiba

6. ATOMIC PHYSICS AND SOLID STATE PHYSICS ····· 65
6.1 Charge state distribution of carbon ions after penetration of C-foil targets ····· 67
M. Imai, M. Sataka, H. Sugai, K. Kawatsura, K. Takahiro, K. Komaki, K. Nishio and H. Shibata
6.2 Electronic sputtering of CuO films by high-energy ions ····· 69
N. Matsunami, M. Sataka, S. Okayasu and H. Kakiuchida

7. RADIATION EFFECTS IN MATERIALS ····· 71
7.1 Radiation damage of crystal structure in UO_2 irradiated with high-energy heavy ions ····· 73
N. Ishikawa, T. Sonoda, T. Sawabe and A. Iwase
7.2 Study on effects of energetic ion irradiation in Gd_2O_3-doped CeO_2 by means of synchrotron radiation X-ray spectroscopy ····· 75
Y. Tahara, K. Shimizu, N. Ishikawa, Y. Okamoto, F. Hori, T. Matsui and A. Iwase
7.3 Change in magnetic properties of CeO_2 by swift heavy ion irradiation ····· 77
K. Shimizu, S. Kosugi, Y. Tahara, K. Yasunaga, N. Ishikawa , Y. Okamoto , Y. Baba , N. Hirao, F. Hori , T. Matsui and A. Iwase
7.4 Shape and property control of Zn and ZnO nanoparticles by swift heavy ions ····· 79
H. Amekura, N. Ishikawa and N. Okubo
7.5 Radiation effects for film formation and nano-structural changes of iron disilicide thin film ····· 81
M. Sasase and S. Okayasu
7.6 Formation of metal microstructures induced by heavy ion irradiation in Ag-zeolite ····· 83
Y. Sasaki and S. Okayasu
7.7 Surface amorphization in single crystalline Al_2O_3 ····· 85
N. Okubo, N. Ishikawa, M. Sataka and S. Jitsukawa

8. PUBLICATION IN JOURNAL AND PROCEEDINGS, AND CONTRIBUTION TO SCIENTIFIC MEETINGS ····· 87
8.1 Accelerator Operation and Development ····· 89
8.2 Nuclear Structure ····· 91
8.3 Nuclear Reaction ····· 93
8.4 Nuclear Chemistry ····· 96
8.5 Nuclear Theory ····· 99
8.6 Atomic Physics and Solid-state Physics ····· 103
8.7 Radiation Effects in Materials ····· 104

9. PERSONNEL AND COMMITTEE ····· 107
9.1 Personnel ····· 109
9.2 Research Planning and Assessment Committee ····· 113

10. COOPERATIVE RESEARCHES AND COMMON USE IN JAEA ····· 115
10.1 Cooperative Research Programs ····· 117
10.2 Common Use Programs in JAEA ····· 119

目　　次

1. 加速器の運転状況及び開発 …… 1
1.1 タンデム加速器とブースターの運転及び利用状況 …… 3
長　明彦、月橋　芳廣、花島　進、阿部　信市、石井　哲朗、石崎　暢洋、田山　豪一、
松田　誠、仲野谷　孝充、株本　裕史、中村　暢彦、沓掛　健一、乙川　義憲、遊津　拓洋
1.2 KEK-JAEA 共同 RNB 計画 …… 5
TRIAC 共同研究代表　鄭 淳讃
1.3 新ビームラインの設計 …… 7
遊津　拓洋、株本　裕史、石崎　暢洋
1.4 TIS からの 15N ビームを用いた NRA 法による水素分析実験 …… 9
松田　誠、遊津　拓洋、中村　暢彦、左高　正雄

2. 原子核構造 …… 11
2.1 重イオン核子移行反応を用いた中性子欠損アクチノイド核のインビームγ線分光 …… 13
浅井　雅人、石井　哲朗、高橋　竜太、牧井　宏之、塚田　和明、佐藤　望

2.2 高融点元素のオンラインレーザー分光のためのガスセルの開発 …… 14
飯村　秀紀、小泉　光生、宮部　昌文、大場　正規
2.3 超重核を対象とした高分解能α線微細構造測定法の開発 …… 16
浅井　雅人、嶋　洋佑、佐藤　望、塚田　和明、豊嶋　厚史、
佐藤　哲也、石井　哲朗、柴田　理尋
2.4 ^{126}Xe のクーロン励起実験 …… 18
小泉　光生、藤　暢輔、木村 敦、初川　雄一、古高　和禎、原田　秀郎、
北谷　文人、中村　詔司、菅原　昌彦、井手口　栄治
2.5 新同位体 ^{216}U の合成実験 …… 20
若林　泰生、西尾　勝久、光岡　真一、西中　一朗、
牧井　宏之、高橋　竜太、S. Yan、宮武 宇也
2.6 代理反応のための電着標的の開発 …… 22
石井　哲朗、牧井　宏之、西中　一朗、浅井　雅人、
塚田　和明、高橋　竜太
2.7 核分光を目的とした核スピン偏極した ^{132}Sn 近傍核の開発 …… 24
平山　賀一、三原　基嗣、渡辺 裕、今井　伸明、鄭 淳讃、松多　建策、宮武 宇也、
百田　佐多生、石山　博恒、泉川　卓司、西中　一朗、西尾　勝久、牧井　宏之、
光岡　真一、乙川　義憲、佐藤　哲也、若林　泰生

3. 原子核反応 …… 27
3.1 重イオン入射核分裂反応における反応の Q 値の効果 …… 29
西尾　勝久、光岡　真一、西中　一朗、牧井　宏之、若林　泰生、
池添　博、大槻　勤、廣瀬　健太郎

3.2 アクチノイド重イオン誘起核分裂における核分裂片角度異方性 ……31
西中　一朗、西尾　勝久、谷川　勝至、牧井　宏之、
光岡　真一、若林　泰生、横山　明彦
3.3 TRIAC を用いた $^{12}C(\alpha,\gamma)^{16}O$ 反応断面積測定 ……33
牧井　宏之、宮武　宇也、若林　泰生、仁木　和昭、岡田　雅之、石山　博恒、平山　賀一、
今井　伸明、鄭　淳讃、嶋　達志、光岡　真一、西尾　勝久、西中　一朗、千葉　敏
3.4 軽イオン観測用 Si ΔE-E 検出器の開発 ……35
牧井　宏之、石井　哲朗、高橋　竜太、若林　泰生、西中　一朗、光岡　真一、
千葉　敏、宮武　宇也、鄭　淳讃、今井　伸明、平山　賀一

4. 核化学 ……37
4.1 電気化学的手法によるメンデレビウムの還元電位測定 ……39
豊嶋　厚史、浅井　雅人、李　子杰、佐藤　望、佐藤　哲也、大江　一弘、
菊池　貴宏、金谷　佑亮、北辻　章浩、塚田　和明、永目　諭一郎、M. Schädel、
笠松　良崇、舘　優香、篠原　厚、羽場　宏光、J. Even
4.2 Lr のイオン化電位測定に向けた表面電離イオン源開発 ……41
佐藤　望、佐藤　哲也、浅井　雅人、市川　進一、塚田　和明、豊嶋　厚史、
李　子杰、菊池　貴宏、金谷　佑亮、永目　諭一郎、M. Schädel
4.3 Db を模擬した 5 族元素 Nb，Ta のオンライン等温ガスクロマトグラフ挙動 ……43
佐藤　哲也、塚田　和明、浅井　雅人、豊嶋　厚史、笠松　良崇、
李　子杰、佐藤　望、菊池　貴宏、永目　諭一郎、M. Schädel
4.4 Zr および Hf 塩化物の揮発挙動に関する研究 ……45
後藤　真一、村山　裕史、小嶋　貴幸、村上　昌史、工藤　久昭、
塚田　和明、浅井　雅人、佐藤　哲也、佐藤　望、豊嶋　厚史、永目　諭一郎
4.5 フッ化水素酸・硝酸混合水溶液系における 6 族元素の陰イオン交換挙動
－ ^{106}Sg のイオン交換挙動研究に向けて － ……46
梁　小虎、塚田　和明、李　子杰、豊嶋　厚史、浅井　雅人、佐藤　哲也、
佐藤　望、菊池　貴宏、金谷　祐亮、永目　諭一郎
4.6 HDEHP/HNO_3 系における Bk と Md の溶媒抽出挙動 ……48
笠松　良崇、舘　優香、高山　玲央奈、菊永　英寿、豊嶋　厚史、塚田　和明、
浅井　雅人、佐藤　哲也、李　子杰、佐藤　望、菊池　貴宏、金谷　祐亮、
永目　諭一郎、大江　一弘、小森　有希子、吉村　崇、高橋　成人、篠原　厚
4.7 リチウムイオンビームによる放射性アスタチン同位体の合成 ……50
西中　一朗、横山　明彦、鷲山　幸信、天野　良平、
山田　紀大、石黒　梨花、牧井　宏之、橋本　和幸
4.8 医療用放射性同位体 $^{9.5m}$Tc の製造 ……52
初川　雄一、橋本　和幸、塚田　和明、浅井　雅人、佐藤　哲也、金　政浩、永井　泰樹

5. 原子核理論 ……55
5.1 モンテカルロ殻模型における方法論的および技術的進展 ……57
宇都野　穣、清水　則孝、大塚　孝治、阿部　喬、水崎　高浩、本間　道雄

5.2 球形基底法を用いた重・超重核領域の核分裂障壁の計算 …… 59
小浦 寛之
5.3 代理反応によって生成された複合核のスピン分布および分裂片の質量分布 …… 61
有友 嘉浩、千葉 敏、西尾 勝久
5.4 離散化チャネル結合法とアイコナール反応理論を用いた
重陽子入射反応における様々な断面積の解析 …… 63
橋本 慎太郎、八尋 正信、緒方 一介、蓑茂 工将、千葉 敏

6. 原子物理及び固体物理 …… 65
6.1 炭素薄膜透過後の炭素イオン電荷分布 …… 67
今井 誠、左高 正雄、須貝 宏行、川面 澄、高廣 克己、
小牧 研一郎、西尾 勝久、柴田 裕実
6.2 高エネルギーイオン照射による Cu0 の電子励起スパッタリング …… 69
松波 紀明、左高 正雄、岡安 悟、垣内田 洋

7. 材料の照射効果 …… 71
7.1 高エネルギー重イオン照射した UO_2 の結晶構造に対する照射損傷 …… 73
石川 法人、園田 健、澤部 孝史、岩瀬 彰宏
7.2 放射光 X 線分光法を用いたガドリニア添加セリアの
高エネルギーイオン照射効果 …… 75
田原 佑規、清水 浩貴、石川 法人、岡本 芳浩、堀 史説、松井 利之、岩瀬 彰宏
7.3 高エネルギーイオン照射を用いた CeO_2 の磁性変化 …… 77
清水 浩貴、小杉 晋也、田原 佑規、安永 和史、石川 法人、岡本 芳浩、
馬場 祐治、平尾 法恵、堀 史説、松井 利之、岩瀬 彰宏
7.4 高速重イオン照射による Zn 系ナノ粒子の形状・物性制御 …… 79
雨倉 宏、石川 法人、大久保 成彰
7.5 鉄シリサイド薄膜に及ぼすイオン照射効果 …… 81
笹瀬 雅人、岡安 悟
7.6 Ag-ゼオライトへの重イオン照射による金属微小構造形成 …… 83
佐々木 優吉、岡安 悟
7.7 単結晶 Al_2O_3 における表面非晶質化 …… 85
大久保 成彰、石川 法人、左高 正雄、實川 資朗

8. 雑誌及び国際会議等の刊行物、学会発表 …… 87
8.1 加速器の運転状況及び開発 …… 89
8.2 原子核構造 …… 91
8.3 原子核反応 …… 93
8.4 核化学 …… 96
8.5 原子核理論 …… 99
8.6 原子物理及び固体物理 …… 103
8.7 材料の照射効果 …… 104

9. 関連課室職員及び委員会 …… 107
9.1 課室職員 …… 109
9.2 委員会 …… 113

10. 共同研究及び施設供用 …… 115
10.1 共同研究課題 …… 117
10.2 施設供用課題 …… 119

CHAPTER 1

Accelerator Operation and Development

1.1 Operation and usage of tandem accelerator and booster
1.2 KEK-JAEA joint RNB project
1.3 Design of the new beam lines
1.4 Preliminary experiment of the hydrogen analysis

This is a blank page.

1.1 Operation and usage of tandem accelerator and booster

A. Osa[1], Y. Tsukihashi[1], S. Hanashima[1], S. Abe[1], T. Ishii[1], N. Ishizaki[1], H. Tayama[1], M. Matsuda[1], T. Nakanoya[1], H. Kabumoto[1], M. Nakamura[1], K. Kutsukake[1], Y. Otokawa[1] and T. Asozu[1]

The tandem accelerator and booster were operated for experiments from June 7, 2010 to September 28, 2010, from December 1, 2010 to January 26, 2011 and from March 7, 2011 to March 10, 2011. The last beam time was terminated by the Great Eastern Japan Earthquake on March 11, 2011. The total operation time of the tandem accelerator for FY2010 (from April 1, 2010 to March 31, 2011) was 171 days and 27 different beams were delivered for experiments. The experimental proposal and the usage of the beam times for FY2010 are summarized in Table 1 and Table 2, respectively.

In FY 2010, the terminal voltage with beam was improved to 18.5 MV which was highest value this tandem accelerator has ever had. In this condition, we accelerated and boosted xenon ions up to 1314 MeV. Carbon cluster beams C_2^+, C_3^+ and C_4^+ were accelerated from the in-terminal 14.5-GHz ECR ion source.

Table 1. Experimental proposals.

Research proposals accepted by the program advisory committee:	
In-house staff proposals	6
Collaboration proposals	14
Number of experiments proposed	75
Total number of scientists participating in research	
from outside	219
in-house	381
Number of institutions presented	31

Table 2. Usage of beam-times in different research fields.

Research field	Beam time (days)	(%)
Nuclear physics	47	27.5
Nuclear chemistry	55	32.2
Atomic and materials sciences	48	28.1
Accelerator development	21	12.3
total	171	100

Distributions of the terminal voltages and ion species for experiments are shown in Fig.1 and Fig.2, respectively. Half of the beams were extracted from three negative ion sources, SNICS-2. The proton beam and multiply charged ion beams of helium-3, carbon, nitrogen, oxygen and rare gases were ionized and extracted from in-terminal ECR ion source. The ECR ion source was used as much as 48% of all the beam time.

The super-conducting booster was operated for a total of 24 days to boost the energies of 6 different beams from the tandem accelerator, as is summarized in Table 3. These beams were used for experiments of nuclear physics and accelerator development.

The proton, ^{7}Li and ^{19}F beams were supplied to the TRIAC (Tokai Radioactive Ion Accelerator Complex) experiments for 14 days. The radioactive ^{8}Li, ^{111}In and ^{142}Ba were ionized and separated by the ISOL and injected into the TRIAC.

[1] Japan Atomic Energy Agency (JAEA)

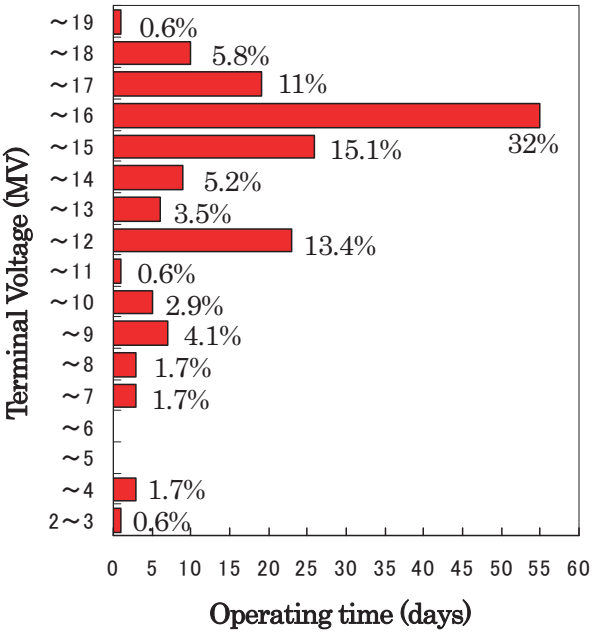

Fig. 1 Distribution of terminal voltages.

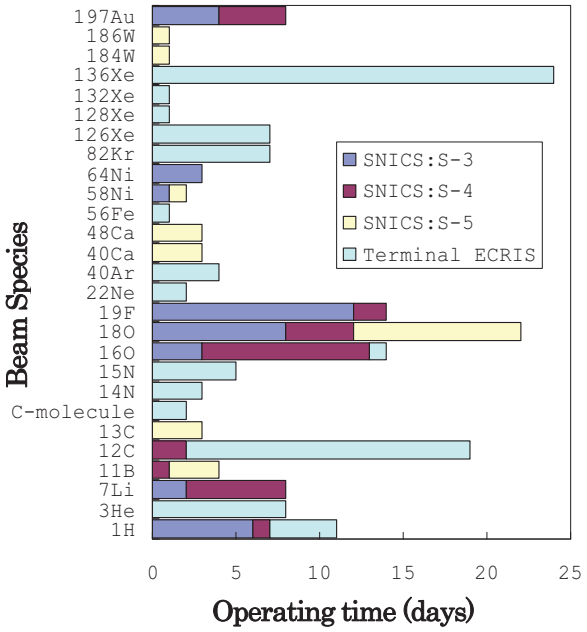

Fig. 2 Distribution of beam species accelerated for experiments.

Table 3. Boosted ion beams for experiments.

Beam species	Boosted energies (MeV)	Beam time (days)
^{40}Ca	212.8-270.9(9 energy points)	3
^{48}Ca	297	4
^{64}Ni	368	3
^{82}Kr	378	7
^{126}Xe	385	3
	544	3
^{136}Xe	1314	1

1.2 KEK-JAEA joint RNB project

S.C. Jeong[1] on behalf of TRIAC collaboration

The Tokai Radioactive Ion Accelerator Complex (TRIAC) is operating for nuclear physics and materials science experiments at JAEA-Tokai tandem accelerator facility under collaboration between KEK and JAEA (TRIAC collaboration). Produced by the proton-induced fission reactions of ^{nat}UC, the radioactive ions (RIs) were extracted and mass-separated as singly charged ions by the isotope separator on-line (ISOL) of JAEA. They were charge-bred to higher charge states with a charge-to-mass ratios of about 1/7 using charge breeding electron cyclotron resonance ion source (CB-ECRIS) called as KEKCB. And then, the charge-bred RIs were accelerated by using a series of heavy ion linacs, the split-coaxial radiofrequency quadrupole (SCRFQ) and the inter-digital H (IH) linacs. In FY 2010, we performed two experiments as R&D of TRIAC. First one is the Coulomb excitation measurement with stable nucleus ^{130}Ba at 1.1 MeV/*A*. The other one is the injection of ^{111}In into KEKCB to explore the origin of small charge breeding efficiencies for metallic ions. The following experiments were carried out in FY2010: (1) Direct exclusive measurement of ^{8}Li(α,n) reaction at astrophysical energies (RNB08-K05). (2) Production of polarized medium-mass RI by the tilted foil method (RNB08-K02/K03). (3) Measurement of the cross section of ^{12}C(α,γ) reaction (RNB09-KJ04). Some details of the experiments can be found in this report.

In the experiment named RNB09-KJ03, Coulomb excitation measurement of ^{142}Ba had been proposed to determine the **B** (*E2;*$2^+ \rightarrow 0^+$) value in a rather direct way in order to settle down the inconsistency of the value raised by the recent lifetime measurement of the first 2^+ sate. The TRIAC can accelerate RIs extracted by the JAEA-ISOL up to 1.1 MeV/nucleon, which is far below the Coulomb barrier. Thus, the cascade transition would be negligible since the probability of multi-step excitation should be very small. As a test of the whole experimental system including charge-breeding by the KEKCB, we performed an experiment of Coulomb excitation with a stable ^{130}Ba beam of 1.1 MeV/nucleon. The energy of 2^+_1 state of ^{130}Ba is 359 keV, which is close to the 357 keV for ^{142}Ba. Therefore, the present experiment could well simulate the very measurement of ^{142}Ba. A $^{130}Ba^{1+}$ beam was supplied by the JAEA-ISOL using the enriched $BaCO_3$. Typical beam intensity was about 30 *e*nA. The beam was injected into the KEKCB for charge-breeding the singly charged $^{130}Ba^{1+}$ to multi-charged $^{130}Ba^{19+}$. The charge breeding efficiency achieved was around 1%.

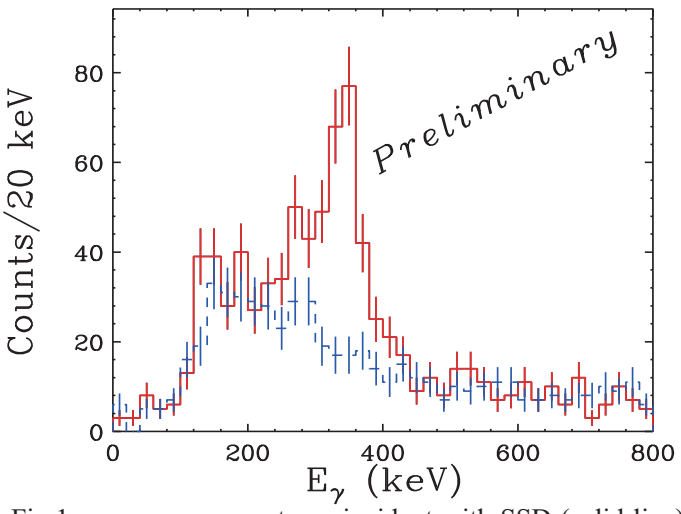

Fig.1 γ ray energy spectra coincident with SSD (solid line) and accidentally coincident with SSD (dashed line).

[1] High Energy Accelerator Research Organization(KEK), corresponding author: N. Imai

The $^{130}Ba^{19+}$ beam was transported to post-accelerators of the TRIAC and accelerated to 1.1 MeV/nucleon. At the final focal plane of the TRIAC, a secondary target of 2-μm thick ^{nat}V was placed and irradiated by the beam. Six NaI(Tl) detectors of 9 x 9 x 18 cm^3 were placed to detect the de-excitation γ rays from the excited ^{130}Ba around the target. The NaI(Tl)s were mounted in the 2-cm thick lead box to suppress the background γ rays or X rays. To measure the recoiled particles, an annular-type silicon solid-sate detector (SSD) was placed 13-cm downstream of the target. The detector covered from 13 to 26° in the laboratory frame, which corresponded to angles from 48 to 160° in the center of mass frame. Figure 1 shows two γ-ray energy spectra measured by three NaI(Tl) detectors with different timing gates. Solid line indicates the γ rays which were coincident with the SSD, while dashed line represents the accidentally coincident γ rays; a peak around the energy of 360 keV was clearly observed as expected. Comparison of the cross sections between elastic and inelastic scatterings yielded the **B** ($E2;2^+ \rightarrow 0^+$) = 0.97 (22) e^2b^2, which was in good agreement with the adopted value of 1.163(16) e^2b^2. The measurement of B (E2) value of the 2^+_1 state of ^{142}Ba will be carried out soon.

The lower charge breeding efficiencies for metallic radioactive ions than the gaseous element is one of the open questions when the ions are charge-bred by ECRIS. The charge breeding efficiencies can be regarded as the product of two efficiencies; the capture efficiency by the ECR plasma and the ionization efficiency for step-by-step charge breeding. In general, for the ECRIS the latter efficiency is supposed to be independent of the element. And thus, the difference of charge breeding efficiencies may attribute to the inadequate capture by the ECR plasma. In order to study the capture process, we injected a metallic element ^{111}In into the ECR plasma in FY2008. The ions were charge-bred and extracted as usual, and then the activities of their residuals in the plasma chamber were measured. The anisotropic distribution was observed around z = 200 mm, the minimum of ECR confinement magnetic field as presented in Fig 2 (a). The anisotropy might be related to the decelerating electric field around the ECR plasma boundaries where the electric potential suddenly changed from 0 kV to around 15 kV; its actual configuration strongly depends on the plasma conditions, and therefore it is hardly simulated. To determine the configuration of the electric field definitely, we installed a grid of molybdenum mesh on the decelerating electrode at the entrance of the plasma chamber. The residual activities observed are illustrated in Fig. 2 (b). It appeared that the anisotropy was well improved. However, the charge breeding efficiencies was almost the same as that obtained without mesh. Further analysis is in progress to understand our observations.

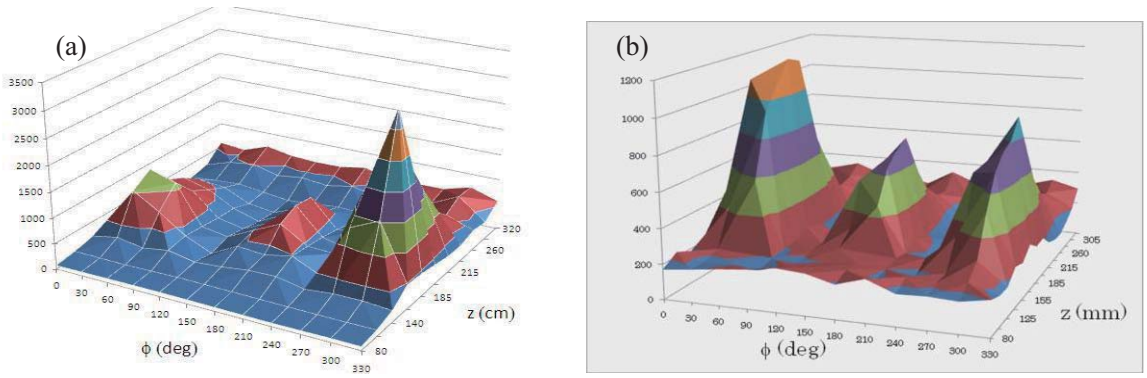

Fig. 2 (a) Residual activities of ^{111}In in the plasma chamber as a function of azimuthal angle (ϕ) and longitudinal position (z). (b) Residual activities of ^{111}In after molybdenum mesh was installed.

1.3 Design of the new beam lines

T. Asozu[1], H. Kabumoto[1] and N. Ishizaki[1]

The project of the radioactive nuclear beam (RNB) accelerator at JAEA-Tokai was over in 2010. We are planning to install new beam lines of the tandem accelerator at the laboratory where the RNB accelerator was placed. We can use radioactive materials as targets in this laboratory, because this room was designed as a high-security controlled area for the RNB project. Figure 1 shows a grand plan of the new laboratory. There are three beam courses; 0° course, 20° course and 45° course. We can switch the beam course with the bending magnet.

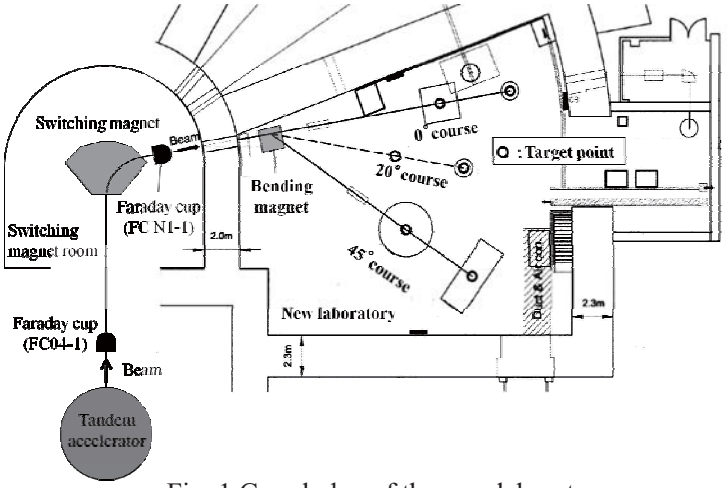

Fig. 1 Grand plan of the new laboratory.

We simulated beam optics with OPTIC Ⅱ and designed the layout of optical devices. OPTIC Ⅱ can simulate the beam emittance ellipse by using a beam transport matrix [1]. The initial conditions in this simulation are as follows. The beams start from the faraday cup (FC 04-1 in Fig. 1). The emittance ellipse is that the radius is 1mm and the divergence angle is 1mrad. The ion species and the energy in each course are $^{136}Xe^{+20}$ and 200 MeV in 0° course, $^{58}Ni^{+13}$ and 230 MeV in 20° course, $^{18}O^{+8}$ and 162 MeV in 45° course. We laid out the optical devices in consideration of the focal distance which maximize the space and minimize the beam radius at the target points. The results are shown in Fig. 2, Fig. 3 and Fig. 4. The box and the circle shapes at the top of the figure show the devices and the target points. Figures under the shapes are the distances. The curved lines show beam envelopes. The dark line shows a horizontal envelope and the light one shows a vertical envelope. Each course has two target points. Upper beam envelopes in each figure are for the target of short distance and the others are for the target of long distance.

There are enough spaces around the target points for installing not only optical devices and vacuum devices but large apparatus such as a γ-ray spectrometer. The beam radii are 0.5~1.0mm at the target points. It is sufficiently small to realize that we use a several micrograms radioisotope for target. The research on surrogate reactions and material properties of reactor fuel will be carried out there.

[1] Japan Atomic Energy Agency (JAEA)

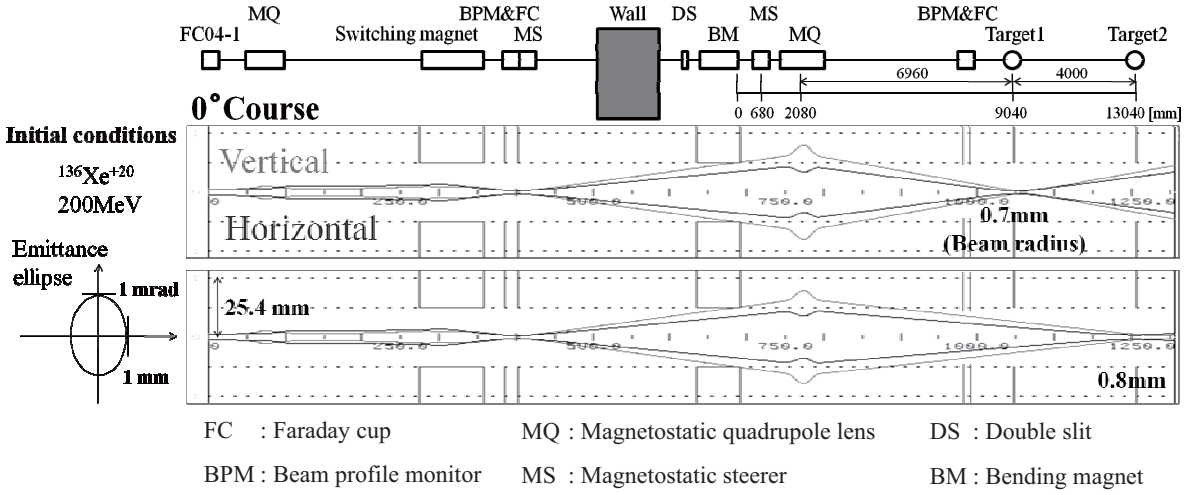

Fig. 2 The devices layout and beam envelopes at 0° course.

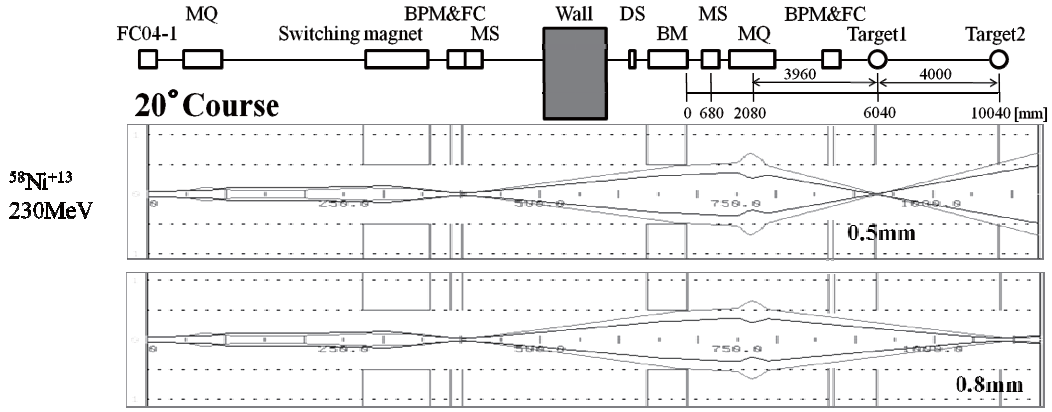

Fig. 3 The devices layout and beam envelopes at 20° course.

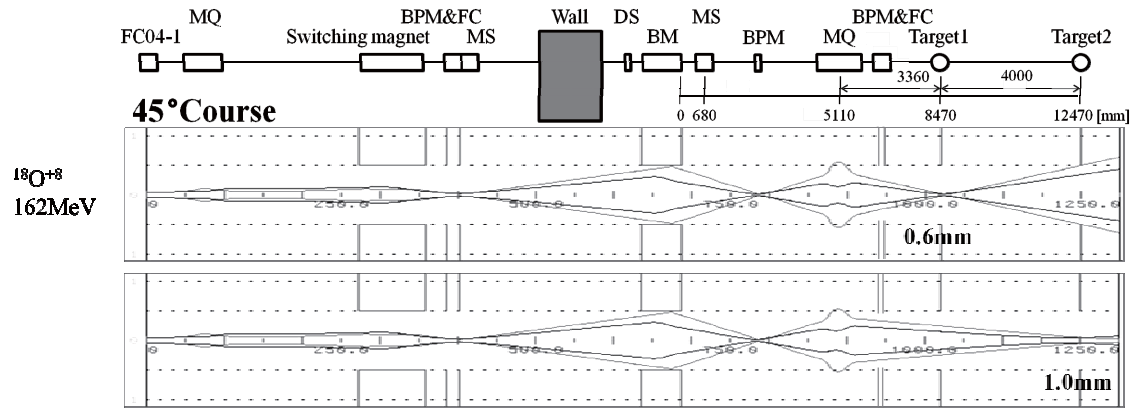

Fig. 4 The devices layout and beam envelopes at 45° course.

Reference

[1] J. D. Larson, Nuclear Instru. Methods, 189 (1981) 71-91.

1.4 Preliminary experiment of the hydrogen analysis by the NRA method using ^{15}N beam from TIS

M. Matsuda[1], T. Asozu[1], M. Nakamura[1] and M. Sataka[1]

For the analysis of hydrogen in solids, the ^{15}N nuclear reaction technique, which utilizes the 6.385 MeV resonance of the reaction $H(^{15}N,\alpha\gamma)^{12}C$, has become a well-established tool. ^{15}N beam in the energy range of 6.3-13.3 MeV is used for measurement of depth distribution of hydrogen in a target sample. These low energy beams can be obtained easily from TIS by extracting single charged ions.

First, we measured depth distribution of hydrogen in a $WO_3(H)$ target sample experimentally. The hydrogen concentration in the sample was $0.7\times10^{17}/cm^2$. For measuring the 4.4 MeV gamma-rays from the $H(^{15}N,\alpha\gamma)^{12}C$ reaction, a 3"×3" NaI detector was used. The detector and the target sample were installed in L2 beam line tentatively. $^{15}N^+$ beam could not be deflected to the L2 beam line because there was a limit of the magnetic field of the switching magnet. So, the charge state was changed to 5+ by a post stripper foil. Fig. 1 shows the profile of H in WO_3 sample prepared by thermal oxidation. The horizontal axis is the beam energy calculated from the magnetic field of the energy analyzing magnet. The rising point of the graph, 6.485 MeV, differs from the resonance energy, 6.385 MeV. It caused that the energy calibration was insufficient and an energy loss was occurred by the post stripper foil. Fig. 1 shows that the thickness of an oxide layer of $WO_3(H)$ was about 0.7 μm. This result was in qualitative agreement with other measurements. To quantify hydrogen concentration, we should measure beam current correctly.
Next, the beam energy calibration of the tandem accelerator was experimentally performed. $^{15}N^+$ beam from the tandem accelerator was directly guided to the H1 beam line. We used a $WO_3(H)$ and a quartz which did not contain hydrogen for target samples. The opening width of the double slit at the object point and the image point of the energy analyzing magnet were 6(x) x 6(y) mm and 1(x) x 2(y) mm, respectively. Fig. 2 shows H profiles of these samples near the surface. Starting point of the reaction was determined to be 6.32 MeV from the magnetic field. Therefore, it was found that the difference of the present beam energy calibration was about 60keV (1%) below the resonance energy.

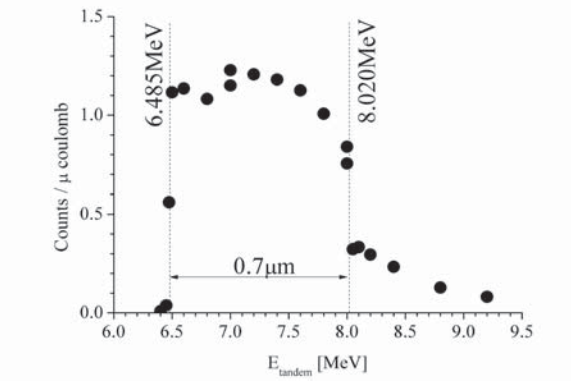

Fig. 1 Hydrogen profile of $WO_3(H)$ sample.

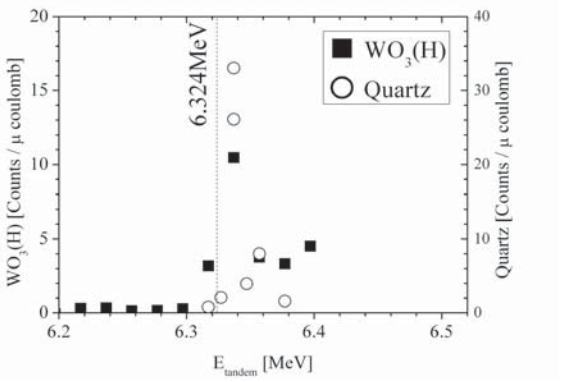

Fig. 2 Hydrogen profiles of $WO_3(H)$ and quartz samples near the surface.

[1] Japan Atomic Energy Agency (JAEA)

This is a blank page.

CHAPTER 2

Nuclear Structure

2.1 In-beam γ-ray spectroscopy of neutron-deficient actinide nuclei using heavy-ion induced transfer reactions
2.2 Development of a gas cell for on-line laser spectroscopy of refractory elements
2.3 Development of high-resolution α fine-structure spectroscopy for the heaviest nuclei
2.4 Coulomb excitation experiment of ^{126}Xe
2.5 Experiment for synthesis of a new isotope ^{216}U
2.6 Development of an electrodeposited target for a surrogate reaction
2.7 Development of spin-polarized radioactive nuclear beam for nuclear spectroscopy through β-delayed decay of spin-polarized nuclei around doubly magic nucleus ^{132}Sn

This is a blank page.

2.1 In-beam γ-ray spectroscopy of neutron-deficient actinide nuclei using heavy-ion induced transfer reactions

M. Asai[1], T. Ishii[1], R. Takahashi[1,2], H. Makii[1], K. Tsukada[1] and N. Sato[1]

In-beam γ-ray spectroscopy using heavy-ion induced transfer reactions is very powerful to study high-spin states in neutron-rich actinide nuclei. In fact, we successfully performed in-beam γ-ray spectroscopy of neutron-rich Th, U, Pu, Cm and Cf isotopes using ^{238}U, ^{244}Pu, ^{248}Cm and ^{249,250,251}Cf targets [1-6] and with transfer reactions of (^{18}O,^{16}O), (^{18}O,^{20}Ne), (^{18}O,^{17}O), (^{16}O,^{15}O) etc. On the other hand, experimental data of high-spin states in neutron-deficient actinide nuclei are still lacking. To study excited states in neutron-deficient actinide nuclei, we have started a series of in-beam γ-ray spectroscopy using proton pickup reactions with an ^{233}U target.

An ^{233}U target with a thickness of 1.8 mg/cm^2 was prepared by an electrodeposition onto a 0.8 mg/cm^2 thick Al backing. The target was bombarded with a 156 MeV ^{18}O^{8+} beam or a 155 MeV ^{16}O^{8+} beam from the tandem accelerator. Projectile-like scattered particles were detected by four Si Δ*E*-*E* telescopes placed at 60 mm away from the target, and at 40° with respect to the beam axis. Six Ge detectors were set around the target chamber to detect in-beam γ rays in coincidence with the scattered particles. Detailed descriptions of the experimental setup are given in Ref. [2].

By setting a gate on the measured *E*-Δ*E* distribution of scattered particles, events of the proton transfer reactions of (^{18}O,^{17}N) or (^{16}O,^{15}N) are selected. With the compiled events, in-beam γ rays from Np isotopes as well as intense Np K X rays were successfully observed. The yields of neutron-deficient Np isotopes in the reaction with the ^{18}O projectile were compared with those with the ^{16}O projectile to examine the optimum experimental conditions. Data analysis is now in progress.

References

[1] T. Ishii et al., Phys. Rev., C72(2005)021301(R).
[2] T. Ishii et al., J. Phys. Soc. Jpn., 75(2006)043201.
[3] T. Ishii et al., Phys. Rev., C76(2007)011303(R).
[4] H. Makii et al., Phys. Rev., C76(2007)061301(R).
[5] T. Ishii et al., Phys. Rev., C78(2008)054309.
[6] R. Takahashi et al., Phys. Rev., C81(2010)057303.

[1] Japan Atomic Energy Agency
[2] Tokyo University of Science

2.2 Development of a gas cell for on-line laser spectroscopy of refractory elements

H. Iimura[1], M. Koizumi[1], M. Miyabe[1] and M. Oba[1]

Laser spectroscopy of the hyper-fine structures (HFS) and isotope shifts (IS) in atomic spectra has been providing much information on the studies of nuclear structure because nuclear moments and nuclear charge radii can be determined from the HFS and IS, respectively. Neutron-deficient nuclei in the rhenium region (Z~75) have been attracting much interest because axially asymmetric shapes are predicted theoretically for them [1]. However, the laser spectroscopy for these isotopes is very scarce because elements in this region are so refractory that they are difficult to be atomized. In order to perform the laser spectroscopy for these isotopes, we are developing an on-line gas cell technique. Following is our recent progress.

The schematic geometry of the gas cell is shown in Fig. 1, which is similar to the one constructed at the Stony Brook tandem accelerator facility [2]. The nickel foil window isolates the gas cell from the accelerator beam line. The gas cell is filled with gas of proper pressure so that the reaction products recoiling out of the target stop at the center of the inner cell. Then, a laser beam illuminates them before

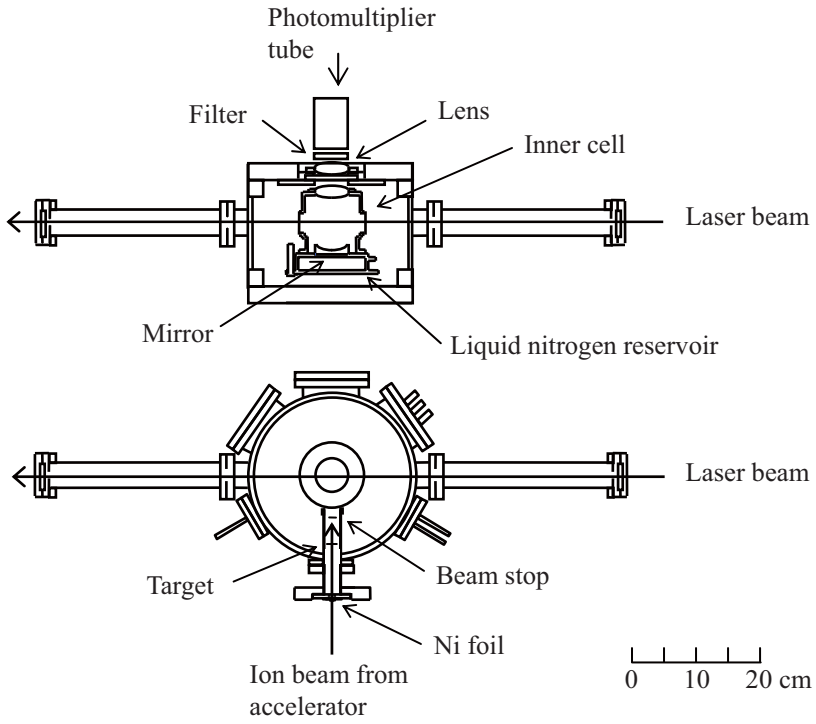

Fig. 1 Schematic layout of the gas cell. The upper and lower sections of the figure are side and top views of the cell, respectively.

[1] Japan Atomic Energy Agency (JAEA)

they diffuse through the gas to the wall of the cell. Laser-induced fluorescence is collected on a photomultiplier tube by a mirror and lenses. Color glass filters suppress stray light from the laser. To reduce the background light coming from the collisions between the gas and ion beam, a beam stop is placed between the target and the inner cell.

Prior to the studies of radioactive isotopes, we are working with stable isotopes to improve the resolution and sensitivity of the apparatus. In order to simulate the tungsten isotopes (Z=74) produced by heavy-ion fusion reactions, a beam of stable ^{184}W was accelerated to 100 MeV by using the tandem accelerator and injected into the gas cell without setting the target and the beam stop. This energy was selected so that the energy of the tungsten beam, after passing through the 5 μm Ni foil window, became the same as that of the reaction-produced isotopes. The intensity of the tungsten beam was about 1 pnA. The gas cell was filled with 19 hPa of argon.

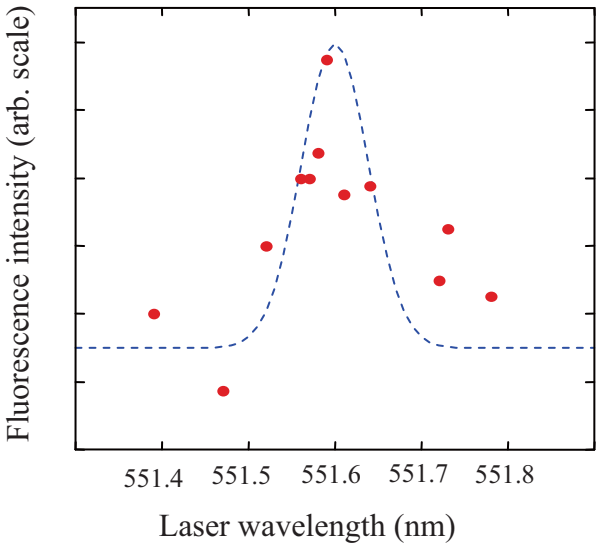

Fig. 2 Spectrum of the 551.6-nm transition of ^{184}W.

The investigated optical transition in tungsten atom is the 551.6-nm transition from $5d^4 6s^2\ ^5D_2$ level at 3326 cm^{-1} – $5d^4 6s6p\ ^7D_1$ level at 21454 cm^{-1}. The wavelength of a tunable dye laser, the bandwidth of which was about 2 GHz, was changed stepwise, and the signal from the photomultiplier tube was counted at each wavelength. The result is shown in Fig. 2. Although the fluorescence intensity fluctuates, the resonance peak at 551.6-nm is observed. Now we are working to obtain a better spectrum by scanning continuously the wavelength of the tunable dye laser with narrower bandwidth of about 1 MHz. Also we plan to reduce the background by chopping the ion beam and the laser beam and counting the signal while these beams are off. After these improvements, we will try on-line laser spectroscopy of unstable tungsten isotopes.

References

[1] P. Möller et al., At. Data Nucl. Data Tables, 94(2008)758-780.

[2] A. Berger et al., Nucl. Instrum. Methods Phys. Res., A311(1992)224-239.

2.3 Development of high-resolution α fine-structure spectroscopy for the heaviest nuclei

M. Asai[1], Y. Shima[2], N. Sato[1], K. Tsukada[1], A. Toyoshima[1], T.K. Sato[1], T. Ishii[1] and M. Shibata[2]

Locations of proton and neutron single-particle orbitals in the heaviest nuclei provide direct information on the shell structure of superheavy nuclei. To establish the proton and neutron single-particle orbitals, experimental assignments of spin-parities and single-particle configurations of the ground states as well as excited states and experimental determination of excitation energies are indispensable. The α-γ coincidence spectroscopy is one of the most sensitive methods to investigate the level structure of the heaviest nuclei. However, in the α decay of the heaviest nuclei, intensities of γ rays are typically very weak because α decays preferentially populate low-energy states in the daughter nucleus and low-energy γ transitions typically have large internal conversion coefficients, especially in nuclei with the large atomic number. Moreover, if the α decays directly populate the ground state or isomeric states, no γ ray is observed. To overcome these difficulties, we have developed high-resolution α fine-structure spectroscopy which makes it possible to identify single-particle configurations only through the α-singles measurement. In this work, applicability of this method is demonstrated by measuring α fine structure of ^{257}No.

The nucleus ^{257}No was produced in the ^{248}Cm(^{13}C,4n) reaction. The beam energy was 70 MeV on target, and the average beam intensity was 0.8-particle μA. Reaction products recoiling out of the target were thermalized in He gas, transported through a 25-m long capillary with a He/KCl aerosol jet into a rotating-wheel α detection system, and deposited on a thin catcher foil eighty of which were set on the wheel. The wheel was periodically rotated at 30-s intervals to move the deposited sources to six consecutive detector stations each of which was equipped with a Si detector (PIPS). To measure α fine structure precisely, the Si detectors were set at the distance with a solid angle of 15% of 4π sr from the source. This setup reduces a low-energy tail of α peaks and also reduces energy sum between α particles and subsequently emitted conversion electrons, Auger electrons, and low-energy X rays which considerably distorts the measured α-energy spectrum. For comparison, α energy spectra were also measured at the distances with solid angles of 24% and 5% of 4π sr. The α-energy resolution of 12 keV FWHM was achieved at the 15% distance.

Figure 1 shows an α-energy spectrum of ^{257}No measured at the 5% distance. It was previously reported that there are two α transitions with energies of 8222 and 8323 keV in the α decay of ^{257}No [1]. The present α-energy spectrum clearly shows each of the 8222 and 8323 keV α groups contains one intense α transition plus two weak α ones which could not be distinguished in the previous experiment [1] owing to the insufficient α-energy resolution. These α lines are considered to be the transitions to rotational band members built on each one-quasiparticle state. Figure 2 shows an α decay scheme of ^{257}No constructed

[1] Japan Atomic Energy Agency
[2] Nagoya University

from the present α fine-structure measurement. The 205 keV level in ^{253}Fm was observed for the first time in the present work. The 0, 22, and 47 keV levels are assigned to be the $1/2^+$, $3/2^+$, and $5/2^+$ states in the $1/2^+$[620] band, respectively; their energy spacings are characteristic of the $1/2^+$[620] rotational band. The 124, 159, and 205 keV levels are assigned to be the $3/2^+$, $5/2^+$, and $7/2^+$ states in the $3/2^+$[622] band, respectively. Their energy spacings are very close to those of the $3/2^+$[622] rotational band in the neighboring nuclei ^{249}Cm and ^{251}Cf [2]. The α-transition intensities to each rotational band and rotational-band member also show large dependences on the spin-parity and single-particle configuration. Although the rotational bands in ^{253}Fm have been already established in our previous α-γ (*e*) coincidence measurement [1], the present result demonstrates that we could assign spin-parities and single-particle configurations in ^{253}Fm only through the α fine-structure measurement.

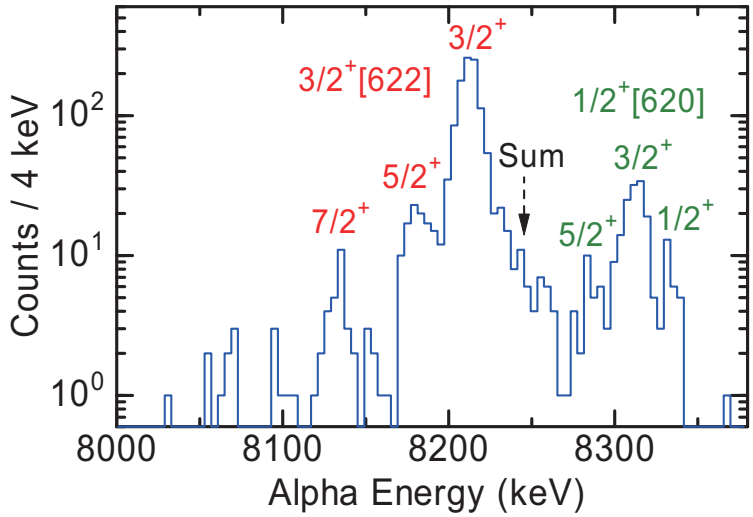

Fig. 1 Measured α fine-structure spectrum of ^{257}No.

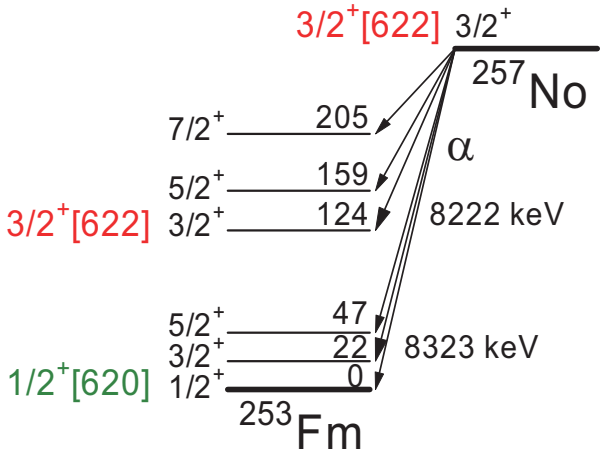

Fig. 2 Alpha decay scheme of ^{257}No constructed from the present α fine-structure measurement.

References

[1] M. Asai et al., Phys. Rev. Lett., 95 (2005) 102502.

[2] *Table of Isotopes, 8th ed.* (John Wiley & Sons, Inc., New York, 1996).

2.4 Coulomb excitation experiment of ^{126}Xe

M. Koizumi[11], Y. Toh[1], A. Kimura[1], Y. Hatsukawa[1], K. Furutaka[1], H. Harada[1], F. Kitatani[1], S. Nakamura[1], M. Sugawara[2] and E. Ideguchi[3]

Being located in a transitional region, stable Xe isotopes gradually change their properties from a γ-unstable character (A ~ 124) to a vibrational (A = 134) [1]. In terms of dynamic symmetry of the IBM, the change is considered as a shape phase transition from O(6) to U(5) symmetry. Theoretical calculations suggested that the E(5) critical point of the shape phase transition would appear at around A = 130 in Xe isotopes [2,3]. To understand the characters of those nuclei, information on electromagnetic properties is required. The B(E2) values near the ground state of $^{126\text{-}136}$Xe are, however, scarcely measured. As for the ^{126}Xe, which is considered to be a γ-unstable nuclei, no B(E2) has been measured except for B(E2: $2_1^+ \rightarrow 0_1^+$).

Coulomb excitation is a useful method for measurements of B(E2)s and quadrupole moments near the ground states of nuclei [4,5]. Our systematic study revealed nuclear properties and their evolutions of stable nuclei with A ~ 70 [6-13]. To obtain electromagnetic properties of $^{126\text{-}136}$Xe isotopes, we have started Coulomb excitation experiments.

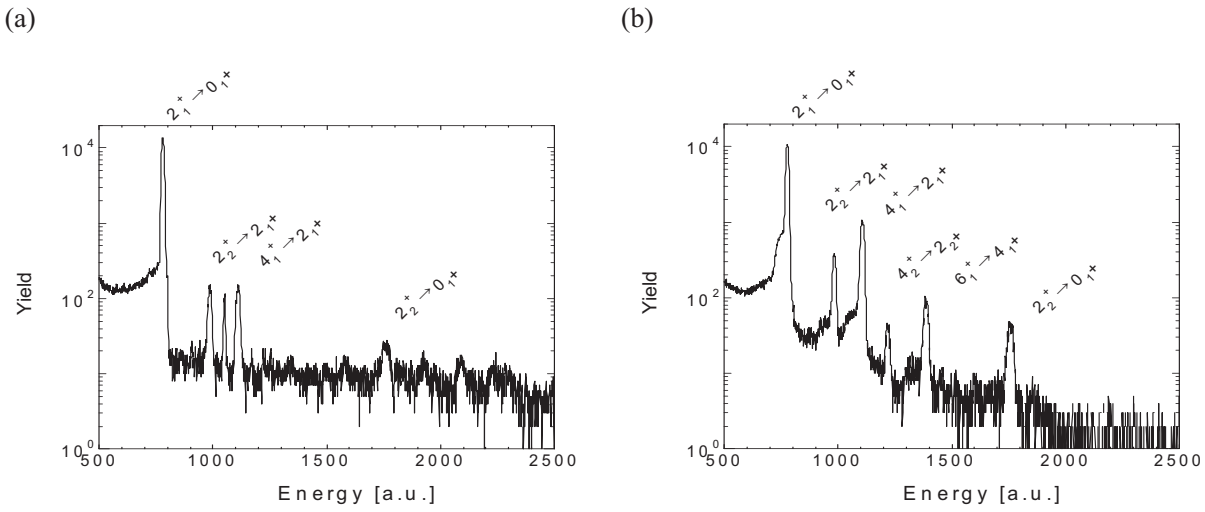

Fig. 1 Doppler-corrected particle-γ coincidence spectra measured with a Ge detector. (a) A Doppler-corrected spectrum obtained in the ^{12}C(^{126}Xe, γ) experiment; the peak between the $2_2^+ \rightarrow 2_1^+$ and $4_1^+ \rightarrow 2_1^+$ transition is a background peak, the origin of which is the radioactive nucleus produced during the adjustment of ion beam. (b) A Doppler-corrected spectrum obtained in the ^{208}Pb(^{126}Xe, γ) experiment.

[1] Japan Atomic Energy Agency (JAEA)
[2] Chiba Institute of Technology
[3] CNS, the University of Tokyo

Coulomb excitation experiments of ^{12}C(^{126}Xe, γ) and ^{208}Pb(^{126}Xe, γ) were carried out with 385-MeV and 560-MeV ^{126}Xe beams; both beam energies are below each of the Coulomb barrier. The beam currents were approximately 0.5 pnA in both cases. The target thicknesses of carbon and ^{208}Pb foils were 500 μm and 0.9 μm (1 mg/cm^2), respectively. A γ-ray detector array, GEMINI-II [14,15], was used to detect de-excitation γ rays, and a position sensitive particle detector array, LUNA [16], was used to detect recoiled or scattered particles. Totally, approximately 8×10^6 and 3×10^7 particle-γ coincidence events were obtained in the ^{12}C(^{126}Xe, γ) experiment and in the ^{208}Pb(^{126}Xe, γ) experiment, respectively.

Position data of LUNA were used for corrections of Doppler shift of γ-energies. Deduced angles of recoiled carbon and scattered ^{126}Xe were used for the correction in the ^{12}C(^{126}Xe, γ) and the ^{208}Pb(^{126}Xe, γ) reaction, respectively. Figure 1 shows Doppler-corrected γ spectra. During the adjustment of the ion beam in the ^{12}C(^{126}Xe, γ) experiment, it happened that ^{14}N^{2+} hit the carbon target (the A/Q of it is the same as that of ^{126}Xe^{18+}); this resulted in producing radioactive isotopes. The experiment was, therefore, carried out with ^{126}Xe^{24+} ion beam. A sharp peak of Fig. 1(a) between the $2_2^+\rightarrow 2_1^+$ and $4_1^+\rightarrow 2_1^+$ transition is 511-keV γ ray relevant to the decay of the unstable nuclei. Four de-excitation peaks are identified in the ^{12}C(^{126}Xe, γ) spectrum, and six peaks in the ^{208}Pb(^{126}Xe, γ) spectrum. ^{126}Xe was excited up to the 6_1^+ and 4_2^+ states with ^{208}Pb(^{126}Xe, γ) reaction; the excitation energy of the 6_1^+ and 4_2^+ states are 1634 keV and 1488 keV, respectively. The analysis of the experimental data is in progress. B(E2) values and quadrupole moments will be deduced with the χ^2 minimum search code GOSIA.

References

[1] R.F. Casten and P.V. Brentano, Phys. Lett., 152(1985)22.
[2] D.L. Zhang and Y.X. Liu, Chin. Phys. Lett., 20(2003)1028-1030.
[3] R. Fossin, Dennis Bonatsos, and G.A. Lalazissis, Phys. Rev., C73 (2006)044310.
[4] K. Alder and A. Winther, Coulomb Excitation (Academic, New York, 1966).
[5] K. Alder and A. Winther, Electromagnetic Excitation (North Holland, Amsterdam, 1975).
[6] Y. Toh et al., J. Phys., G27(2001)1475-1480.
[7] Y. Toh et al., Eur. Phys. J., A9(2000)353-356.
[8] A. Osa et al., Phys. Lett., B546(2002)48-54.
[9] M. Zielinska et al., Nucl. Phys., A712(2002)3-13.
[10] M. Koizumi et al., Eur. Phys. J., A18(2003)87-92.
[11] M. Sugawara et al., Eur. Phys. J., A16(2003)409-414.
[12] M. Koizumi et al., Nucl. Phys., A736(2003)46-58.
[13] T. Hayakawa et al., Phys. Rev., C67(2003)064310.
[14] K. Furuno et al., Nucl. Instrum. Methods Phys. Res., A421(1999)211; M. Oshima et al., J. Radioanal. Nucl. Chem., 278 (2008)257-262.
[15] M.Oshima et al., J. Radioanal. Nucl. Chem., 278 (2008)257-262.
[16] Y. Toh et al., Rev. Sci. Inst., 73 (2002)47-50.

2.5 Experiment for synthesis of a new isotope ^{216}U

Y. Wakabayashi[1], K. Nishio[1], S. Mitsuoka[1], I. Nishinaka[1], H. Makii[1], R. Takahashi[1], S. Yan[1] and H. Miyatake[2]

Synthesis of neutron-deficient actinide nucleus close to the N=126 shell closure is important to understand the stability of the N=126 closed shell [1] and also to study the nuclear structure for the actinide nucleus with spherical shape. We have started a campaign to investigate the nuclei in this region. In this report, we have carried out the experiment to produce a new isotope ^{216}U in the fusion reaction of ^{82}Kr+^{138}Ba and to measure its alpha-decay energy and half-life.

The experiment to produce ^{216}U was performed using the ^{138}Ba (^{82}Kr, 4*n*) ^{216}U reaction. The cross section of ^{216}U is estimated to be about 100 *pb* using the HIVAP code [2]. The $^{82}Kr^{12+}$ beam of 395 MeV was supplied from the JAEA-tandem accelerator and bombarded the rotating ^{138}Ba target foil. The ^{138}Ba targets of 233 and 332 μg/cm^2 in thickness were made by sputtering a 99%-enriched material of ^{138}Ba isotope on 0.8 mm aluminum foil. A total beam dose of 6.7x10^{16} was accumulated. Evaporation residues (ER's) emitted to the beam direction were separated from the ^{82}Kr beam by a recoil mass separator (JAEA-RMS). The separated recoils were implanted into a double-sided position-sensitive strip detector (PSD; 73x55 mm^2). The energy calibration of the PSD was performed using known α lines from ^{204}Rn(6.42 MeV), ^{209}Fr(6.65 MeV), and ^{207}Ra(7.13 MeV) produced in the ^{82}Kr+^{130}Te reaction. Two Multi Channel Plates (MCP's) were used for timing detectors to obtain the time-of-flight (TOF) signal of the ER's. The presence of the signal in the timing detectors was also used to separate the α decay in the PSD from the recoil implantation.

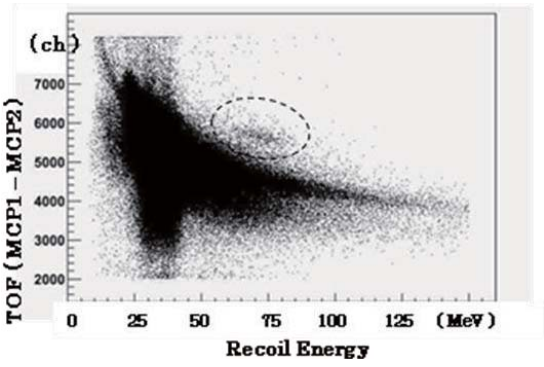

Fig. 1 Two dimensional spectrum of the energy versus TOF obtained from the ^{82}Kr+^{138}Ba reaction. The unit of X and Y axis are MeV and ch, respectively. The dashed line shows the area of ER's.

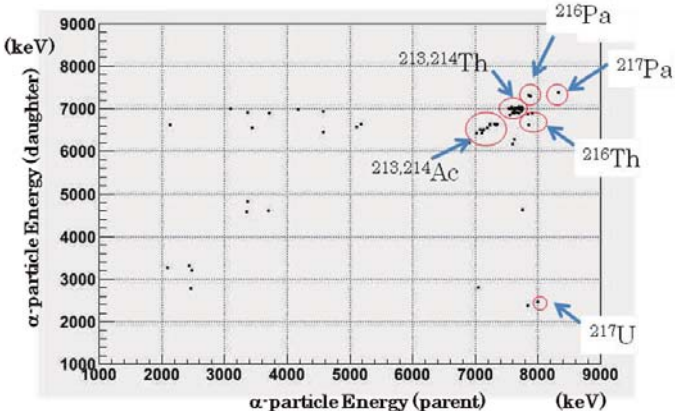

Fig. 2 Two dimensional spectrum of α-α correlation originated from ER's. The X and Y axis are α-particle energy emitted from parent nucleus and daughter one, respectively. The circle with arrow and name shows a α chain starting from parent nucleus.

[1] Japan Atomic Energy Agency (JAEA)
[2] High Energy Accelerator Research Organization (KEK)

Figure 1 shows a two dimensional spectrum of the recoil energy versus TOF obtained from the $^{82}Kr+^{138}Ba$ reaction. In Fig. 1, the region of dashed line also shows the area of ER's produced by the $^{82}Kr+^{138}Ba$ reaction. From the result of analysis using this area, α-α correlation spectrum was obtained as shown in Fig. 2. It was found that α-α chains from ER's shown in Fig. 3 were observed as indicated. One event for known ^{217}U [3] was observed, which we expect to have the same cross section as ^{216}U in this incident energy. As shown in Fig. 4 (a), the cross section of this nucleus was estimated to be about 100 *pb* as same as ^{216}U. Here, in this experiment, we obtained an upper-limit cross-section of 65 *pb* for ^{216}U and confirmed the consistent cross-section for other observed ER's. This indicates that the estimation using the HIVAP code is reliable for the $^{82}Kr+^{138}Ba$ reaction system. We will continue the experiment to produce ^{216}U down to the cross section limit of 10 *pb*.

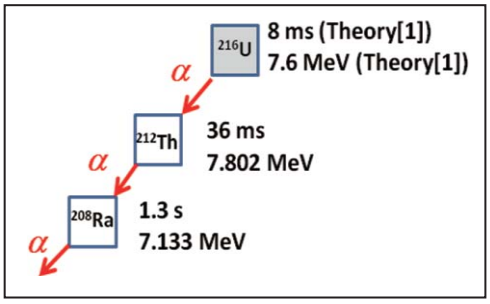

Fig. 3 Schematic view of α-decay chain starting from ER's. In this figure, ^{216}U is described as a relevant. ^{212}Th and ^{208}Ra are known nuclei. The half-lives and α-particle energies are shown. For ^{216}U, these are calculated ones by Koura et al [1].

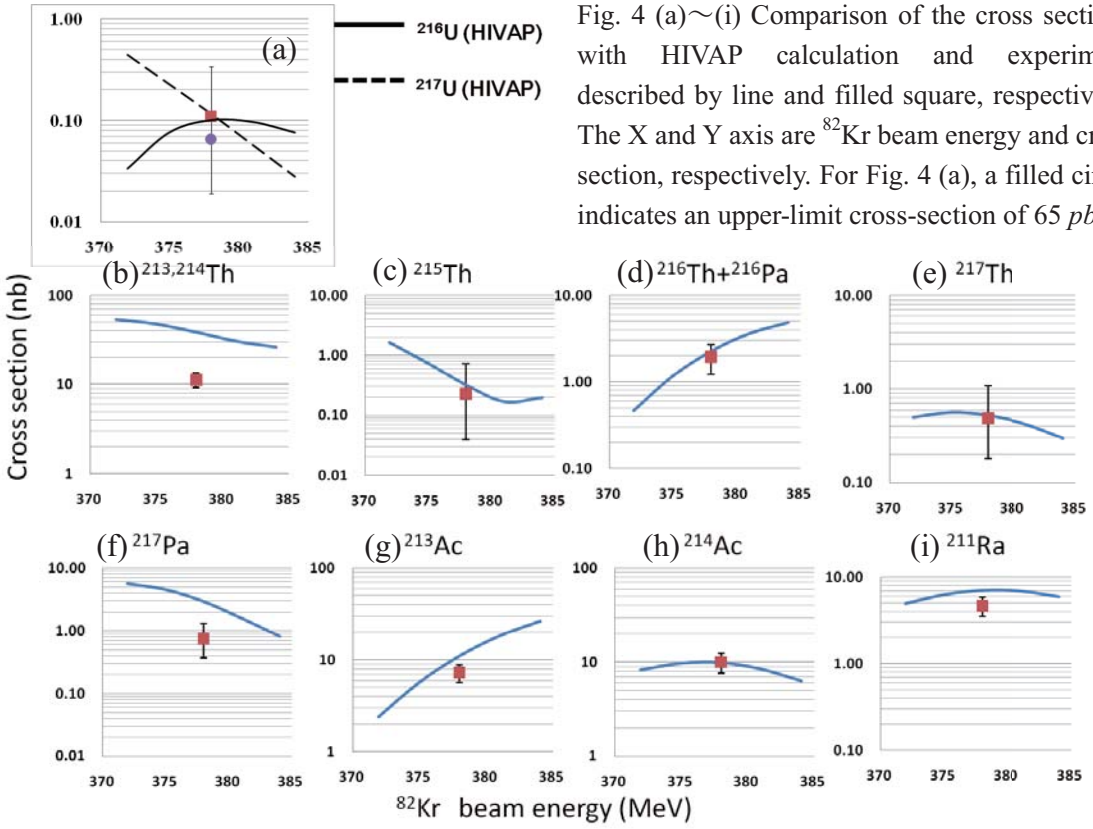

Fig. 4 (a)～(i) Comparison of the cross sections with HIVAP calculation and experiment described by line and filled square, respectively. The X and Y axis are ^{82}Kr beam energy and cross section, respectively. For Fig. 4 (a), a filled circle indicates an upper-limit cross-section of 65 *pb*.

References

[1] H. Koura and T. Tachibana, Btsuri (in Japanese), 60 (2005)717-724.

[2] W. Reisdorf and M. Schadel, Z. Phys., A343(1992)47-57.

[3] O.N. Malyshev et al., Eur. Phys. J., A8(2000)295-297.

2.6 Development of an electrodeposited target for a surrogate reaction

T. Ishii[1], H. Makii[1], I. Nishinaka[1], M. Asai[1], K. Tsukada[1] and R. Takahashi[1,2]

We develop a surrogate reaction method for deducing neutron cross sections of an actinide nucleus whose lifetime is too short to be used as a target. In this method, neutron incident energy is derived from the kinetic energy of a scattered nucleus. For example, using the $^{238}U(^{18}O,^{16}O)^{240}U$ transfer reaction, neutron incident energy for the $n+^{239}U$ reaction can be obtained from the kinetic energy of ^{16}O. Therefore, it is important to measure kinetic energies of scattered particles with good energy resolution. Actinide targets, e.g., Pu and Cm, used in the surrogate reaction are usually produced by an electrodeposited method because of their scarcity and radioactivity. In our earlier experiment using an electrodeposited ^{248}Cm target, we have experienced a bad energy resolution of scattered particles, which should be caused by a large variation of thickness of this target. Therefore, we have examined the uniformity of the thickness of an electrodeposited target, using gadolinium instead of radioactive actinide.

An electrodeposited target was prepared as follows. 5μl nitric gadolinium ($Gd(NO_3)_36H_2O$) aqueous solution of 8.9 mol/l was dissolved in isopropyl alcohol of 2 ml. High voltage of 1000 V was applied to a platinum electrode in the solution, and nitric gadolinium was electrodeposited on an aluminum foil during 15 min. Electrodeposited area was 5 mm in diameter. The thickness of nitric gadolinium was 0.71 mg/cm^2 and that of the aluminum foil was 0.5mg/cm^2. For comparison, we also made an evaporated metal Gd target of 0.37 mg/cm^2 in thickness on a 0.4 mg/cm^2 thick aluminum foil.

We have tested the uniformity of thickness for the targets by measuring kinetic energies of elastically scattering particles using a 135 MeV ^{18}O beam at the JAEA tandem accelerator. Beam was collimated using an aperture of 1.4 mm in diameter. Elastically scattered particles were measured at 28±0.6 degree with respect to the beam axis using a Si detector. Figures 1(a) and 1(b) show energy spectra of scattered particles of ^{18}O for the evaporated target and the electrodeposited target, respectively. The peak width (FWHM) for the former and the latter target was 500 keV and 650 keV, respectively. The spectrum for the electrodeposited target has a large tail. By observing this target using a microscope, we have found that this target has many spherical-shape particles about 20 μm in diameter. This should cause a large energy loss. By changing the electrodeposited condition, we can reduce these particles. We will find conditions for producing a target with good uniformity of thickness.

[1] Japan Atomic Energy Agency (JAEA)
[2] Tokyo University of Science

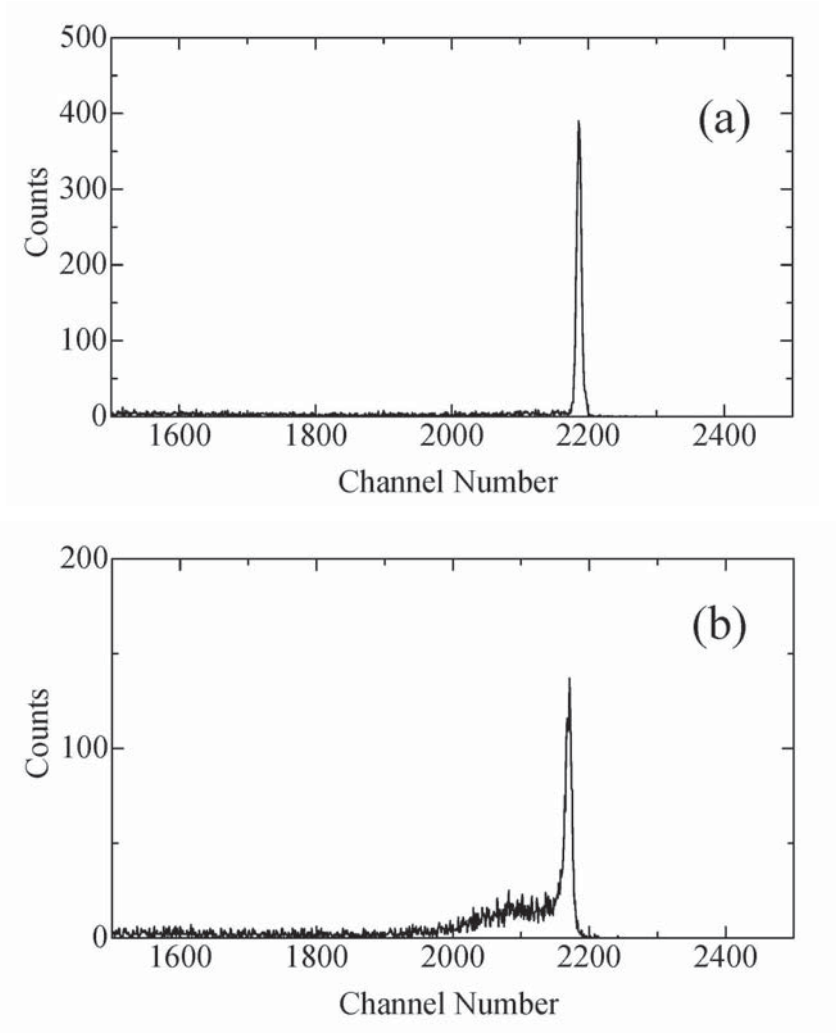

Fig. 1 Energy spectra of elastically scattered ^{18}O particles measured by a Si detector (a) for an evaporated Gd target (metal Gd of 0.37 mg/cm^2 in thickness) and (b) for an electrodeposited Gd target (nitric Gd of 0.71 mg/cm^2 in thickness). Beam energy of ^{18}O was 135 MeV. Peak width (FWHM) of the elastically scattered peak in the spectrum (a) and (b) is 500 keV and 650 keV, respectively.

2.7 Development of spin-polarized radioactive nuclear beam for nuclear spectroscopy through β-delayed decay of spin-polarized nuclei around doubly magic nucleus ^{132}Sn

Y. Hirayama[1], M. Mihara[2], Y.X. Watanabe[1], N. Imai[1], S.C. Jeong[1], K. Matsuta[2], H. Miyatake[1], S. Momota[3], H. Ishiyama[1], T. Izumikawa[4], I. Nishinaka[5], K. Nishio[5], H. Makii[5], S. Mitsuoka[5], Y. Otokawa[5], T.K. Sato[5] and Y. Wakabayashi[5]

Spin-polarized radioactive isotope beam (RIB) is a useful tool to study nuclear structures and material science. For nuclear spectroscopy around the doubly magic nucleus ^{132}Sn at TRIAC facility, we have developed the tilted-foil (TF) technique [1] for the production of spin-polarized radioactive isotope beams. The details of the TF method and the previous results of the development at TRIAC were reported in refs. [2, 3]. Here, we report the successful production of spin-polarized $^{123}In_{g.s.}$ ($T_{1/2}$ = 6.17 s, $I^{\pi} = 9/2^{+}$, g = 1.220) for the first time and the systematic study for enhancement of polarization by means of multi-tilted foil using $^{8}Li_{g.s.}$ ($T_{1/2}$ = 838 ms, $I^{\pi} = 2^{+}$, g = 0.8268).

The experimental conditions for the production of $^{123}In_{g.s.}$ polarization are as follows: The beam energy was 305 keV/nucleon. The carbon foil with thickness of 10 μg/cm^2 was used as a stack of 15 sheets with tilted angle of 70^o. The stopper material for the preservation of nuclear polarization was a cubic semiconductor crystal of InAs (N-type) at a temperature of about 18 K under the magnetic field of B_0 ~ 0.5 T. In the present experiment, the nuclear polarization of $^{123}In_{g.s.}$ was successfully produced by the TF method owing to stable supply for about 24 hours of ^{123}In beam with the intensity of about 1.6×10^3 particles per second (pps). Figure 1 shows the measured nuclear polarization at the tilted angles of ±70^o by β-NMR technique. The degrees of nuclear polarization are –0.67 ± 0.47% and +2.37 ± 0.90% at tilted angles of ±70^o reversing the stacked tilted-foils, respectively. The change of nuclear polarization according to the foil direction clearly demonstrates that the $^{123}In_{g.s.}$ nucleus was polarized by the TF method and the procedure of NMR worked properly. From the double ratio between the nuclear polarization of ±70^o, the degree of nuclear polarization 1.63 ± 0.54% was deduced in the accuracy of 3.0 times of the standard deviation (σ), which indicated that the ground state of ^{123}In was certainly polarized by the TF method.

A study of the TF method has been performed using the ^{8}Li beam with typical beam intensity of 10^5 pps. ^{8}Li nuclei were implanted in an annealed platinum stopper foil of 10 μm thick at room temperature, where the magnetic field of B_0 ~0.05 T was applied to preserve the nuclear polarization. The β-NMR technique was applied to the measurement of the nuclear polarization. Figure 2 shows the obtained polarization as a function of the number of foils. The foils used for this experiment were polystyrene foils with thickness of 3.8 μg/cm^2 and the incident beam energies were 140, 178 and 240 keV/nucleon. The measured nuclear

1 High Energy Accelerator Research Organization (KEK)
2 Osaka University
3 Kochi University of Technology
4 Niigata University, 5 Japan Atomic Energy Agency(JAEA)

polarization P_I successfully built up with increase in the number of foils. And at the lower incident energies, much higher nuclear polarization P_I were produced with the same numbers of the foils. The solid lines in Fig. 2 show the fitted results using the classical-model formula $P_I(N) \sim (I+1)/(J+1)\ (1-Q^N)P_J$, where the multi-foil effect is taken into account [4]. Here N is the number of foils, I and J are nuclear and atomic spins, respectively, P_J is the degree of atomic polarization. For small P_J, Q is expressed approximately by: $1-2J^2/3I^2$ if $I/J>1$, 1/2 if $I/J = 1$, 1/3 if $I/J < 1$. Dominant atomic state for the atomic and nuclear polarization could be estimated by using the formula for the nuclear polarization P_I measured as a function of the number of foils. The data points observed with largest number of foils at the beam energy of 140 and 240 keV/nucleon are largely deviated from the general tendency. Except for the two data points, the data points seem to be well reproduced with the formula. In the fitting, we assumed the atomic spin of $J = 1/2$ for ^{8}Li ions. This value actually governs the dependence of the polarization on the number of foils. If the atomic spin is assumed to be higher than $J = 1/2$, the formula becomes saturated with about 10 foils and cannot reproduce the experimental data. It indicates that 2p ($^2P_{1/2}$) state would dominantly contribute to produce the polarization of ^{8}Li. The most probable values for the P_J were 7.95(22), 5.66(15) and 3.85(19) % for 140, 176 and 240 keV/nucleon, respectively, and decreased with increasing incident energies in the present case.

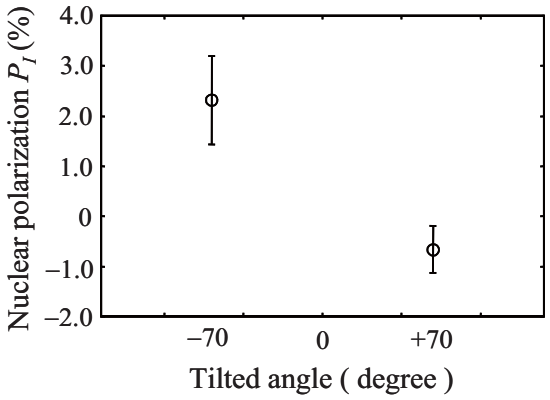

Fig.1 The degrees of nuclear polarization of ^{123}In were measured at tilted angles of ±70° reversing the stacked tilted-foils.

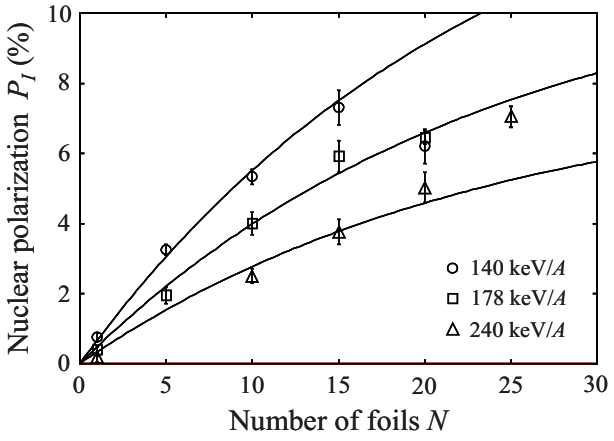

Fig. 2 Nuclear polarization P_I of ^{8}Li beam as functions of the number of polystyrene foils measured for incident beam energies of 140, 178 and 240 keV/nucleon, respectively. The solid lines were given by fitting the formula for nuclear polarization P_I to the data

References

[1] Y. Nojiri and B.I. Deutch, Phys. Rev. Lett., 51 (1983)180.
[2] Y. Hirayama et al., JAEA-Review, 2007-046 (2007)28.
[3] Y. Hirayama et al., JAEA-Review, 2008-054 (2008)48.
[4] M. Lindroos et al., Nucl. Phys., A361(1995)53.

This is a blank page.

CHAPTER 3

Nuclear Reaction

3.1 Influence of the reaction Q-value on heavy-ion induced fission
3.2 Fission fragment anisotropy in heavy-ion-induced fission of actinides
3.3 Measurement of the $^{12}C(\alpha,\gamma)^{16}O$ cross sections by using TRIAC
3.4 Development of Si ΔE-E detector for detection of light ions

This is a blank page.

3.1 Influence of the reaction Q-value on heavy-ion induced fission

K. Nishio[1], S. Mitsuoka[1], I. Nishinaka[1], H. Makii[1], Y. Wakabayashi[1], H. Ikezoe[1],
T. Ohtsuki[2] and K. Hirose[2]

Understanding of heavy-ion fusion is important to make a proper estimation of the production cross section for superheavy nuclei (SHN). In heavy-ion induced reactions, quasifission competes with fusion, so that the fusion cross section is lower than the cross section that the colliding nuclei penetrate or overcome the Coulomb barrier. A possible way to get information on fusion is to measure the fission fragments produced by heavy-ion collision. The fission process has two origins with different properties; the compound-nucleus fission (fusion-fission) and quasifission. The fusion probability can be estimated from the measured fission spectra with the help of a theoretical model such as unified theory [1,2]. In this model, fusion-fission and quasifission evolve on a potential energy surface of a nucleus with different trajectories and form the inherent mass distribution. The incident beam energy has a crucial effect on the evolution of the nuclear shape. After the collision between the projectile and target nucleus, the trajectory calculation is started by referring the excitation energy of a system relative to the ground state, E^* (= $E_{\mathrm{c.m.}}$ + Q) [2], so that the Q-value is a variable in addition to the incident energy $E_{\mathrm{c.m}}$.

We measured the incident-energy dependence of the fission fragment mass distribution in the reactions of ^{40}Ca + ^{238}U and ^{48}Ca+^{238}U in order to see the effects of the reaction Q-value on the fusion process. The Q-values for fusion are -138.6 MeV and -159.1 MeV for the former and the latter reactions, respectively. These reactions will have a difference in the excitation energy of 20.5 MeV at a certain incident energy $E_{\mathrm{c.m.}}$. In the heavy-ion induced fission using actinide target nucleus, it has been known that quasifission has a mass-asymmetric fission yield, whereas fusion-fission has a symmetric yield [3-6].
The purpose of this work is to see if the variable E^* can account for the relative yield for symmetric and asymmetric fission.

The experiment was carried out by using ^{40}Ca and ^{48}Ca beams supplied by the tandem-booster accelerator. The ^{238}U target was made by an electro-deposition method. The fission fragments were detected in coincidence by position-sensitive multi-wire proportional counters (MWPCs). The experimental setup was essentially the same as in [6]. Fission fragment masses are determined by using a conservation law for the mass and momentum. Results for the mass distributions are shown in Fig. 1. The yield is normalized such that the sum of the yield over the mass is 200 %. In both reactions, we observed transition from the symmetric to asymmetric mass distributions to the direction of low incident energy. The variation of the mass distribution represents the effects of deformed target nucleus on the completion between fusion and quasifission. The ^{238}U target nucleus has a prolate deformation. At the high incident energy, where the projectile can collide on the equatorial side of the target nucleus, the fusion probability is larger. The

[1] Japan Atomic Energy Agency (JAEA)
[2] Tohoku University

quasifission increases at the low incident energy, where the projectile can contact only to the polar sides of ^{238}U.

Agreement of the shape of the mass distribution between ^{48}Ca + ^{238}U and ^{40}Ca + ^{238}U is seen when they are compared at the same the incident energy ($E_{c.m.}$) rather than the excitation energy (E^*). In a preliminary calculation, the conditional saddle point which the ^{40}Ca + ^{238}U system must surmount to reach the shape of the compound nucleus is about 26 MeV higher than that for ^{48}Ca + ^{238}U. It means that the former reaction needs 26 MeV higher excitation energy than the latter reaction to give the same fusion probability. Considering the difference in the Q-value (20.5 MeV), this condition is achieved when the incident beam energy has a similar value.

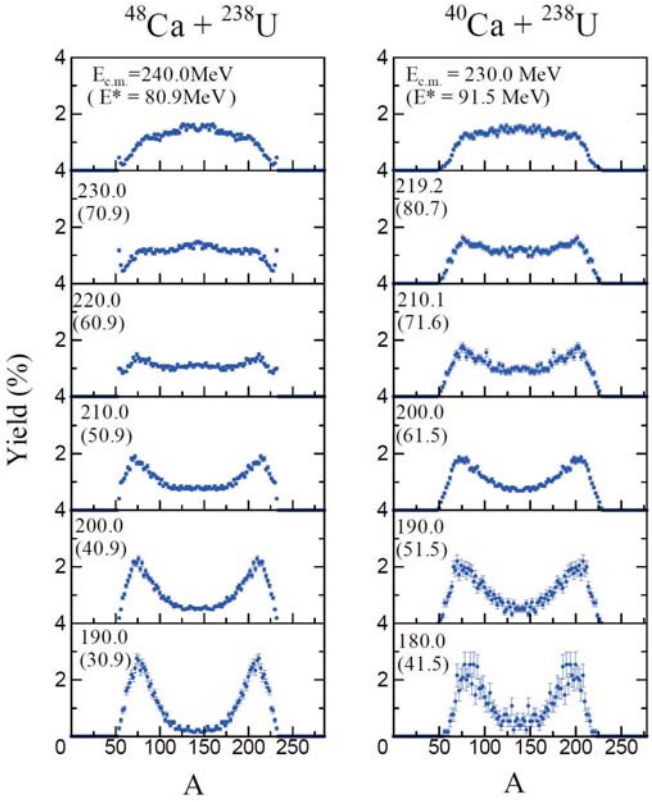

Fig. 1 Fission fragment mass distributions for ^{48}Ca+^{238}U and ^{40}Ca+^{238}U. Reaction energy in the center-of-mass frame ($E_{c.m.}$) and excitation energy (E^*) are shown.

References

[1] V. Zagrebaev and W. Greiner, J. Phys., G31(2005)825.
[2] Y. Aritomo, Phys. Rev., C80(2009)064604.
[3] W.Q. Shen et al., Phys. Rev., C36(1987)115.
[4] J.Töke et al., Nucl. Phys., A440(1985)327.
[5] M.G. Itkis et al., Nucl. Phys., A787(2007)150c.
[6] K. Nishio et al., Phys. Rev., C77(2008)064607.

3.2 Fission fragment anisotropy in heavy-ion-induced fission of actinides

I. Nishinaka[1], K. Nishio[1], M. Tanikawa[2], H. Makii[1], S. Mitsuoka[1],
Y. Wakabayashi[1] and A. Yokoyama[3]

In heavy-ion-induced fission of actinides at near-barrier energies, it has been found that fission fragment anisotropy become anomalously large compared with that expected from the standard saddle point model. The pre-equilibrium *K*-states model suggests that entrance channel mass asymmetry $\alpha=(A_t-A_p)/(A_t+A_p)$ plays an important role for fission fragment anisotropy in heavy-ion-induced fission of actinides [1, 2]. A_t and A_p are mass numbers of target and projectile nuclei, respectively. In the previous work [3], in order to study the effect of entrance channel mass asymmetry α on fission fragment anisotropy, we measured fission fragment angular distributions in the reactions of $^{22}Ne+^{232}Th$ (α =0.827) and $^{12}C+^{242}Pu$ (α =0.906), producing the same compound nucleus ^{254}Fm. The results suggest that entrance channel mass asymmetry play a role for fission fragment anisotropy. In addition, we have measured fission fragment angular distribution for $^{16}O+^{238}U$ (α =0.874) populating ^{254}Fm to obtain additional and detailed information on the effect of entrance channel mass asymmetry.

A ^{238}U target was irradiated with ^{16}O ions of energy E_{lab} = 100.8, 96.9, 93.0, 89.1, and 85.0 MeV at the JAEA tandem accelerator, excitation energies of the compound nucleus being 56.1, 52.5 48.8, 45.2, and 41.3 MeV, respectively. These excitation energies except for 41.3 MeV correspond to the same excitation energies of the compound nucleus ^{254}Fm for $^{22}Ne+^{232}Th$ and $^{12}C+^{242}Pu$ in the previous work [3]. The ^{238}U target with a thickness of 174 μg/cm^2 was prepared by molecular electrodeposition onto 89 μg/cm^2 nickel foil. Fission fragments were measured by three position-sensitive parallel-plate avalanche counters (PPACs) and a silicon surface barrier detector (SSD). Each PPAC has the sensitive area of 20×8 cm^2 for horizontal (X) and vertical (Y) directions in the reaction plane. The PPACs cover horizontal angles of θ= 25º-67º, 73º-105º, and 205º-247º in laboratory system. The SSD located at θ= 176º has a solid angle of 0.8 msr.

Figure 1 shows the center-of-mass angular distribution of fission fragments in the 100.8 MeV $^{16}O+^{238}U$, using the fission fragment kinetic energy estimated by the systematic of Viola et al. [4]. The data points at $86.5º < \theta_{c.m.} < 110.5º$ were determined from coincident fission events measured by the PPAC at θ= 205º -247º and the PPAC at θ= 25º-67º or 73º-105º, and the data point at θ= 176º was obtained from fission events measured by the SSD. The center-of-mass angular distribution provides the fission fragment anisotropy defined as $A = W(180º)/ W(90º)$. Figure 2 shows the present and previous results of the fission fragment anisotropy as a function of the excitation energy of the compound nucleus by solid circles for $^{16}O+^{238}U$, open ones for $^{22}Ne+^{232}Th$, and open squares for $^{12}C+^{242}Pu$. The error bar indicates the uncertainty of experimental angular distribution as shown by dashed lines in fig. 1. The anisotropy for $^{16}O+^{238}U$ is

[1] Japan Atomic Energy Agency (JAEA)
[2] University of Tokyo
[3] Kanazawa University

close to that for $^{12}C+^{242}Pu$ but slightly larger at lower energies. The anisotropy for $^{22}Ne+^{232}Th$ with the smallest entrance channel mass asymmetry $\alpha = 0.827$ clearly is large as compared with those for $^{16}O+^{238}U$ with $\alpha = 0.874$ and $^{12}C+^{242}Pu$ with $\alpha = 0.906$. The Businaro-Gallone critical point [5,6], which corresponds to the conditional saddle point with respect to mass asymmetric deformation on the energy surface of the fission potential in the liquid drop model, was calculated to be $\alpha_{BG} = 0.903$ for ^{254}Fm according to the parameterization of ref. [7]. While, for touching two nuclei, the Businaro-Gallone critical point was estimated to be $\alpha_{BG} = 0.819$ using the liquid drop energy and the electrostatic repulsion energy between the touching nuclei [8]. The entrance channel mass asymmetry $\alpha = 0.827$ for $^{22}Ne+^{232}Th$ is close to $\alpha_{BG} = 0.819$ for a touching two nuclei compared with $\alpha_{BG} = 0.903$ of the fission potential. It indicates that the large anisotropy for $^{22}Ne+^{232}Th$ is strongly related to the potential energy of the touching two nuclei compared with the fission potential.

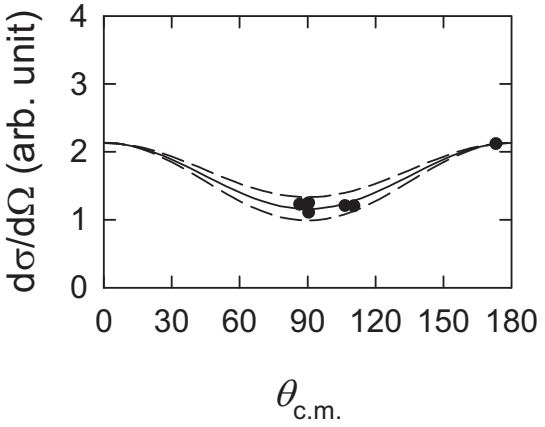

Fig. 1 The center-of-mass angular distributions of fission fragments in the 100.8 MeV $^{16}O+^{238}U$ reaction.

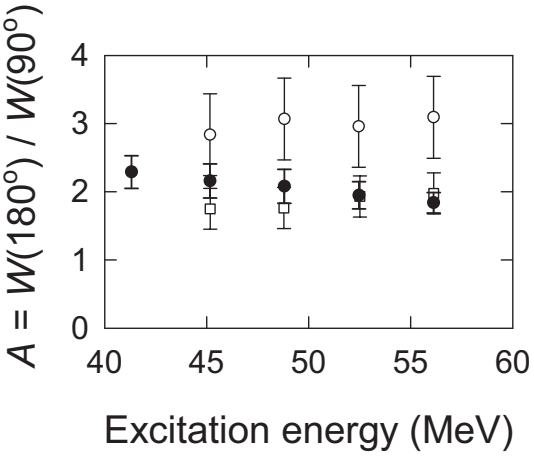

Fig. 2 Preliminary results of the fission fragment anisotropy for $^{16}O+^{238}U$ (solid circles), $^{12}C+^{242}Pu$ (open square) and $^{22}Ne+^{232}Th$ (open circles) as a function of the excitation energy of the compound nucleus ^{254}Fm.

Referenc

[1] V.S. Ramamurthy *et al*., Phys. Rev. Lett., 65(1990)25-28.

[2] Z. Liu et al., Phys. Lett., B353(1995)173-178.

[3] I. Nishinaka et al., JAEA-Review, 2010-056(2010)46-47.

[4] V.E. Viola et al., Nucl. Data Tables, A1(1966)391-410.

[5] U. L. Businaro and S. Gallone, Nuovo Cimento, 5 (1957)315-317.

[6] K.T.R. Davis and A.J. Sierk, Phys. Rev., C31(1985)915-922.

[7] M. Abe, KEK Preprint 86-26, KEK TH-128 (1986).

[8] W. Nörenberg and H.A. Weidenmüller, *Introduction to the Theory of Heavy-Ion Collisions*, (Springer-Verlag, New York, 1980)43-46.

3.3 Measurement of the $^{12}C(\alpha,\gamma)^{16}O$ cross sections by using TRIAC

H. Makii[1], H. Miyatake[2], Y. Wakabayashi[1], K. Niki[2], M. Okada[2], H. Ishiyama[2],
Y. Hirayama[2], N. Imai[2], S.C. Jeong[2], T. Shima[3], S. Mitsuoka[1],
K. Nishio[1], I. Nishinaka[1] and S. Chiba[1]

The $^{12}C(\alpha,\gamma)^{16}O$ reaction plays an important role in stellar evolution at the stage of helium-burning. Its reaction rate determines the mass fraction of ^{12}C and ^{16}O, the abundance distribution of the elements between oxygen and iron, the iron-core mass before supernovae explosion [1]. Therefore, it is quite important to accurately determine the cross section at center of mass energy of $E_{c.m.}$ = 0.3 MeV. The direct measurement of the cross section at $E_{c.m.}$ = 0.3 MeV, however, is not possible using current experimental technique, because the cross section is too small, around 10^{-17} barn. Hence one has to derive the cross section by extrapolating a directly measured cross section at $E_{c.m.}$ > 1.0 MeV into the range of stellar temperature. However, estimated cross section at $E_{c.m.}$ = 0.3 MeV still has a large uncertainty. In order to provide a stringent constrain to extrapolation down to $E_{c.m.}$ = 0.3 MeV, we designed new measurement at TRIAC. With use of the 18 GHz electron cyclotron resonance ion source [2] set upstream of the TRIAC accelerators, TRIAC has a possibility to deliver intense α-beams.

Because the Split Coaxial RFQ (SCRFQ), which is one of the TRIAC accelerators, has a radio frequency of 26 MHz, the bunch interval of the α-beams provided by TRIAC becomes 38.5 ns. On the other hand, the bunch interval is required to be that of 250 ns or more for removing the background events due to neutrons from $^{13}C(\alpha,n)^{16}O$ reaction with TOF method [3]. Therefore, we have developed and installed the sawtooth-wave pre-buncher system, coupled to multilayer chopper, with a variable bunching frequency of 2-4 MHz upstream of the SCRFQ [4,5]. When one sets the bunching frequency to be 2 MHz, 13 micro bunches are included in one bunching cycle as shown in Fig. 1(a). Time structure of α-beams was changed by using the pre-buncher as shown in Fig. 1(b), where α particles in one bunching cycle were gathered in the center micro bunch by help of the pre-buncher. In addition, the number of background α particles was well suppressed to be $5x10^{-5}$ of the pulsed α particles by using the chopper.

With use of this pulsed α-beams, the high efficiency anti-Compton NaI(Tl) spectrometers [3] and enriched carbon targets (99.99% enrichment in ^{12}C), we measured the γ-ray spectrum of the $^{12}C(\alpha,\gamma)^{16}O$ reaction at incident energy of E_α = 2.8, 3.1 and 4.5 MeV. Obtained γ-ray correlation spectrum of the energies and coincident times between the γ-ray detections and RF signals from the TRIAC accelerators measured at E_α = 2.8 MeV is shown in Fig. 2. The characteristic 9 MeV γ-ray events from the $^{12}C(\alpha,\gamma)^{16}O$ reaction are shown at 210 ns as a part of prompt events indicated in a circle on the Fig. 2. Note that since the separation energy of ^{16}O into $^{12}C + \alpha$ is 7.16 MeV, the characteristic γ-ray energy feeding from the α capture state by

[1] Japan Atomic Energy Agency (JAEA)
[2] High Energy Accelerator Research Organization (KEK)
[3] Osaka University

^{12}C to the ground state in ^{16}O is about 9 MeV at E_α = 2.8 MeV. The γ-ray yields from the $^{12}C(\alpha,\gamma)^{16}O$ reaction will be deduced from the area of 9 MeV γ-ray peak. The data analysis to determine the absolute cross section is now in progress.

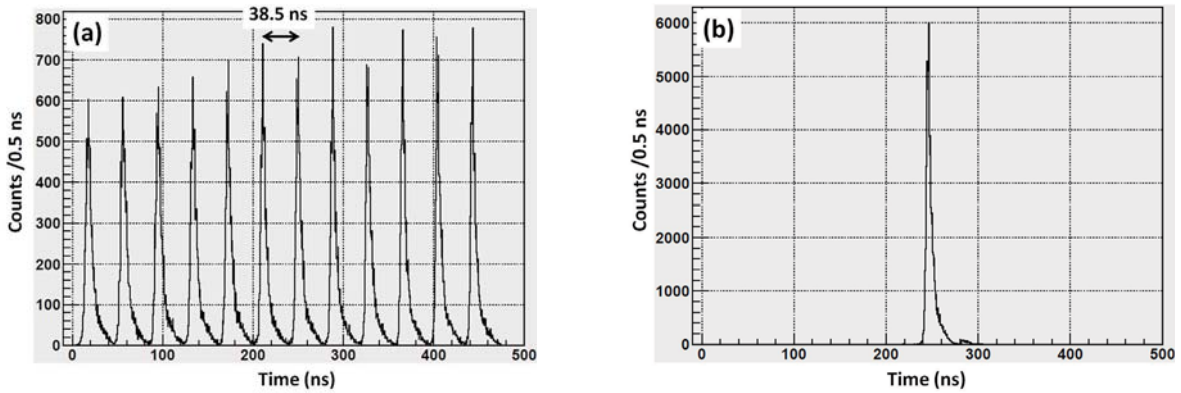

Fig. 1 Time structures of the α beams provided by the TRIAC accelerators without the pre-buncher and the chopper (a), and with the pre-buncher and the chopper (b).

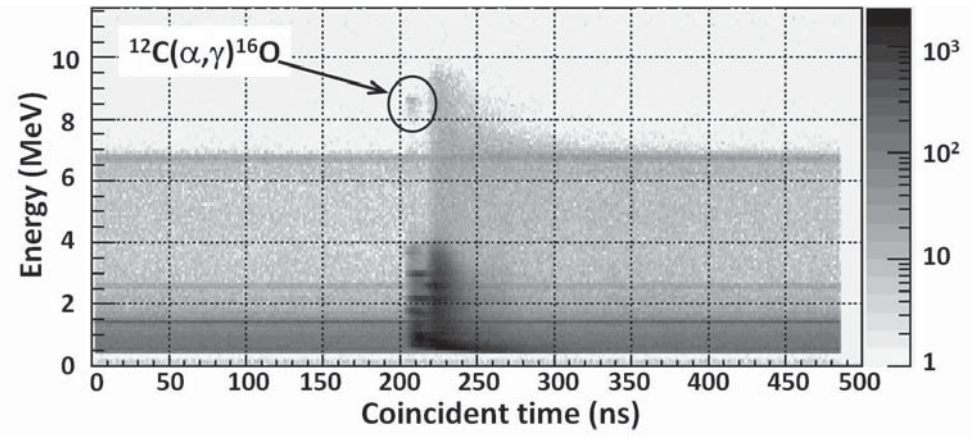

Fig. 2 Observed γ-ray correlations in the energy and the time at the $^{12}C(\alpha,\gamma)^{16}O$ reaction using pulsed α-beams at E_α = 2.8 MeV. Vertical and horizontal axes correspond to the observed γ-ray energy and coincident times between the γ-ray detections and RF signals from the TRIAC accelerators, respectively. The γ-rays from the $^{12}C(\alpha,\gamma)^{16}O$ reaction are shown inside of the circle.

References

[1] T. A. Weaver and S.E. Woosley, Phys. Rep., 227 (1993)65-96.

[2] M. Oyaizu et al., Rev. Sci Instrum., 73 (2002)806-808.

[3] H. Makii et al., Nucl. Instrum. Methods Phys. Res., A547 (2005)411-423.

[4] K. Niki et al., Proceedings of IPAC'10, Kyoto, Japan (2010)3903-3905.

[5] M. Okada et al., Proceedings of IPAC'10, Kyoto, Japan (2010)3906-3908.

3.4 Development of Si ΔE-E detector for detection of light ions

H. Makii[1], T. Ishii[1], R. Takahashi[2], Y. Wakabayashi[1], I. Nishinaka[1], S. Mitsuoka[1],
S. Chiba[1], H. Miyatake[3], S.C. Jeong[3], N. Imai[3] and Y. Hirayama[3]

Neutron-capture [(n,γ)] cross section with unstable nuclei plays an important role in the stellar nucleosynthesis [1]. However, measurement of the (n,γ) cross section of the unstable nuclei at stellar temperature range ($kT \approx 8 \sim 90$ keV) are very difficult. The main reasons of the difficulty are due to a sample preparation and/or radioactivity of the sample. Recently, light-ion induced reactions, such as (^{3}He,pγ), (d, pγ), (^{3}He,^{3}He'γ), and (^{3}He, ^{4}Heγ) reactions, have been proposed as surrogate reactions for (n,γ) reactions [2-4] on the basis of the assumption that the formation and decay of a composite nucleus are independent of each other. In order to confirm the feasibility of the ^{3}He induced surrogate reactions for determination of the (n,γ) cross sections, we are now preparing new measurement.

So far, we used Si Δ*E*-*E* detector to measure the heavy-ion induced transfer reactions using ^{18}O and ^{16}O beams, and actinide targets [5-10]. In these experiments excitation energy of residual nuclei is obtained from the sum of energy losses of outgoing projectile-like particles in a Si Δ*E* detector and Si *E* detector. Here the thickness of the Si *E* detector is 300 - 500 μm, because typical ranges of outgoing projectile-like particles (such as 160 MeV ^{16}O) in Si are about 200 μm. On the other hand, one need thicker Si *E* detector to detect light ions such as *p*, *d*, *t*, ^{3}He,and ^{4}He, since the range of *p*, whose typical energy is above 20 MeV, exceeds 500 μm in Si. Hence we have developed a Si Δ*E*-*E* detector to detect the outgoing light ions. This Si Δ*E*-*E* detector consists of two surface-barrier type Si detectors with a thickness of 75 μm (Δ*E* detector) and 4 mm (*E* detector), and has three annular active-areas covering angle ranges of 123° - 130°, 130° - 140°, and 140° - 152° with respect to the beam axis, respectively. Energy resolution obtained from this Si Δ*E*-*E* detector was checked by using a 0.35 mg/cm^2 ^{196}Pt self-support target (94.6% enrichment in ^{196}Pt) and a 24 MeV ^{3}He beam.

Fig. 1 shows an energy spectrum of the outgoing projectile-like particles, which obtained by the sum of energy losses in the second annular active-area (covering an angle range of 130° - 140° with respect to the beam axis) of the Si Δ*E* detector and Si *E* detector. The energy resolution of the peak from the elastic scattering is about 210 keV in FWHM (0.9 %), which is enough to measure the ^{3}He induced reactions. Note that obtained energy resolution was affected by not only energy resolution of the Si detectors but energy losses in target, geometrical stragglings due to finite sizes of the incident ^{3}He beam and the Si detectors, and so on. We will use this Si Δ*E*-*E* detector to detect the outgoing projectile-like particles from ^{3}He induced surrogate reactions in coincidence with γ rays from the residual nuclei.

[1] Japan Atomic Energy Agency (JAEA)
[2] Tokyo University of Science
[3] High Energy Accelerator Research Organization (KEK)

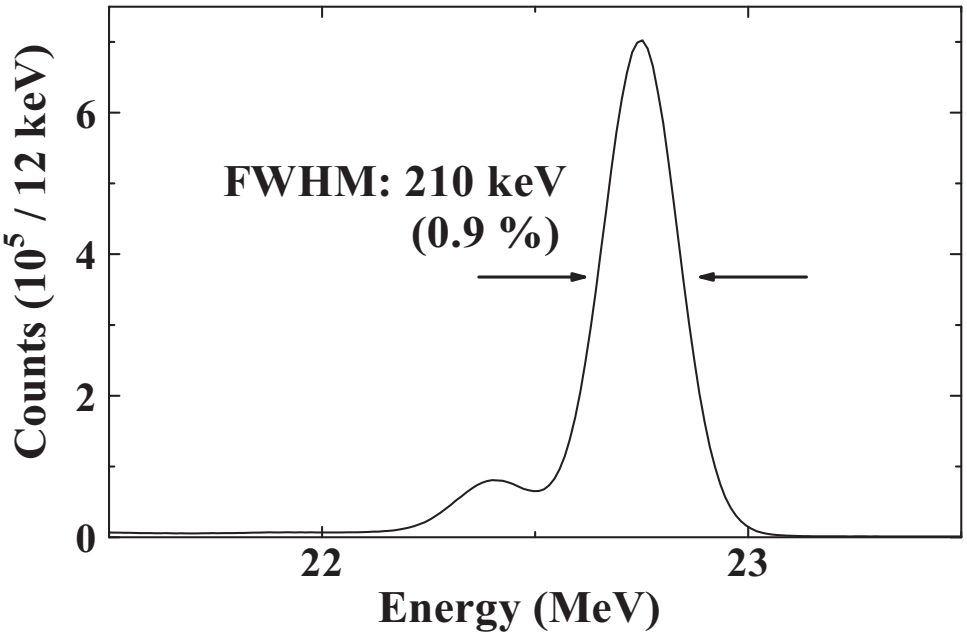

Fig. 1 Energy spectrum of the outgoing projectile-like particles. This spectrum was obtained by the sum of energy losses in the second annular active-area of the Si Δ*E* detector and Si *E* detector.

References

[1] F. Käppeler and A. Mengoni, Nucl. Phys., A777(2006)291-310.
[2] S. Boyer et al., Nucl. Phys., A775(2006)175-187.
[3] B.L.Goldblum et al., Phys. Rev., C78(2008)064606.
[4] J.M. Allmond et al., Phys. Rev., C79(2009)054610.
[5] T. Ishii et al., Phys. Rev., C72(2005)021301(R).
[6] T. Ishii et al., J. Phys. Soc. Jpn., 75(2006)043201.
[7] T. Ishii et al., Phys. Rev., C76(2007)011303(R).
[8] H. Makii et al., Phys. Rev., C76(2007)061301(R).
[9] T. Ishii et al., Phys. Rev., C78(2008)054309.
[10] R. Takahashi et al., Phys. Rev., C81 (2010)057303.

CHAPTER 4

Nuclear Chemistry

4.1 Determination of the reduction potential of mendelevium between 2+ and 3+ states using an electrochemistry apparatus
4.2 Development of a surface-ionization-type ion-source for the measurement of the first ionization potential of Lr
4.3 On-line isothermal gas chromatographic behavior of group-5 elements as homologues of Db
4.4 Studies on volatile behavior of Zr and Hf chlorides
4.5 Anion-exchange behavior of the group-6 elements in HF/HNO_3 mixed solutions
4.6 Solvent extraction of Bk and Md into HDEHP from HNO_3 solution
4.7 Production of radioactive astatine isotopes using lithium ion beams
4.8 Production of medical radio isotopes ^{95m}Tc

This is a blank page.

4.1 Determination of the reduction potential of mendelevium between 2+ and 3+ states using an electrochemistry apparatus

A. Toyoshima[1], M. Asai[1], Z. J. Li[1], N. Sato[1], T.K. Sato[1], K. Ooe[1], T. Kikuchi[1], Y. Kaneya[1], Y. Kitatsuji[1], K. Tsukada[1], Y. Nagame[1], M. Schädel[1,2], Y. Kasamatsu[3], Y. Kogama[3], A. Shinohara[3], H. Haba[4] and J. Even[5]

The determination of redox potentials of the heaviest actinides between divalent and trivalent states can shed light on the stability of 5f electrons. Due to stronger binding of 5f electrons with increasing atomic number, divalent states are predicted to be stabilized at the end of the actinide series. Recently, we have developed an electrochemistry apparatus with chromatographic separation technique for single atom chemistry [1]. Carbon fibers modified with Nafion were employed as a working electrode for cation-exchange separation. In our previous report, we presented the excitation function of the ^{248}Cm(^{11}B, 4*n*)^{255}Md reaction to find optimum production conditions and the reduction of Md^{3+} to Md^{2+} using an electrochemistry apparatus. In the present study, the redox potential of Md between Md^{2+} and Md^{3+} was determined with this apparatus.

The ^{255}Md isotope with a half-life of 27 min was produced in the ^{248}Cm(^{11}B, 4n) reaction at the JAEA tandem accelerator. The 525 μg/cm^2 ^{248}Cm target was prepared by electrodeposition of a Cm compound in 2-propanol onto a Be backing foil of 1.80 mg/cm^2 thickness. The $^{11}B^{4+}$ beam intensity was 780 nA (particle) on average. The 63.2 MeV ^{11}B ions passed through a 2.08 mg/cm^2 HAVAR window, 0.13 mg/cm^2 He cooling gas, and the Be backing foil before entering the ^{248}Cm target material with a beam energy of 57.8 MeV. At this energy, the excitation function shows a maximum production cross section of ~4 μb. Reaction products recoiling out of the Cm target were then transported to a chemistry laboratory by a He/KCl gas-jet method at a gas flow rate of 2.4 L/min. Transported products were repeatedly deposited in an automated rapid chemistry apparatus for 10 min. After 90 min collection, these products were dissolved in 0.1 M HCl and were loaded onto a 30 mm long and 7 mm i.d. HDEHP chromatographic column for separation of KCl. This was necessary because large amounts of KCl impair the energy resolution in α-spectrometry. Subsequently, Md fractions, eluted in 6 M HCl, were dried, were dissolved in 20 μL of 0.10 M HCl, and were fed into the column of our reduction apparatus. Potentials between -0.3 and -0.9 V vs. a Ag/AgCl reference electrode were applied on the working electrode and 0.10 M HCl was passed through the column at a flow rate of 0.8 mL/min. To reduce dissolved oxygen which prevents a quantitative reduction of Md, the modified electrode was preconditioned for 3 min with an electrolyzed 0.10 M HCl solution. This solution had first passed through another flow electrolytic column at an applied potential of -1.5 V. To search for the elution position of Md, the effluent from the main column electrode was collected

[1] Japan Atomic Energy Agency (JAEA)
[2] GSI Helmholtzzentrum für Schwerionenforschung GmbH
[3] Osaka University
[4] RIKEN
[5] Universität Mainz

on eight Ta discs with a volume of 240 μL each. Remaining products were stripped from the electrode with 600 μL of 3.0 M HCl and were collected on two Ta discs. After evaporation, these 10 samples were subjected to α-spectrometry with 10 PIPS detectors. Counting efficiency and energy resolution of the present arrangement between detectors and samples were ~30% and ~60 keV (FWHM), respectively. Gamma rays of ^{250}Bk, a nuclear reaction by-product used to monitoer the behavior of trivalent ions, were measured with Ge detectors. The procedure was accomplished within 12 min. The chemical yield of ^{255}Md was ~12%.

Figures 1(a) and 1(b) show the elution behavior of ^{255}Md and ^{250}Bk at the applied potentials of -0.3 and -0.6 V, respectively. At both potentials, $^{250}Bk^{3+}$ is not eluted with 0.10 M HCl and is stripped with 3.0 M HCl, showing that trivalent ions are strongly retained on the column electrode in an elution with 0.10 M HCl. At -0.3 V, only a small part of Md is eluted with 0.10 M HCl. In our previous reduction experiment with Eu, the elution of Eu^{2+} with 0.10 M HCl was clearly observed on sufficiently negative potentials. The present result, thus, shows that a small fraction of Md^{3+} is reduced to Md^{2+} and is eluted in 0.10 M HCl at -0.3 V. However, at -0.6 V, ^{255}Md is completely eluted with 0.10 M HCl. This unambiguously exhibits that Md^{3+} is completely reduced to Md^{2+}. By variation of the applied potential it was determined that the reduction probability of Md sharply increases when decreasing the applied potential from -0.3 to -0.6 V, showing quantitative reduction of Md. The redox potential of the $Md^{2+} \rightleftarrows Md^{3+} + e^-$ reaction was preliminarily evaluated to be -0.40 ± 0.03 V referred to a Ag/AgCl electrode which corresponds to the value of -0.18 ± 0.03 V vs. a standard hydrogen electrode.

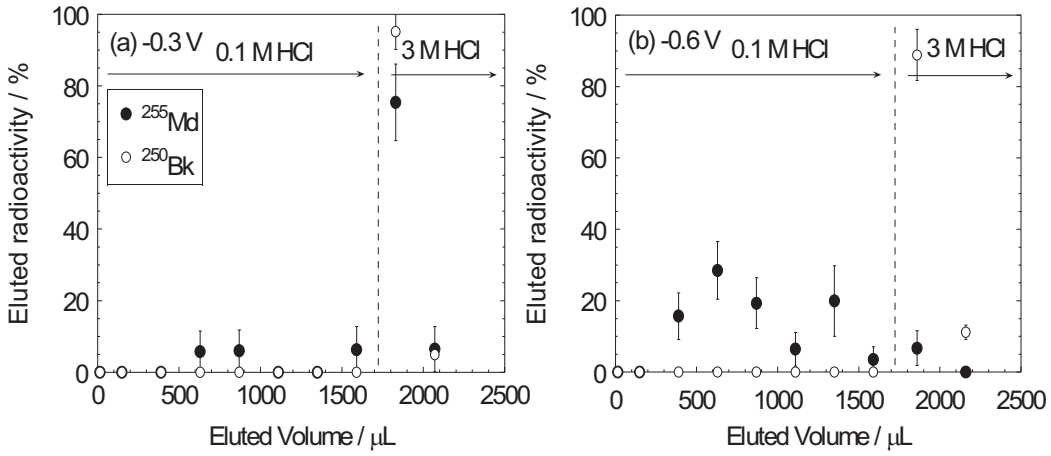

Fig. 1 Elution behavior of ^{255}Md and ^{250}Bk at applied potentials of (a)-0.3 V and (b) -0.6 V.

Reference

[1] A. Toyoshima et al., Radiochim. Acta, 96(2008)323-326.

4.2 Development of a surface-ionization-type ion-source for the measurement of the first ionization potential of Lr

N. Sato[1], T.K. Sato[1], M. Asai[1], S. Ichikawa[2], K. Tsukada[1], A. Toyoshima[1], Z.J. Li[1], T. Kikuchi[1], Y. Kaneya[1], Y. Nagame[1] and M. Schädel[1,3]

Studying the valence electronic structure of heaviest elements is an important subject in the field of nuclear chemistry. One of the most sensitive atomic properties to the structure is the first ionization potential (IP) which reflects the stability of an outermost electron affected by strong relativistic effects. The ground-state electronic configuration of the last actinide, lawrencium (Lr) is predicted to be [Rn]$5f^{14}7s^2 7p$ which is different from that of the lanthanide homologue Lu, [Xe]$4f^{14}6s^2 5d$ [1], because the $7p$ orbital of Lr is stabilized below the $6d$ orbital by the strong relativistic effects. The weakly-bound outermost electron causes low IP of Lr compared to those of other actinides [2]. Due to low production rate and short half-lives, IPs of the heaviest elements must be measured on an atom-at-a-time scale. To determine the IP of Lr based on the surface ionization comparison technique [3] which was used for IP measurement of lanthanides, we are developing a surface-ionization-type ion-source [4]. As a model of the Lr experiment, we measured ionization efficiencies of lanthanides versus ion-source temperature.

A schematic view of the experimental setup is shown in Fig. 1. Short-lived lanthanide isotopes were produced in the ^{136}Ce/^{141}Pr/^{159}Tb + ^{11}B, ^{136}Ce/^{141}Pr/^{159}Tb + ^{12}C, and ^{142}Nd/^{147}Sm/^{nat}Eu + ^{12}C reactions at the JAEA tandem accelerator facility. Nuclear reaction products recoiling out of the target were stopped in helium gas, attached CdI_2 aerosols generated by sublimation of CdI_2 powder at 290 ^{o}C, and were transported to the ion-source with a He/CdI_2 gas-jet system through a Teflon capillary of 1.5 mm i.d. and 8.8 m length. The helium gas flow rate was 1.4 L/min. The ion-source made of tungsten was heated up to 2300 ^{o}C by radiant heat and by thermal electron bombardment from a surrounding filament. Ionized nuclides were accelerated by electrical potential of 30 kV and were mass-separated with an ISOL. Then, ions were implanted into an Al-coated Mylar tape and γ-rays were measured with a Ge detector. Production yields were measured in separate experiments using a catcher system.

Figure 2 shows the ionizer-temperature dependence of ionization efficiencies for typical elements. High efficiencies of 48%, 15%, and 8% were attained for Eu, Dy, and Lu, respectively at 2300 ^{o}C. The experimental data were analyzed with the Saha-Langmuir equation: $\frac{N^+}{N^0} = \exp\left(\frac{\varphi - IP}{kT}\right)$, where N^+ and N_0 are the number of ions and neutral atoms in the ionizer, respectively, φ is a work function of the ionizer surface, k is the Boltzmann constant, and T is the temperature. Experimental IP values were evaluated from ionization efficiency slopes. As shown in Fig. 3, present IP values of elements with high boiling points

[1] Japan Atomic Energy Agency (JAEA)
[2] RIKEN
[3] GSI Helmholtzzentrum für Schwerionenforschung GmbH

(B.P.s) are higher than literature values [5]. Difference in IPs between experimental data and literature values [5] become large with increasing the B.P. of the elements. These results suggest that ionization efficiency is affected by not only IP but also B.P of each element. To obtain the IP of Lr with our apparatus, an effect of the B.P. has to be also considered into account.

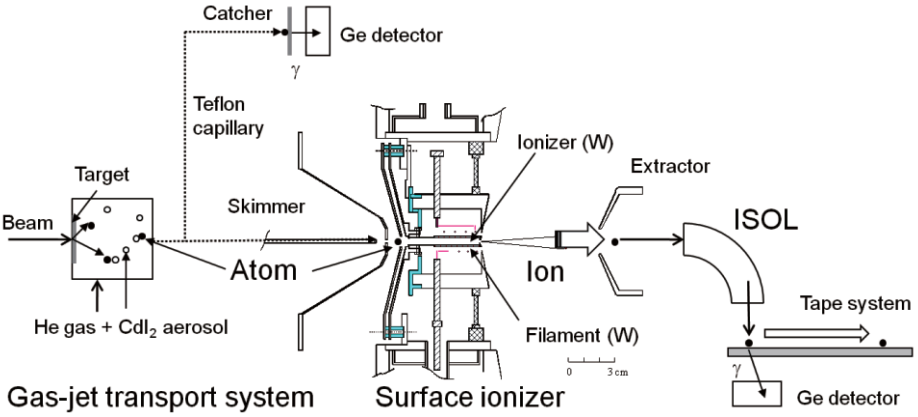

Fig. 1 Schematic view of the experimental setup.

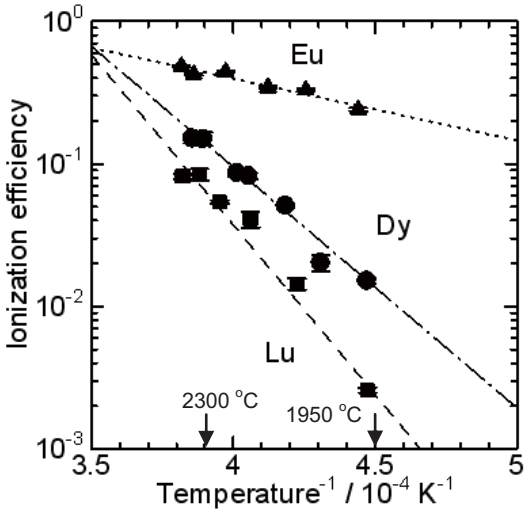

Fig. 2 Ionization efficiency versus the inverse of temperature. Lines show the exponential curve fitting results for each element.

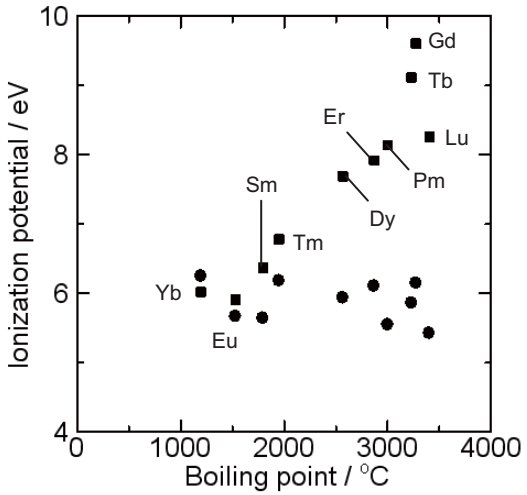

Fig. 3 Boiling point dependence of the IP values. Squares and circles represent experimental data and literature values [5], respectively.

References

[1] Y. Zou, C. Froese Fischer, Phys. Rev. Lett., 88(2002)183001-1-4.

[2] A. Borchevsky et al., Eur. Phys. J., D45 (2007)115-119.

[3] G. R. Hertel, J. Chem. Phys., 48(1968)2053-2058 and references therein.

[4] S. Ichikawa et al., Nucl. Instrum. Methods Phys. Res., B187(2002)548-554.

[5] D. R. Lide (Editor), Handbook of Chemistry and Physics, 87th ed., CRC Press, Florida (2006) 4-133-134.

4.3 On-line isothermal gas chromatographic behavior of group-5 elements as homologues of Db

T. K. Sato[1], K. Tsukada[1], M. Asai[1], A. Toyoshima[1], Y. Kasamatsu[2],
Z. J. Li[1], N. Sato[1], T. Kikuchi[3], Y. Nagame[1] and M. Schädel[1]

Dubnium (Db, Z=105), one of transactinide elements, is expected to be a member of group-5 and a homologue of V, Nb, and Ta according to its place in the Periodic Table. In a gas phase the group-5 elements are most stable in their maximum oxidation state +5 and therefore form pentachlorides and/or oxychlorides in chlorinating atmosphere. Oxychlorides are less volatile than the pentachlorides. Chemical properties of Db compounds in a gas phase have been still ambiguous since it was only reported that the retention behavior of chlorides of Db had two components at least in an isothermal gas chromatography. The multi components would be caused by production of both pentachloride and oxychloride owing to contamination of oxygen[1]. In this work, we performed on-line experiments with short-lived Nb and Ta isotopes as the homologues of Db with our isothermal gas chromatographic apparatus under conditions to form only oxychloride species in order to compare volatilities of the same species among Db, Nb and Ta, each other. In addition, we attempted to observe volatile compounds of Db under the identical conditions.

Short-lived Nb and Ta isotopes were produced in the reactions of ^{nat}Ge (^{19}F, xn)^{87,88}Nb ($T_{1/2}$ = 3.7/14.5 min) and ^{nat}Gd (^{19}F, xn)^{169,170}Ta ($T_{1/2}$ = 4.9/6.7 min), respectively, at the JAEA Tandem accelerator facility. The nuclear reaction products were transported to the on-line isothermal gas chromatographic apparatus by a carrier gas flow. The chemical apparatus was described in [2]. A mixture of 0.9 L/min of He and 0.1 L/min of N_2 was used as a carrier gas. Nitrogen saturated with $SOCl_2$ vapor with 1 % oxygen concentration was employed as a reactive gas to produce volatile oxychlorides of Nb and Ta. Volatile compounds after separation were transported to a collection site in a chemistry laboratory by a He/KCl gas-jet method for γ-ray measurements. An HP-Ge detector was used to measure the γ-rays of each nuclide. We measured yields of the volatile compounds of ^{87,88}Nb and ^{169,170}Ta passing through the column as a function of isothermal temperature. These results were compared with direct measurements of the recoil products from the target using an Al catcher foil to determine overall efficiencies.

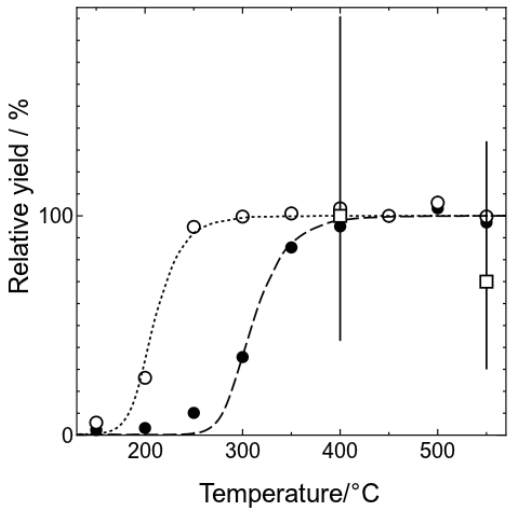

Fig.1 Relative yields of ^{88}Nb(○) and ^{170}Ta(●) as a function of isothermal temperature with the relative yields of ^{262}Db(□) at isothermal temperature of 400 and 550 °C. The yield curves were analyzed with the Monte Carlo model.

[1] Japan Atomic Energy Agency (JAEA).
[2] Osaka University.
[3] Ibaraki University.

Figure 1 shows the variations of the relative yields of ^{88}Nb and ^{170}Ta as a function of isothermal temperature. The overall efficiencies were about 10 % at maximum for Nb and Ta. The maximum yields were normalized to 100%. The each behavior of Nb and Ta had one component. It indicates that only one chemical species was formed, which was oxychloride, since a small amount of oxygen was added to the reactive gas. The adsorption enthalpies (ΔHa) of the oxychlorides of Nb and Ta were evaluated by a Monte Carlo code to reproduce experimental isothermal gas chromatographic behavior based on a microscopic model of gas-solid thermochromatography in open columns proposed by Zvara[5]. The calculations were applied to the behaviors of ^{87,88}Nb and ^{169,170}Ta. The resulting adsorption enthalpies were $\Delta Ha(NbOCl_3)$ = -105±3 kJ/mol and $\Delta Ha(TaOCl_3)$ = -126±2 kJ/mol. In Table 1, a compilation of experimental ΔHa-values from the literature, measured for carrier free amounts of $NbOCl_3$ and $TaOCl_3$ on quartz surfaces, along with the results from this work, is shown. The ΔHa-values obtained in this work were in good agreement with the literature values while that of $NbOCl_3$ was slightly higher than those values.

In the identical chemical conditions, observation of volatile compounds of Db was also performed. ^{262}Db was produced in the reaction of ^{248}Cm(^{19}F, 5n) with ~500 μg/cm^2 thick ^{248}Cm target and about 250 pnA of ^{19}F beam. Chemically separated products carried by the He/KCl gas-jet were collected and measured with a rotating wheel α-particle detection system (MANON) which has 6-pairs of Si-PIN photodiodes. Isothermal column temperature were kept at 400 and 550 °C. The ^{262}Db nuclide is identified based on α-α correlations originating from the α decay of ^{262}Db followed by the α decay of the ^{258}Lr. In this experiments, 3-pairs of the α-α correlations were detected in each isothermal temperature. The number α-α correlations were normalized to the beam integral and to the yield observed at 400°C as shown in Fig.1. It was found that Db would form volatile compounds under the chlorinating conditions including small amount of oxygen.

Table 1. Experimentally determined adsorption enthalpies on quartz surfaces of oxychlorids of Nb and Ta from this work and from literature data.

Chemical species	$T_{1/2}$	-□Ha /kJ mol-1	Chlorinating agent	Reference
$^{87,88}NbOCl_3$	3.7/14.5 min	105±3	$SOCl_2$ (O_2 1%)	This work
$^{97m}NbOCl_3$	52.7 s	96±3	CCl_4/H_2O	[3]
$^{99g}NbOCl_3$	15 s	99±1	HCl (99.8%)	[1]
$^{169,170}TaOCl_3$	4.9/6.8 min	126±2	$SOCl_2$ (O_2 1%)	This work
$TaOCl_3$	Long -lived	133±20	CCl_4	[4]

References

[1] A. Turler et al., Radiochim. Acta, 73(1996)55-66.
[2] T. K. Sato et al., JAEA-Review, 2009-036(2009)69-70.
[3] J. Rudolph et al., Radiochim. Acta, 27(1980)105-108.
[4] J. Rudolph et al., J. Chromatograph, 178(1979)459-469.
[5] I. Zvara, Radiochim. Acta, 38(1985)95-101.

4.4 Studies on volatile behavior of Zr and Hf chlorides

S. Goto[1], H. Murayama[1], T. Kojima[1], M. Murakami[1], H. Kudo[1],
K. Tsukada[2], M. Asai[2], T. K. Sato[2], N. Sato[2], A. Toyoshima[2] and Y. Nagame[2]

In order to clarify chemical properties of superheavy elements, a technique of a gas phase chemical separation has been applied to the chemistry experiments because it allows separating them continuously and rapidly. Adsorption enthalpies of volatile compounds of these elements can be determined from their adsorption-desorption processes on a surface of gas chromatograph column. In this study, we investigated gas chromatographic behavior of volatile chloride compounds of Zr and Hf for the study of Rf.

The Zr and Hf isotopes with various half-lives were produced in the ^{nat}Ge and ^{nat}Gd(^{16}O, *x*n), ^{nat}Ge and ^{nat}Gd(^{18}O, *x*n), and ^{nat}Ga and ^{nat}Eu(^{19}F, *x*n) reactions at the JAEA tandem accelerator facility. Nuclear reaction products were transported to the gas chromatographic apparatus with attaching on a carbon cluster in a He carrier gas flow. The carbon cluster was produced by the DC pulse discharge between carbon electrodes. The transported products were collected on a quartz wool plugged in a quartz tube where a reactive HCl gas was added to form volatile chloride compounds. The formed volatile compounds were then fed into an isothermal chromatographic quartz column directly connected to the tube. The compounds of Zr and Hf through the column were re-tranported attaching on a KCl cluster in a He carrier gas flow, and collected on a glass filter for γ-rays measurement to examine the yields of these elements which passed through the column. The passed-through yields for Zr and Hf were obtained as a function of the temperature of the isothermal column.

The yields of ^{85}Zr ($T_{1/2}$ = 7.9 min) and ^{166}Hf ($T_{1/2}$ = 6.8 min) increased with the temperature of the column between 300 and 450 °C, and isothermalchromatographic behavior of both was very similar, which is in good agreement with the previous report [1]. Furthermore, the temperature to increase the yield for ^{165}Hf ($T_{1/2}$ = 76 s) came higher than that for ^{166}Hf. The chromatograms of ^{165}Hf and ^{166}Hf are shown in Fig. 1. These indicate that the adsorption-desorpiton model considered so far [2] is appropriate. The overall efficiency to re-transportation was about 6% for ^{165}Hf at the column temperature of 450 °C. This efficiency corresponds to 84 counts of ^{261}Rf during 10 hours. It will be enough efficiency for ^{261}Rf ($T_{1/2}$ = 68 s) experiment.

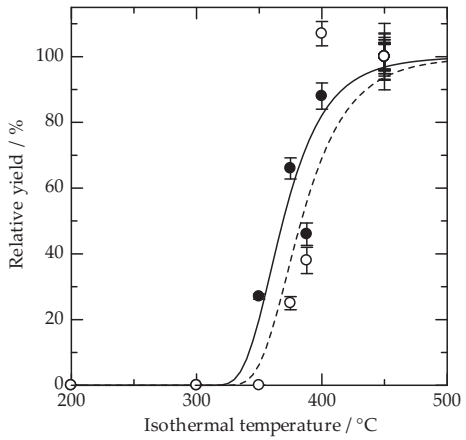

Fig. 1 Isothermal chromatograms of Hf isotopes. Open symbols and dashed line are ^{166}Hf, and closed symbol and solid line are ^{165}Hf.

References

[1] T. K. Sato et al., J. Nucl. and Radiochem. Sci., 6(2005)N1–N3.
[2] I. Zvara, Radiochim. Acta, 38(1985)95–101.

4.5 Anion-exchange behavior of the group-6 elements in HF/HNO_3 mixed solutions - Towards the study of ion-exchange behavior of $_{106}$Sg -

X. H. Liang[1], K. Tsukada[1], Z.J. Li[1], A. Toyoshima[1], M. Asai[1], T. K.Sato[1],
N. Sato[1], T. Kikuchi[1], Y. Kaneya[1] and Y.Nagame[1]

The aqueous phase chemistry of the group-6 elements Mo, W, and element 106 (seaborgium, Sg) has been studied by Schaedel et al. in 1997 and 1998 by chromatographic methods, and the similarity of the chemical behavior of Sg to those of its lighter homologues has been discussed [1,2]. However no experimental data for Sg in the aqueous phase chemistry has been established after the reports. For deeper understanding of the chemical properties of Sg, more detailed systematic studies are required. In the present work, prior to the Sg experiment, anion-exchange behavior of the group-6 elements, W and Mo, in HF and HNO_3 mixed solutions [3] has been studied by a batch method using the carrier-free radiotracers ^{181}W ($T_{1/2}$ = 121.2 d) and ^{93m}Mo ($T_{1/2}$ = 6.9 h).

The long-lived isotope ^{181}W was produced in the ^{181}Ta(p, n) reaction at the JAEA tandem accelerator. The ^{181}W isotope was chemically separated from the Ta target material, and was dissolved with 10^{-4} – 1.0 M HF and 0.1 M HNO_3 mixed solutions for batch experiments. On the other hand, the short-lived isotope ^{93m}Mo was produced in the ^{93}Nb(p, n) reaction. The recoiling products from the Nb target were transported to a chemical laboratory with a He/KF gas-jet system, and were dissolved with HF and HNO_3 mixed solution. The solutions containing ^{181}W or ^{93m}Mo were mixed with 5 – 200 mg anion exchange resin CA08Y. Radioactivities of the solution were assayed for γ-ray spectrometry, and then distribution coefficients (K_ds) of these elements were determined.

In Fig. 1, the variation of the K_d values of W and Mo on the anion-exchange resinin HF and 0.1 M HNO_3 mixed solutions at 70°C is plotted as a function of [HF]. It can be seen that the adsorption sequence on the

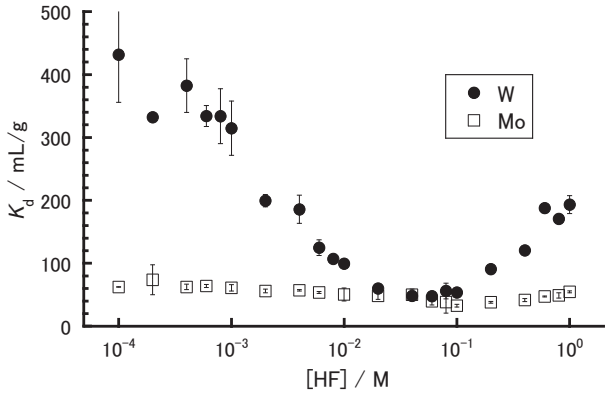

Fig. 1 Variation of the K_d values of W and Mo on the anion-exchange resin (CA08Y) as a function of [HF] in HF and 0.1 M HNO_3 mixed solutions at 70°C.

[1] Japan Atomic Energy Agency(JAEA)

anion-exchanger is W > Mo, confirming that W has a stronger ability to form fluoride complexes than Mo [3]. It was also found that the *K*d values of W depend strongly on the concentration of HF, while those of Mo are almost constant as a function of [HF] under the given conditions.

References

[1] Schädel et al., Nature, 388(1997)55.
[2] Schädel et al., Radiochim. Acta, 83(1998)156.
[3] Kronenberg et al., Radiochim. Acta, 92(2004)395.

4.6 Solvent extraction of Bk and Md into HDEHP from HNO_3 solution

Y. Kasamatsu[1], Y. Kogama[1], R. Takayama[1], H. Kikunaga[2], A. Toyoshima[3], K. Tsukada[3], M. Asai[3], T.K. Sato[3], Z.J. Li[3], N. Sato[3], T. Kikuchi[3], Y. Kaneya[3], Y. Nagame[3], K. Ooe[3], Y. Komori[1], T. Yoshimura[1], N. Takahashi[1] and A. Shinohara[1]

The lanthanide and actinide series involve the filling of the 4f and 5f subshells, respectively. The early members of the actinide series have various oxidation states in consequence of extended 5f electrons. On the other hand, the trivalent oxidation state is the most stable for lanthanides and heavy actinides from $_{95}$Am to $_{103}$Lr, except for $_{102}$No, because the f electrons exist in the inner shell and little participate in the chemical bonding. Thus, the chemical properties of trivalent lanthanides, Ln(III), and actinides, An(III), are similar to each other and systematic trends related to their ionic radii are often observed on their chemical properties. In contrast, there would be differences in chemical properties between Ln(III) and An(III) due to the relativistic effect and so on. Indeed, some reports suggest the different properties between Ln(III) and An(III) [1,2]. The chemical research on heavy actinides is, however, difficult to be performed because the production yields of artificial heavy actinides are low and the nuclides of the elements have short half-lives. Therefore, detailed and systematic studies have been few conducted. It is very important to systematically study the chemical properties of An(III) and to compare these properties with those of Ln(III) in order to discuss the properties of 4f- and 5f-elements in detail.

Previously, we systematically studied the extraction behavior of Ln(III) as well as that of $_{95}$Am, $_{96}$Cm, $_{98}$Cf, $_{99}$Es, and $_{100}$Fm into di(2-ethylhexyl) phosphoric acid (HDEHP) under identical conditions by a batch method [3]. It was confirmed that these elements are extracted as $M\{H(DEHP)_2\}_3$ (M = An(III) and Ln(III)) into organic phases containing HDEHP as reported previously [4,5]. In this work, we produced $_{97}$Bk and $_{101}$Md by using a powerful accelerator in JAEA and extraction behaviors of Bk and Md were investigated in the HDEHP/HNO_3 system.

The ^{255}Md isotope with a half-life of 27 min was produced in the ^{248}Cm(^{11}B, 4n) reaction at the JAEA tandem accelerator. The ^{250}Bk nuclide was simultaneously produced as a by-product in the above irradiation. Reaction products recoiling out of the Cm target were transported to the chemistry laboratory with a He/KCl gas-jet system. Before the extraction, the products were dissolved in 0.1 M HNO_3 and Bk and Md were separated from KCl and other by-products by a column chromatography with the HDEHP resin. Subsequently, the sample in 6 M HNO_3 was evaporated to dryness and was dissolved in 200 μL of 0.1 M HNO_3. The solution sample was mixed with 200 μL of HDEHP-benzene solution and shaken for 10 min. After a phase separation by centrifugation for 1 min, aliquots of the aqueous and organic solutions were taken and were evaporated to dryness. The dried samples were then subjected to radiation measurement (γ-ray measurement for the Bk samples and α-particle measurement for Md). The distribution ratios (D) were obtained by the equation $D = [M^{3+}]_{org}/[M^{3+}]_{aq}$. The volumes of the solutions taken were

[1] Osaka University
[2] Tohoku University
[3] Japan Atomic Energy Agency (JAEA)

evaluated from the weights and the densities of the solutions. In the extraction experiments of Bk, the *D* values were determined in 0.10, 0.16, 0.25, and 0.63 M HDEHP-benzene solutions with the collection times of the nuclear reaction products of 1.5, 0.5, 3, and 6 h, respectively. In the Md experiments, extraction experiments were repeated 9, 5, and 16 times in 0.063, 0.10, and 0.16 M HDEHP-benzene solutions, respectively, with the constant collection time of 0.5 h.

The *D* values of Bk and Md determined in this experiment are shown in Fig. 1 together with our previous data of other An(III) [3]. The data are well fitted with linear lines with the slope of +3 for Bk and Md the same as that for other An(III) and Ln(III) [3]. This indicates that Bk and Md are also extracted as $M\{H(DEHP)_2\}_3$ into the HDEHP with the concentrations in the present experiment. Thus, extraction constants K_{ex} of Bk and Md expressed by $K_{ex} = [M\{H(DEHP)_2\}_3]_{org}[H^+]_{aq}^3/[M^{3+}]_{aq}[(HDEHP)_2]_{org}^3$ were evaluated from the fitting with the equation: $\log D = \log K_{ex} - 3\log[H^+]_{aq} + 3\log[(HDEHP)_2]_{org}$ [3]. The K_{ex} values of Bk and Md are shown in Fig. 2 together with those of other An(III) and Ln(III). Tetrad effects [2] caused by the stability of the f electrons are more clearly observed in actinide elements by the addition of the present data. It also becomes clear that difference between the K_{ex} values of Ln(III) and those of An(III) would be larger for heavier elements. It is very interesting to obtain the data of $_{103}$Lr.

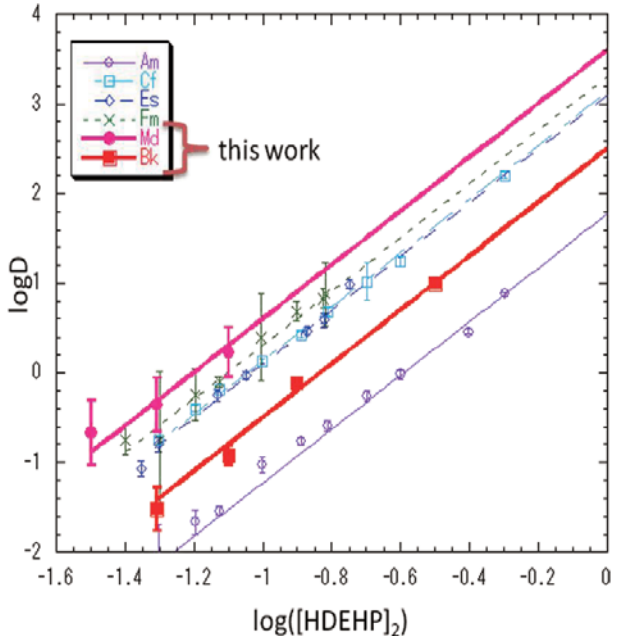

Fig. 1 Variation of log *D* of heavy actinide elements as a function of log $[(HDEHP)_2]$.

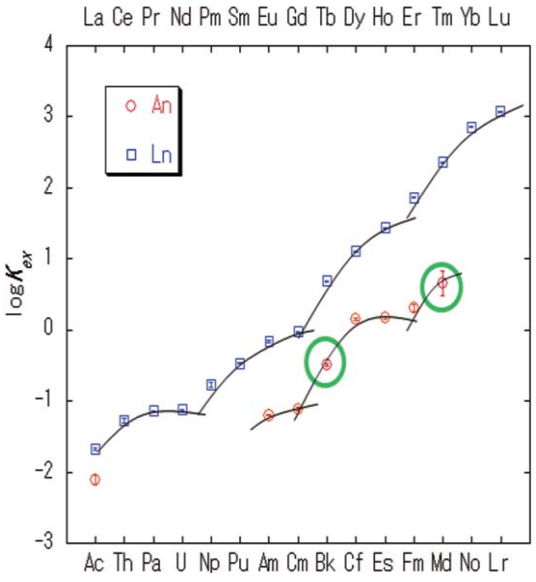

Fig. 2 Variation of log K_{ex} of lanthanides and heavy actinides against atomic number. The plots of Bk and Md are circled.

References

[1] M. P. Jensen and A. H. Bond, J. Am. Chem. Soc., 124(2002)9870.

[2] D. F. Peppard et al., J. Inorg. Nucl. Chem., 32(1970)339.

[3] R. Takayama et al., Radiochim. Acta, in press.

[4] V. N. Kosyakov and E. A. Yerin, J. Radioanal. Chem., 43(1978)37.

[5] M. Aguilar and D. H. Liem, Acta. Chem. Scand., A30(1976)313.

4.7 Production of radioactive astatine isotopes using lithium ion beams

I. Nishinaka[1], A. Yokoyama[2], K. Washiyama[2], R. Amano[2],
N. Yamada[2], R. Ishiguro[2], H. Makii[1] and K. Hashimoto[1]

An α radioactive nuclide ^{211}At with a half-life of 7.2 h is a prospective candidate for utilization in targeted alpha radiotherapy. In a general way, ^{211}At is produced through bombardment of bismuth target with 28 MeV helium ions in the ^{209}Bi(α,2n)^{211}At reaction because of the high yield required for therapeutic purpose [1]. However, the nuclear reactions using lithium ion beams, ^{6,7}Li+Pb, Bi, provide the possible production routes of ^{211}At. Excitation functions have been extensively measured for the ^{6,7}Li+ ^{209}Bi reactions to study the reaction mechanism involving complete fusion and breakup reaction of weakly bounded nuclei ^{6,7}Li [2-4]. For ^{7}Li+^{nat}Pb, however, only report on production of astatine isotopes has been available for radiotherapy [5]. Therefore, we have tried to measure excitation function of ^{211}At in the reaction of 29-48 MeV ^{7}Li+^{nat}Pb.

Bismuth targets with thickness of 0.78-0.97 mg/cm^2 were prepared by vacuum evaporation onto alminum backing sheets with thickness of 5.4 mg/cm^2. Each target was sandwiched between the backing and the catcher sheet of 5.4 mg/cm^2 aluminum. Irradiation was carried out with ^{7}Li^{3+} beams of 50 MeV from the 20 MV tandem accelerator at JAEA-Tokai. Six sets of the bismuth target, the backing and the catcher sheet were placed at a water-cooled Faraday cup as schematically shown in Fig.1. Beam current was approximately 120 nA during the irradiation of 2 h. The beam current was collected by the Faraday cup and was monitored on-line by using a current integrator module equipment connected to a multi-channel scaler (MCS) which was controlled by a personal computer. The MCS data were recorded to calibrate beam fluctuations. In the second irradiation of 2.3 h with the average beam intensity of 150 nA , an aluminum sheet of 5.4 mg/cm^2 was placed at beam upstream of five sets of the bismuth target and the aluminum sheets to change beam energies at the targets. The beam energies at the target were determined by calculating the energy loss in the targets and the sheets with the SRIM code [6]. The γ-ray spectrum measurements of radioactive products were carried out by a Ge detector. The cross section of the radioactive products, σ, was calculated by the following equation, $\sigma = C_\gamma / [\varepsilon_\gamma I_\gamma N \phi (1\text{-}e^{-\lambda T})]$, where C_γ is the counting rate of the photopeak area at the end of irradiation, ε_γ the photopeak detection efficiency, I_γ the emission probability of the γ-ray, N the number of target atoms, ϕ the beam flux, λ the decay constant, and T the irradiation time.

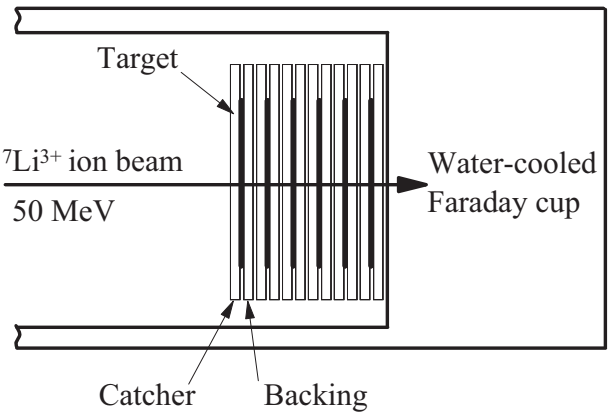

Fig. 1 Schematic view of the irradiation setup.

[1] Japan Atomic Energy Agency (JAEA)
[2] Kanazawa University

The excitation functions of astatine isotopes in the ^{7}Li+^{nat}Pb (^{204}Pb 1.4%, ^{206}Pb 24.1%, ^{207}Pb 22.1%, and ^{208}Pb 52.4%) reaction are shown in Fig. 2. Lines show the cross sections of $^{208\text{-}211}$At isotopes calculated by the HIVAP code [7]; A statistical model calculation by the HIVAP was independently carried out with the input parameters which systematically well reproduced a large number of experimental fusion-evaporation cross sections in the similar heavy ion reactions without adjusting the input parameters to fit the present experimental data [8]. It should be noted that the calculation rather well reproduces the present experimental data. It was found that the hump structure of ^{208}At around 35 MeV originated from the ^{204}Pb(^{7}Li,3n)^{208}At reaction. Larger deviations of experimental data points at 29 MeV could be due to the systematic errors of the energy loss calculation, energy struggling, or uncertainty of the statistical calculation. The calculation predicts that ^{211}At has large cross sections below 45 MeV compared with the other astatine isotopes. However, intense γ-rays of the astatine isotopes with shorter half-lives made it impossible to measure the 687 keV photopeak (I_γ= 0.26%) of ^{211}At by γ-ray spectroscopy. Thus, α-ray spectrometry will be applied to determine the excitation function of ^{211}At.

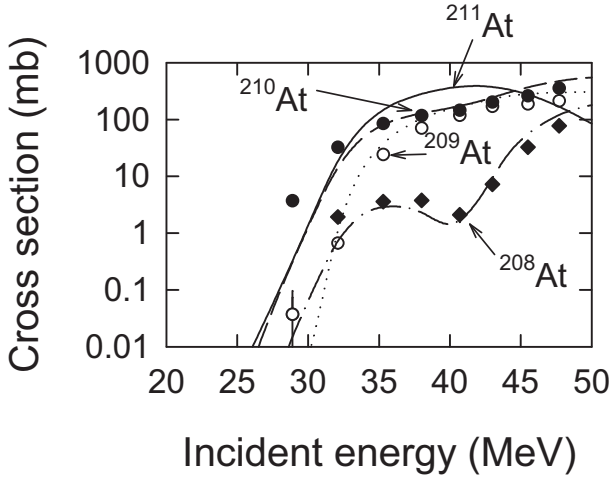

Fig. 2 Excitation functions of astatine isotopes in the ^{7}Li+^{nat}Pb reaction. The experimental and theoretical cross sections are shown by symbols and curves, respectively; solid line: ^{211}At, solid circles and dashed line: ^{210}At, open circles and dotted line: ^{209}At, and solid diamonds and dash-dotted line: ^{208}At.

References

[1] S. Lindergren, T. Bäck, H.J. Jensen, Appl. Radiat. Isot., 55(2001)157-160; S. Lindegren et al., J. Nucl. Med., 49 (2008)1537-1545.

[2] H. Freiesleven, H.C. Britt, J. Birkelund, and J.R. Huizenga, Phys. Rev., C10(1974)245-249.

[3] M. Dasgupta et al., Phys. Rev., C66(2002)04602-1-4; M. Dasgupta et al., Phys. Rev., C70(2004) 024606-1-20.

[4] Yu.E. Penionzhkevich et al., J. Phys., G36(2009)025104-1-12.

[5] K. Roy, and S. Lahiri, Appl. Radiat. Isot., 55(2008)571-576.

[6] J.F. Ziegler, J.P. Biersack and U.Littmark, *The Stopping and Range of Ions in Solids* (Pergamon, New York, 1985); http://www.srim.org/.

[7] W. Reisdorf and M. Schädel, Z. Phys., A343(1992)47.

[8] K. Nishio, private communication.

4.8 Production of medical radio isotopes ^{95m}Tc

Y. Hatsukawa[1], K. Hashimoto[1], K. Tsukada[1], M. Asai[1], T.K. Sato[1], T. Kin[1] and Y. Nagai[1]

Technetium-99m is the most successful medical radio-isotope and many kinds of labeled compounds have been developed for various diagnosis use. Recent years, with the development of the Compton camera which can realize high position resolution, medical radio-isotopes emitting high energy gamma-rays are required.

In this study, Technetium-95m which emits some gamma rays around 800 keV was produced by the ^{95}Mo(p,n)^{95m}Tc reaction. A $^{nat}MoO_3$ target of 628 mg was irradiated with 15 MeV proton beam for 7 hours. Averaged beam currents were 1.2 μA. After a week cooling time, about 700 kBq ^{95m}Tc was extracted from the irradiated MoO_3 target through the chemical purification process[1)] as shown in Fig. 1. After the chemical separation, gamma rays were measured by using a Ge-detector. A gamma-ray spectrum obtained is shown in Fig.2. Most of gamma-rays observed are assigned to ^{95m}Tc and ^{96}Tc. No gamma-ray from other elements was observed in this spectrum. This means chemical purification process was performed well. In the next stage, we will offer ^{95m}Tc obtained by this procedure for the imaging study with the Compton camera.

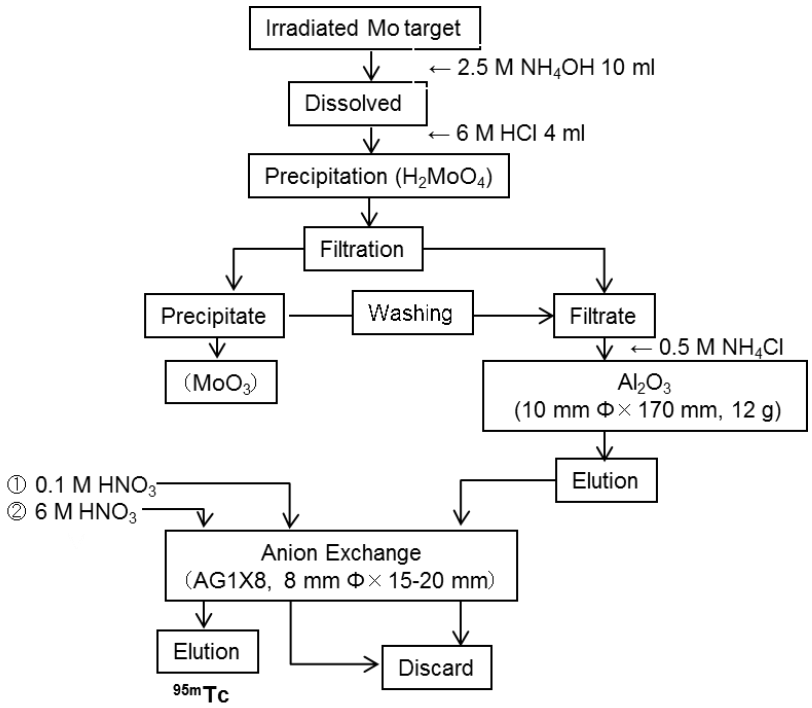

Fig.1 Flow diagram for the separation of ^{95m}Tc from a MoO_3 target.

[1] Japan Atomic Energy Agency (JAEA)

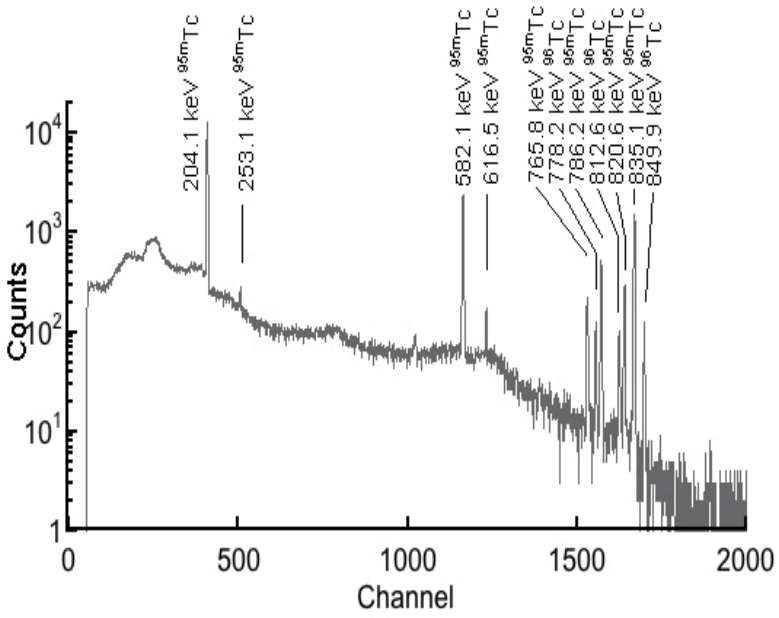

Fig. 2 Gamma ray spectrum of Tc fraction obtained from purification process.

Reference

1) M. Izumo, et al., Appl. Raiat. Isot., 42(1991)297-301.

This is a blank page.

CHAPTER 5

Nuclear Theory

5.1 Methodological and technical development in the Monte Carlo shell model
5.2 Calculation of fission barrier in the heavy and superheavy mass region by using a spherical-basis method
5.3 Spin and mass distributions of compound nucleus in surrogate reaction
5.4 Analysis of various cross sections in deuteron induced reaction with CDCC and eikonal reaction theory

This is a blank page.

5.1 Methodological and technical development in the Monte Carlo shell model

Y. Utsuno[1], N. Shimizu[2], T. Otsuka[2,3], T. Abe[2], T. Mizusaki[4] and M. Honma[5]

The nuclear shell model has been quite successful in systematically describing the nuclear structure mainly in the region of light nuclei. The limitation of the region applicable is not due to the method itself, but is due to a computational problem: as the number of valence orbits increases, it becomes practically impossible to diagonalize a shell-model Hamiltonian matrix of huge size. Currently, the largest matrix dimension diagonalizable is 10^9-10^{10} in the so-called *M*-scheme. In order to overcome the limitation, the Monte Carlo shell model (MCSM) has been developed [1]. In this report, we summarize the most recent advances of MCSM in methodology and in computational technique, with which the latest MCSM code is equipped.

Although MCSM gives rather good energies and other observables demonstrated in several benchmark cases [1], it was unclear how good the MCSM solution is *a priori*. Aiming at giving the exact solution to a good precision using the MCSM result, we introduce a novel method [2] based on the fact that there is a strong correlation between the energy $\langle H \rangle$ and its variance $\langle H^2 \rangle - \langle H \rangle^2$, where H is the Hamiltonian operator. Namely, as the wave function is reaching the eigenstate, its energy variance is vanishing. Thus, by drawing the energy vs. energy variance plot in a series of the MCSM wave functions and extrapolating the variance into zero (see Fig. 1 for an example), the exact solution can be predicted to a satisfactory extent. This method has been demonstrated to be very efficient in the conventional shell-model calculation [3], but it had not been applied to MCSM before this work because it takes much computational time to calculate the energy variance in the expression of the MCSM wave function: the summation of an eight-fold loop is required. In this work, we find that the eight-fold loop calculation can be equivalent with a six-fold loop calculation, which makes it possible to carry out realistic computation. Figure 1 demonstrates the validity of the present method for the system whose exact

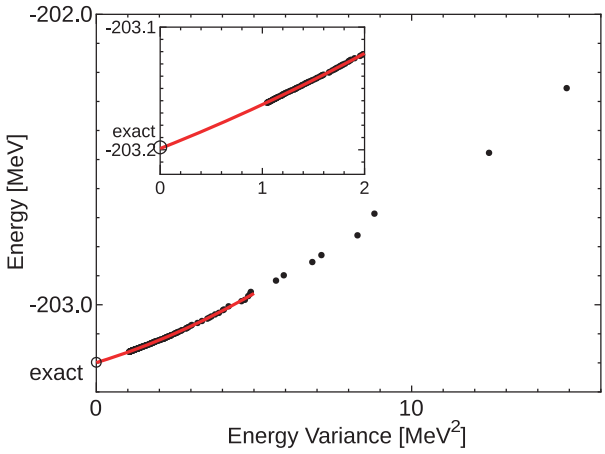

Fig. 1 Extrapolation plot for the *pf* shell calculation of ^{56}Ni compared to the exact solution. The dots are a series of the MCSM results, from which the extrapolating line is drawn.

[1] Japan Atomic Energy Agency (JAEA)
[2] University of Tokyo
[3] Michigan State University
[4] Senshu University
[5] University of Aizu

solution has been recently obtained.

Although MCSM is a powerful tool, it still takes much time to carry out the calculation. The most time-consuming part is the computation of the Hamiltonian kernel $<V> = \Sigma_{l1,l2,l3,l4} \rho_{l3,l1} v_{l1,l2;l3,l4} \rho_{l4,l2}$ where $v_{l1,l2;l3,l4} = <l1,l2|V|l3,l4>$ and ρ is the density matrix. We find a numerical algorithm which enables very fast computation of the Hamiltonian kernel [4] as briefly described below. Since $v_{l1,l2;l3,l4}$ is very sparse (i.e., most of the elements being zero) due to the symmetry of the Hamiltonian, it is not efficient to directly perform the above summation. In our old code, we adopt the so-called list-vector method in which the summation is carried out only for the indices (l1, l2, l3, l4) whose matrix element $v_{l1,l2;l3,l4}$ is non-vanishing. As another approach, the summation can be transformed to a $(\text{vector})^T \times (\text{matrix}) \times (\text{vector})$ by mapping two-dimensional arrays (l3, l1) and (l4, l2) onto one-dimensional arrays l13 and l24, respectively. This method can also avoid unnecessary operations about the vanishing matrix elements, and is named the matrix method. In MCSM, a number of the Hamiltonian kernels for different density matrices are calculated at a time. Here, the (matrix)×(vector) operations are repeated for various vectors, keeping the matrix unchanged. These operations are mathematically equivalent with (matrix)×(matrix) by binding vectors into a matrix, which is named the matrix method with binding vectors. Although those two methods are identical in the sense of mathematics, computational efficiency is quite different. Figure 2 shows the performance compared among different computational methods discussed above. The matrix method with binding vectors is most efficient and exceeds half the theoretical peak performance. This is because the (matrix)×(matrix) operation needs less memory access per floating-point operation.

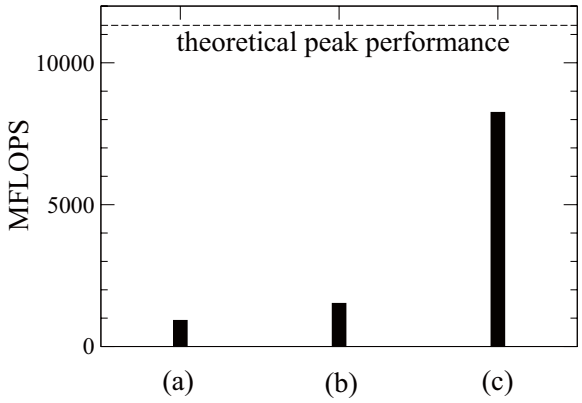

Fig. 2 Performance of the Hamiltonian-kernel computation compared among (a) the list-vector method, (b) the matrix method, and (c) the matrix method with binding vectors.

References

[1] T. Otsuka et al., Prog. Part. Nucl. Phys., 47(2001)319-400.
[2] N. Shimizu et al., Phys. Rev., C82(2010)061305(R)-1-5.
[3] T. Mizusaki and M. Imada, Phys. Rev., C65(2002)064319-1-4.
[4] Y. Utsuno et al., in preparation.

5.2 Calculation of fission barrier in the heavy and superheavy mass region by using a spherical-basis method

H. Koura[1]

The KTUY mass formula was developed for estimating the ground-state nuclear masses and gives a good reproduction of experimental nuclear masses and related energies as Q-values and separation energies [1,2]. Predictions from this method are also applied to calculation of the r-process nucleosynthesis, search for neutron and proton drip lines in the wide nuclear mass region, and so on. A notable feature of our mass formula is a method of obtaining shell energies of deformed nuclei: The shell energy of a deformed nucleus is expressed as an appropriate mixture of spherical shell energies added to an average deformation energy as

$$E_{\rm sh}(Z,N,{\rm def.}) = \sum_{Z'} W_{\rm p}(Z';Z,N)E^{\rm sph}_{\rm psh}(Z',NZ'/Z) + \sum_{N'} W_{\rm n}(N';Z,N)E^{\rm sph}_{\rm nsh}(ZN'/Z,N') + \Delta E_{\rm surf}(Z,N,{\rm def.}) - \Delta E_{\rm Coul}(Z,N,{\rm def.}) - \Delta E_{\rm pro}(Z,N,{\rm def.}),$$

Where the first two terms represent the mixture of spherical shell energies with mixing weights $W_{\rm p}$ and $W_{\rm n}$. The mixing weight is obtained from the geometrical nuclear shapes: the weight corresponds to the differentials of the solid angle measured from the center of a nucleus. When the nuclear shape is fixed, a distance from the center to the surface runs from the minor axis to the major axis with respect to θ (in spherical polar coordinates). Z' (or N') runs from $Z'_{\rm min}$ to $Z'_{\rm max}$., which are obtained from the minor axis and the major axis, respectively. The $\Delta E_{\rm surf}$ and $\Delta E_{\rm Coul}$ are the differences of Liquid-drop surface and Coulomb energies by deformation. Although our mass formula is concerned only with the equilibrium nuclear shapes, a potential energy surface for nuclear fission can be calculated with the above method by using the shell energies for arbitrary shapes. In this report we gives some results for nuclear fission. In the current study we only assume the nuclear shape is limited to an axially- and reflectionally-symmetric shape expressed as the α-expansion of up to α_6, and shapes of neutron and proton are the same.

A landscape of the calculated fission barrier heights is shown in Figure 1. There is a "basin" located around the region of (Z, N)=(110,168) and is a "hill" located around the region of (Z, N)=(98,152). The calculated heights of actinide nuclei are generally 5.5-6.5 MeV, which is in roughly consistent with fission barrier heights of known actinide nuclei. Figures 2 and 3 show two examples of deformation configuration of spherical states in the shape at the fission saddle point. The upper panel shows the spherical shell energies and the lower panel shows mixing weights. Generally, when a given radius of nucleus is a minor axis (θ=0 in spherical polar coordinates) the value of weight is the largest. In the case of $^{278}{\rm Ds}_{168}$ in Fig. 3, both of the mixing weights for proton and neutron are extent to lower closed shells, 82 of proton and 126 of neutron, respectively, and the weighted sum of spherical shell energies mutually lowers the energy due to the largest values of weights at the lowest particle numbers. In other words, the

[1]Japan Atomic Energy Agency (JAEA)

lower fission barrier of $^{278}Ds_{168}$ comes from a geometrical configuration of ^{208}Pb (doubly-magic nucleus) core + other valence particles, which is more highly evolved than that of other nuclei. In contrast with the case of $^{278}Ds_{168}$, the weighed sum of spherical shell energies of $^{252}Fm_{152}$ gives less decreasing as seen in Fig. 3 (Only the closed shell of larger neutron number, 228, slightly contributes to the lowering.) Consequently, fission barrier height of $^{252}Fm_{152}$ and neighboring ones are relatively higher than those of other nuclei.

We can give a new representation of the origin of fission barriers in the same consideration of nuclear deformations in contrast with the Nilsson-type calculation.

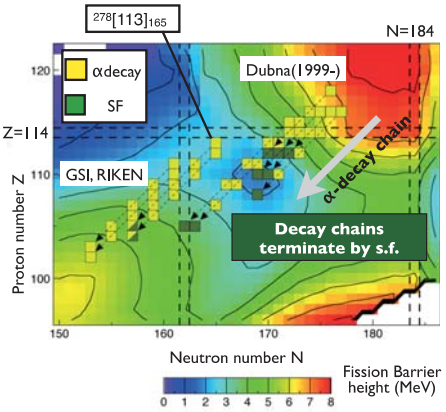

Fig. 1 Landscape of fission barrier heights in the superheavy mass region estimated with the spherical-basis method explained in this report. Some measured alpha decay chains are plotted.

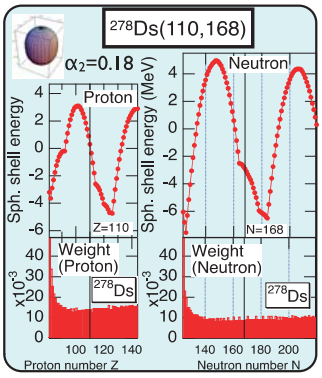

Fig. 2 Configuration mixing in the shape of fission saddle point for ^{278}Ds. Upper: Spherical shell energies relevant to configuration mixing. Lower: Corresponding mixing weight, which is obtained from the geometrical nuclear shape. The vertical axis means a particle number, *Z*' or *N*', corresponding single-particle levels including effects of configuration mixings except for deformation. Particle numbers are also related to radius for each angle θ in spherical polar coordinates.

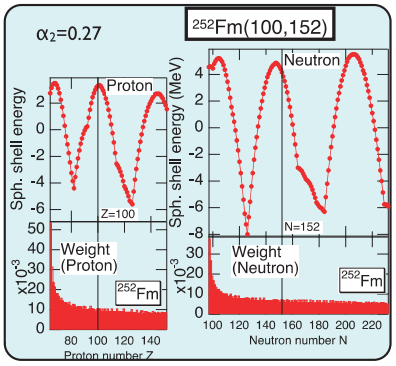

Fig. 3 Configuration mixing in the shape of fission saddle point for ^{252}Fm. See caption of Fig 2.

References

[1]H. Koura et al., Nucl. Phys., A674(2000)47-76.

[2]H. Koura et al., Prog. Theor. Phys., 113(2005)305-325.

5.3 Spin and mass distributions of compound nucleus in surrogate reaction

Y. Aritomo[1], S. Chiba[1] and K. Nishio[1]

Neutron-induced cross-section data of unstable nuclei are systematically required to design next-generation nuclear facilities such as high-burn-up fast breeder reactors or accelerator-driven systems for transmutation of nuclear wastes [1]. Such data are also important to understand origin of elements, namely, the s- and r-process nucleosynthesis. However, it is not usually possible to measure these cross sections directly by using neutrons owing to difficulty in preparing samples. To overcome the experimental limitations, indirect methods have to be developed, such as the surrogate nuclear reaction approach. In this method, (multi) nucleon transfer reactions with an experimentally accessible combination of projectile and target are employed to create the same compound nucleus as the desired neutron reaction, and decay branching ratios to specific channels, normally capture and/or fission, are determined. However, branching ratios are sensitive to the spin and parity of the compound state, while the spin-parity J^{π} distributions of populated nuclei are probably different for the neutron-induced and surrogate reactions. Therefore, validity of the surrogate method depends on how the difference of the spin-parity distributions is comprehended and compensated properly.

Recently, the surrogate ratio method (SRM) is discussed by Chiba and Iwamoto. It was found that SRM works to a certain accuracy if (1) there exist two surrogate reactions whose spin-parity distributions of decaying nuclei are equivalent, (2) difference of representative spin values between the neutron-induced and surrogate reactions is not much larger than 10ħ [2]. They form a set of sufficient conditions for the SRM to work. We need further investigation to verify that the above conditions are really satisfied in certain surrogate reactions. For that aim, we established a theoretical model based on the unified mode [3,4] to describe the whole process of the surrogate reactions, namely, nucleon transfer and decay of a populated compound nucleus [5]. The time-evolution of the system is described by a trajectory calculation on the time-dependent unified potential energy surface using the Langevin equation [6].

Using our theoretical model, we calculated the spin of compound nucleus in surrogate reactions. As the surrogate reaction, we considered the two neutron transfer reaction; $^{18}O+^{238}U \rightarrow {}^{16}O+^{240}U$ at an incident energy of $E_{c.m.}$ =133 MeV. The calculation results suggested the validity of the surrogate ratio method. In our model, the friction parameter has an uncertainty. We reported the spin distribution of compound nucleus for several sliding frictions [7]. Then, we investigate the sensitivity of the spin distribution to the several strengths of the radial friction in the two-body and one-body regions [6]. The main features of spin distributions do not change so much for the friction with several reduction factors. We conclude that the sliding friction has much effect on the spin distribution in this system, and the results for any frictions with the several reduction factors suggest the validity of the surrogate ratio method

[1] Japan Atomic Energy Agency (JAEA)

The fission fragment mass distribution (FFMD) from ^{240}U is shown in Fig.1. In this mass region, the FFMD shows typical asymmetric distribution for low J values, which is well reproduced by our calculation. Then, we put J = 10 and 20, and generated many Langevin trajectories and compared them with the J = 0 results. We can notice that the peak of the asymmetric mass division does not change, but the symmetric components are slightly enhanced when J becomes 10 and 20. It can be interpreted that when J becomes larger, the liquid-drop energy, which gives minimum at the symmetric division, increases, and the overall effect is to enhance the symmetric fission. If this is really the case, the FFMD data, which can be obtained in our forthcoming experiments, can be used to estimate the spin distributions populated in surrogate reactions. However, the spin-dependence of the FFMD pointed out here is not a phenomenon confirmed yet. Therefore we must place a special care on this result, although it may give a new insight into the understanding of the fission mechanism.

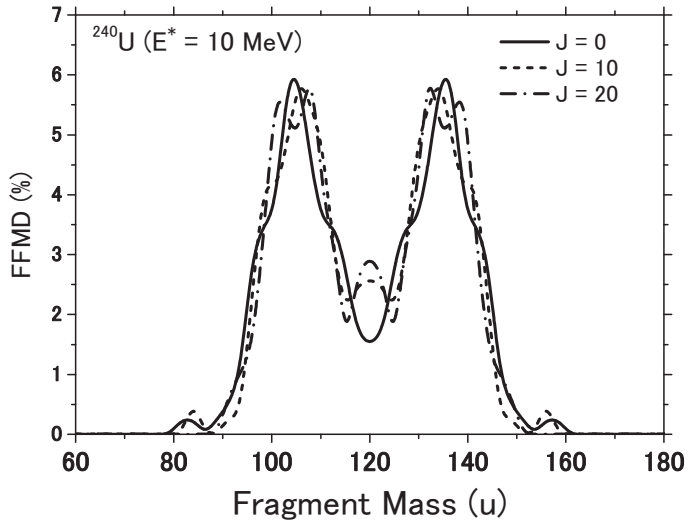

Fig. 1 Fission fragment mass distribution (FFMD) emitted from J=0, 10 and 20 states of ^{240}U at excitation energy of 10 MeV.

References

[1] International Atomic Energy Agency (Editor), Fission Product Yield Data for the Transmutation of Minor Actinide Nuclear Waste (IAEA, Vienna, 2008).

[2] S. Chiba and O. Iwamoto, Phys. Rev., C81(2010) 044604.

[3] V. Zagrebaev and W. Greiner, J. Phys., G31(2005)825.

[4] V. Zagrebaev and W. Greiner, J. Phys., G34(2007)1; J. Phys., G34(2007)2265; Phys. Rev. Lett., 101 (2008)122701; Phys. Rev., C78(2008)034610.

[5] Y. Aritomo, S. Chiba and K. Nishio, accepted for publication in Phys. Rev., C.

[6] Y. Aritomo, Phys. Rev., C80(2009)064604.

[7] Y. Aritomo, S. Chiba and K. Nishio, JAEA-Tokai Tandem Ann. Rep. 2009, JAEA-Review 2010-056 (2010) 75.

5.4 Analysis of various cross sections in deuteron induced reaction with CDCC and eikonal reaction theory

S. Hashimoto[1], M. Yahiro[2], K. Ogata[3], K. Minomo[2] and S. Chiba[1]

Deuteron induced reactions strongly interest not only nuclear physicists but also nuclear engineers, because available data of the nuclear reaction are required to plan new experimental facilities, e.g., the International Fusion Materials Irradiation Facility (IFMIF). In particular, inclusive (*d,xn*) reactions, which may become a high intensity neutron source in such an environment, are very important for the nuclear application. Recently, Ye *et al.* [1] showed that there are large contributions of not only elastic breakup processes but also incomplete fusion (proton stripping) processes in the case of Li targets. Unlike the former process described successfully by the continuum-discretized coupled-channels method (CDCC) [2], which has been developed and successfully used to analyze many breakup reactions with weakly-bound nuclei, the reaction mechanism of the latter process estimated by the Glauber model is still not sufficiently understood owing to the difficulty in describing an effect of the projectile breakup on the fusion reaction in the strong Coulomb field. The solution of this problem is required to analyze many valuable measurements on the reaction with unstable nuclei.

We analyzed deuteron induced reactions on from light and to heavy targets at 400 MeV with CDCC and eikonal reaction theory (ERT) [3]. The procedure [4] combined the two methods takes account of not only breakup but also proton- and neutron-stripping processes, and therefore can provide various cross sections accurately. The CDCC method gives reaction cross section $\sigma_{\rm R}$ and elastic breakup cross section $\sigma_{\rm EB}$, and the proton- and neutron stripping cross sections, $\sigma_{p:\rm STR}$ and $\sigma_{n:\rm STR}$, are obtained by the ERT with *S*-matrix elements calculated by CDCC. Using these cross sections, we can also derive the total, incomplete and complete fusion cross sections, $\sigma_{\rm TF}$, $\sigma_{\rm IF}$ and $\sigma_{\rm CF}$, as follows:

$$\sigma_{\rm TF} = \sigma_{\rm R} - \sigma_{\rm EB}, \quad \sigma_{\rm IF} = \sigma_{p:\rm STR} + \sigma_{n:\rm STR}, \quad \sigma_{\rm CF} = \sigma_{\rm TF} - \sigma_{\rm IF}$$

In Ref. [4], comparing some experimental data on reaction cross section and stripping cross section with theoretical results, we confirmed the validity of the procedure and optical potentials used in the calculation to be suitable. Then, we discussed the dependence of the cross sections on the target mass *A*, and found that the cross sections are presented by simple formulae with effective radii and widths describing the systematics. In Fig. 1, the A-dependence of $\sigma_{\rm R}$, $\sigma_{\rm TF}$, $\sigma_{\rm CF}$, $\sigma_{\rm IF}$ and $\sigma_{\rm EB}$ obtained with CDCC and ERT is shown by dots, and results by the formulae given as,

$$\sigma_{\rm R} = \pi R_{\rm EB}^2, \ \sigma_{\rm TF} = \pi R_{\rm TF}^2, \ \sigma_{\rm CF} = \pi R_{\rm CF}^2,$$

$$\sigma_{\rm IF} = 2\pi D_{p:\rm STR} R_{p:\rm STR} + 2\pi D_{n:\rm STR} R_{n:\rm STR}, \ \sigma_{\rm EB} = 2\pi D_{\rm EB} R_{\rm EB}$$

are also represented. The type of $\sigma_X = \pi R_X^2$ (X=EB, TF, CF) means the corresponding reaction takes place on a disk of radius R_X, and the another type of $\sigma_Y = 2\pi D_Y R_Y$ (Y=IF, *p*:STR, *n*:STR, EB) does the reaction

[1] Japan Atomic Energy Agency (JAEA)
[2] Kyushu University
[3] Research Center for Nuclear Physics (RCNP), Osaka University

occurs on a ring of radius R_Y with width D_Y. These effective radii and widths are parameterized by a function of $c_X + r_{0X}A^{1/3}$ except D_{EB}, and are determined from fitting for R_{EB} and R_{TF}. One can see the good agreement between the dots and lines, and it suggests each reaction is described by the simple picture. In particular, it is surprising that σ_{EB} including not only nuclear but also Coulomb breakup contributions is reproduced very well by using D_{EB}, which depends on also the charge of the target. Figure 2 shows effective radii, R_{EB}, R_{TF}, $R_{n:STR}$, $R_{p:STR}$ and R_{CF}. Division of the R-coordinate space by the various reactions is clearly found in the whole mass region, and we can distinguish the region where each reaction takes places regardless of the target mass.

In conclusion, we applied a new approach with a combination of CDCC and ERT to the deuteron induced reaction at an intermediate energy on various targets, and obtained the reaction, elastic breakup, proton- and neutron-stripping and complete fusion cross sections. The A-dependence of the cross sections can be described by simple formulae with two types of a disk and a ring. By introducing the effective radii and widths, we can deeply understand the reaction mechanism including the direct and fusion processes with composite particles, such as unstable nuclei. For future work, the same analysis for other projectiles or incident energies is interesting, and its result may play an important role in studying nuclear physics and its application.

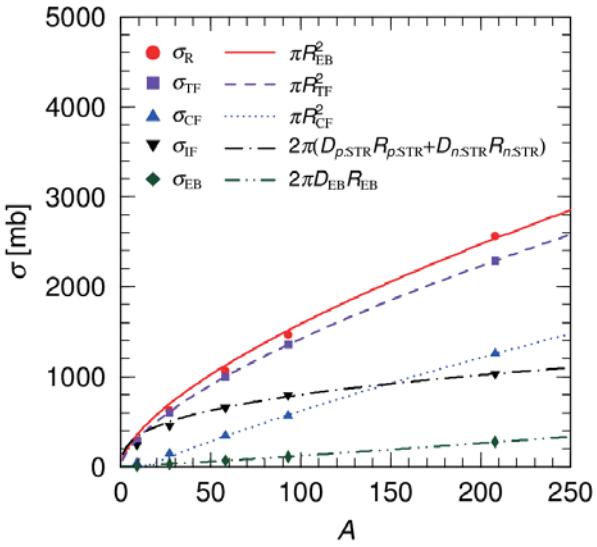

Fig. 1 A-dependence of reaction, total fusion, complete fusion, incomplete fusion and elastic breakup cross sections.

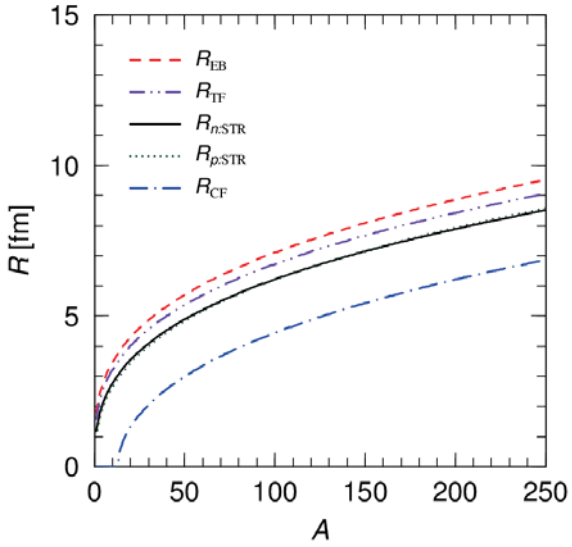

Fig. 2 A-dependence of effective radii. $R_{n:STR}$ and $R_{p:STR}$ are almost the same as each other.

References

[1] T. Ye, Y. Watanabe and K. Ogata, Phys. Rev., C80 (2009)014604.

[2] M. Kamimura et al., Prog. Theor. Phys. Suppl., 89 (1986)1.

[3] S. Hashimoto et al., Phys. Rev., C83(2011)054617.

[4] M. Yahiro, K. Ogata and K. Minomo, arXiv: 1103(2011)3976.

CHAPTER 6

Atomic Physics and Solid State Physics

6.1 Charge state distribution of carbon ions after penetration of C-foil targets
6.2 Electronic sputtering of CuO films by high-energy ions

This is a blank page.

6.1 Charge state distribution of carbon ions after penetration of C-foil targets

M. Imai[1], M. Sataka[2], H. Sugai[2], K. Kawatsura[3,4], K. Takahiro[5],
K. Komaki[6], K. Nishio[2] and H. Shibata[1]

Charge state is one of the most important aspects for ion interactions with matter, and affects various processes, such as electron capture, ionization, and excitation both of projectile and target electrons, as well as consequent phenomena such as energy deposition into the target, *i.e.*, stopping of projectiles. Projectile charge state and its evolution are therefore essential to the study of the penetration of swift ions in matter and the data of charge-state distributions for various collision systems after exiting solid targets have been supplied [1], although the charge-state distribution changes somewhat upon exiting the target foil. As has been presented in the previous annual reports [2] and in the 100,000-hour-operation-memorial workshop as well [3], we have measured the exit charge state distributions for penetrations of S^{6+} – S^{16+} ions through C-foil targets of 0.9 – 200 μg/cm^2 in thickness and performed calculations by ETACHA code [4] to succeed in reproducing the experimental results, although ETACHA has been designed for higher energy region (>10 MeV/u) [5]. Our data was so striking that stimulated another theoretical group to start reproducing them with matrix method [6]. In this report, results of our extensive measurements for carbon projectiles, which are essential to precise estimation of deposited energy for heavy-ion cancer therapy, between C^{2+} and C^{6+} are presented.

The experiments were performed at the LIR1–3 beam line of the 20UR Tandem Accelerator Facility. A beam of 2.0 MeV/u (24 MeV) C^{2+} ion was provided from the Tandem Accelerator within an energy accuracy of 0.1%. A post-stripper C-foil of ~20 μg/cm^2, energy losses through which were estimated to be at most 0.7% by our separate measurement of cusp electron energies, was used to produce higher charge states. The C^{q+} (q = 2−6) ion beam was directed into a self-support carbon foil targets of 0.9 − 10 and 54 − 100 μg/cm^2 in thickness for non-equilibrium and equilibrium charge distribution measurements, respectively. The charge states after foil penetration were measured using the heavy ion magnetic spectrometer ENMA and a position-sensitive gas chamber detector. The vacuum condition inside the collision chamber and the spectrometer were maintained below 10^{-4} and 10^{-6} Pa, respectively, to practically eliminate background charge-exchange collisions with residual gas, which was confirmed by measurements without a target foil.

Values of mean charge state $\bar{q} = \sum_q qF(q)$ and charge distribution width $d = \left[\sum_q (q-\bar{q})^2 F(q)\right]^{1/2}$, where $F(q)$ denotes the fraction for charge state q (q = 3−6), are plotted in Fig. 1. It can be seen that the mean charge states make beelines for the equilibrium value when the target thickness grows until 10

[1] Kyoto University
[2] Japan Atomic Energy Agency (JAEA)
[3] Kansai Gaidai University
[4] Theoretical Radiation Research Laboratory
[5] Kyoto Institute of Technology
[6] RIKEN

μg/cm^2, whereas the distribution width for projectile shows maximum around 3 μg/cm^2. The equilibrium charge state and its distribution width have been derived to be 5.58 and 0.57, respectively.

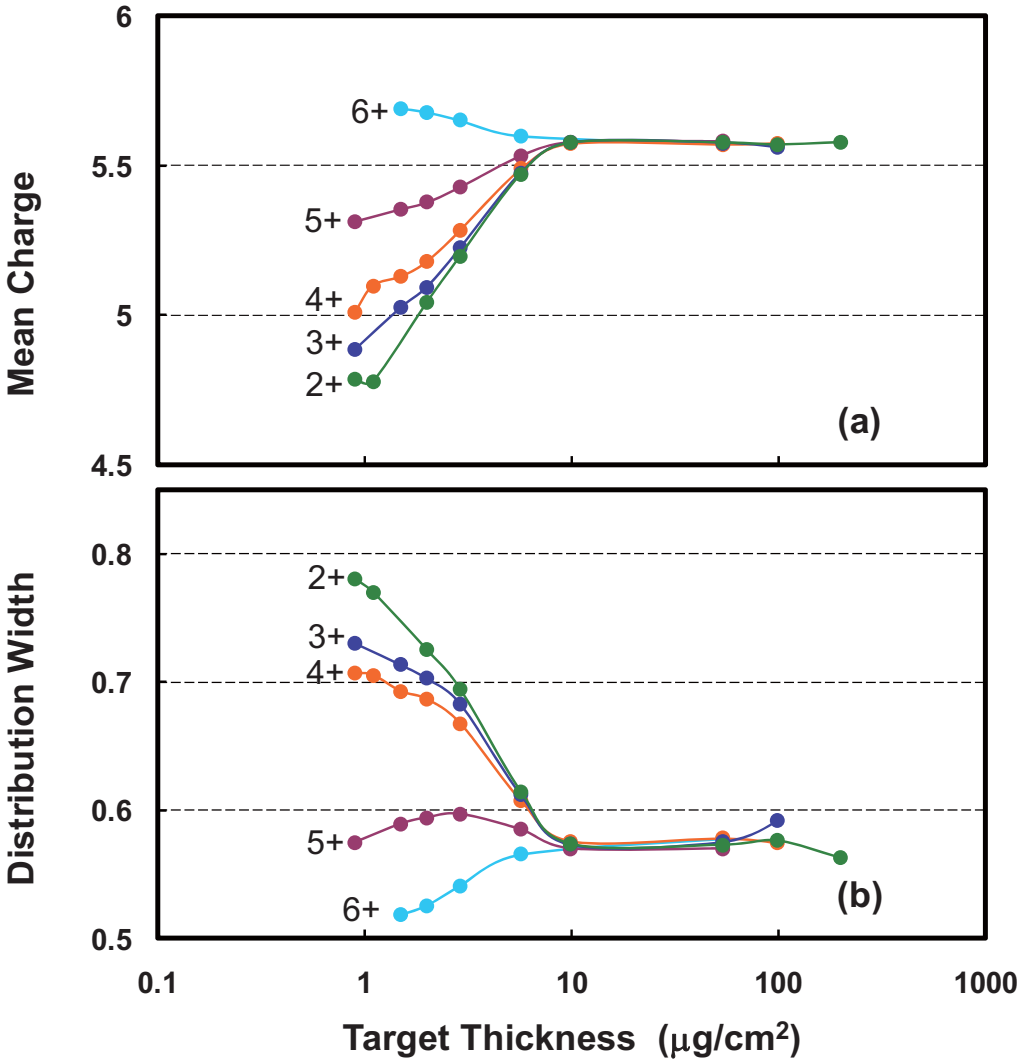

Fig. 1 (a) Mean charge state and (b) distribution width measured for 2.0 MeV/u C^{2+} − C^{6+} ion incidences after penetration through C-foil targets.

References

[1] A. B. Wittkower and H. D. Betz, At. Data Nucl. Data Tables 5 (1973) 113–166; K. Shima *et al.*, *ibid.* 51 (1992) 173–241; K. Shima et al., Nucl. Instrum. Methods Phys. Res., B33 (1988) 212–215.

[2] M. Imai et al., JAEA-Review 2007-046 (2008) 87–88; 2008-054 (2008) 89–90; 2009-036(2009) 91–92; 2010-056 (2010) 89–90.

[3] M. Imai, JAEA-Review 2009-006 (2009) 168–180.

[4] J. P. Rozet et al., J. Phys. B22 (1989) 33–48; Nucl. Instrum. Methods Phys. Res., B107 (1996) 67–70.

[5] M. Imai et al., Nucl. Instrum. Methods Phys. Res., B230 (2005) 63–67; *ibid.* B256 (2007) 11–15; *ibid.* B267 (2009) 2675–2679.

[6] O. Osmani and P. Sigmund, Nucl. Instrum. Methods Phys. Res., B269 (2011) 813–816.

6.2 Electronic sputtering of CuO films by high-energy ions

N. Matsunami[1], M. Sataka[2], S. Okayasu[2] and H. Kakiuchida[3]

We have studied the electronic sputtering, modifications of the electronic and atomic structures of cuprite (Cu_2O) films under high-energy ion impact [1]. It is of interest to extend such studies to cupper oxide (CuO) for comparison with the Cu_2O results and further understanding of the electronic excitation effects.

CuO films were prepared on MgO at 700 ºC, using a sputter-deposition method with a Cu target in Ar and O_2 gas. X-ray diffraction (XRD) shows that the films are monoclinic with (111) orientation and the planar spacing is 0.2339 nm, which is larger by 0.7% than the bulk value, 0.2323 nm [2]. By means of Rutherford backscattering spectroscopy (RBS) of 1.8 MeV He^+, using the stopping power [3] and the density of $4.85x10^{22}$ Cu cm^{-3}, the film thickness is obtained to be ~100 nm with nearly stoichiometric composition.

The carbon (C)-foil collector method [1] was applied to analyze Cu sputtered from CuO films. Fig. 1 shows that the amount of Cu in the C-foil is proportional to the ion fluence, from which the sputtering yield of Cu per ion is evaluated using the C-foil collection efficiency of Cu (0.3) [1] and by multiplying it by 2. Here, stoichiometric sputtering is assumed, since the composition remains unchanged after the ion impact. Firstly, the sputtering yields are much (10^2-10^3) larger than those of the elastic collisions (Y_C) which are calculated assuming the linear dependence of Y_C on the nuclear stopping power with the preliminary sputtering yield of 0.88 by 100 keV Ne ion impact (Table 1). This confirms that the electronic excitations play a dominant role in the sputtering. The electronic sputtering yield Y is well fitted by $Y=4.0S_e^{1.08}$, S_e being the electronic stopping power (keV/nm). This is exceptionally close to linear dependence on S_e, in contrast to the super-linear dependence for other oxides and nitrides [4-6], e.g., $Y=0.006\ S_e^{2.78}$ for Cu_2O.

It appears that the (111) diffraction intensity is reduced to half at the fluence of $2.5x10^{12}$ cm^{-2} and one-fourth at ~$10x10^{12}$ cm^{-2} for both 100 MeV Xe and 90 MeV Ni ion impact. This indicates disordering of the atomic structure and the disordering is exceptionally independent of the ion species or S_e, in contrast to the Cu_2O result that the disordering is more pronounced for 100 MeV Xe ion [1]. It also appears that the (111) planar spacing is reduced by ~0.1 % at $2.5x10^{12}$ cm^{-2} for both 100 MeV Xe and 90 MeV Ni ions. The lattice compaction of CuO is much smaller than that in Cu_2O [1]. No appreciable change in the optical absorption spectra and the bandgap is observed, as shown in Fig. 2, except for the absorption at 0.25 μm due to color center generation of MgO substrate by the ion impact. For unirradiated films (inset in Fig. 2), the direct bandgap [7] is determined to be 2.1(±0.1) eV in agreement with 2.12 eV in [8]. The bandgap of CuO is smaller than that of Cu_2O (2.54 eV). The electronic sputtering yield of CuO is larger than that of Cu_2O, in disagreement with the suggested bandgap dependence ($0.1Eg^4$ at S_e=15 keV/nm) [4] and is much larger than the estimation from the suggested formula. These results imply that for small bandgap, the number of electron hole pairs, which is inversely proportional to the bandgap, becomes more important.

[1] Division of Energy Science, EcoTopia Science Institute, Nagoya University
[2] Japan Atomic Energy Agency (JAEA)
[3] National Institute of Advanced Industrial Science and Technology (AIST)

Table 1 Electronic (S_e) and nuclear (S_n) stopping powers in CuO (keV/nm) [3], sputtering yield Y and the sputtering yield Y_C of the elastic collisions.

Ions	S_e	S_n	Y	Y_C
198 MeV Xe	31.2	0.126	173	0.40
99 MeV Xe	24.0	0.221	120	0.71
89 MeV Ni	17.1	0.0345	80	0.11
60 MeV Ar	9.64	0.0154	48.3	0.050
100 keV Ne	0.334	0.276	0.88	

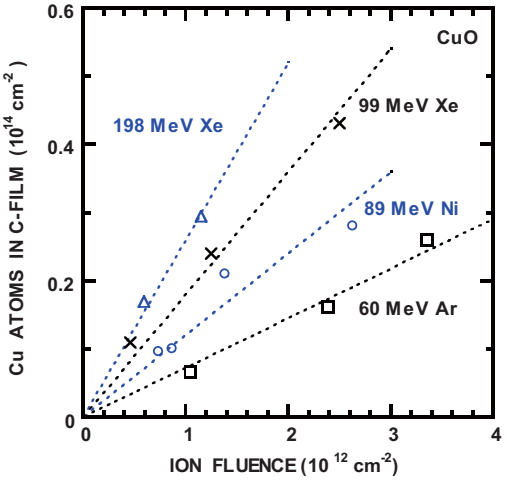

Fig. 1 Cu in carbon-foil collector vs ion fluence for 198 MeV Xe (△), 99 MeV Xe (×), 89 MeV Ni (○) and 60 MeV Ar (□) ion impacts on CuO films.

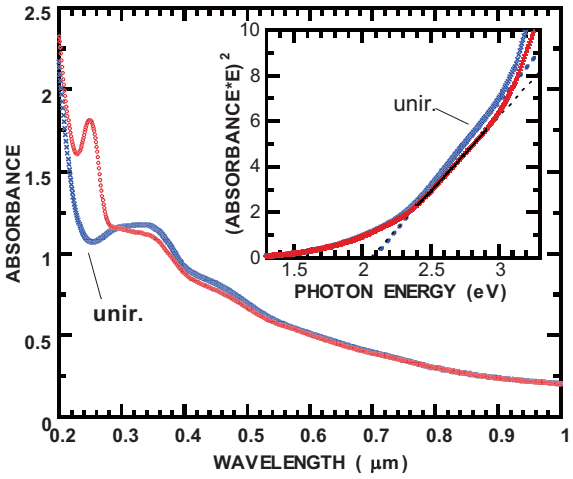

Fig. 2 Optical absorption spectra of CuO before and irradiated with 100 MeV Xe ion at 1.25×10^{12} cm^{-2}. Inset shows square of absorbance times photon energy E vs E, illustrating the bandgap determination.

References

[1] N. Matsunami et al., Nucl. Instrum. Methods, B266(2008)2986 and JAEA Tandem Report 2008.
[2] JCPDS no. 450937.
[3] J.F. Ziegler, J.P. Biersack and U. Littmark, The Stopping and Range of Ions in Solids, Pergamon Press, New York (1985).
[4] N. Matsunami et al., Nucl. Instrm. Methods B256(2007)333.
[5] N. Matsunami et al., Nucl. Instrum. Methods, B267(2009)2653.
[6] N. Matsunami et al., Nucl. Instrum. Methods, B268(2010)3167.
[7] W.Y. Ching, Y.N. Xu, K.W. Wong, Phys. Rev., B40(1989)7684.
[8] A. Chen et al., Thin Solid Films, 517(2009)4277.

CHAPTER 7

Radiation Effects in Materials

7.1 Radiation damage of crystal structure in UO_2 irradiated with high-energy heavy ions
7.2 Study on effects of energetic ion irradiation in Gd_2O_3-doped CeO_2 by means of synchrotron radiation X-ray spectroscopy
7.3 Change in magnetic properties of CeO_2 by swift heavy ion irradiation
7.4 Shape and property control of Zn and ZnO nanoparticles by swift heavy ions
7.5 Radiation effects for film formation and nano-structural changes of iron disilicide thin film
7.6 Formation of metal microstructures induced by heavy ion irradiation in Ag-zeolite
7.7 Surface amorphization in single crystalline Al_2O_3

This is a blank page.

7.1 Radiation damage of crystal structure in UO_2 irradiated with high-energy heavy ions

N. Ishikawa[1], T. Sonoda[2], T. Sawabe[2] and A. Iwase[3]

Uranium dioxide (UO_2) fuels in light water reactors are subjected to various high-energy particles. Not only neutrons but also high-energy fission fragments play an important role in radiation damage process. Since fission fragments have high kinetic energy of about 70~100-MeV, they create radiation damages in UO_2 oxide fuels. One of the intriguing characteristics of the radiation damages due to high-energy ion irradiation in UO_2 is the formation of continuous ion tracks along the ion-paths [1]. The present study aims at characterizing disordering of crystal structure in ion-irradiated UO_2 at high fluence range where ion-tracks overlap heavily. In the present study, polycrystalline UO_2 samples are irradiated with high-energy Xe ions up to 10^{15} ions/cm^2 and the damage is characterized by X-ray diffraction (XRD) technique. The CuKα_1 X-ray is useful to detect crystal structure change of irradiation-induced damaged region, because the diffraction of the X-ray is taken place only in a shallow region where the irradiation-induced damage is accumulated. The depth profile of X-ray penetration is demonstrated in Fig.1, together with the depth profile of the electronic stopping power of 210 MeV Xe ion. In the figure, the incident angle of Cu Kα_1 X-ray is assumed as θ=44°, because in the present study the change of (422) peak which appear at around 2θ=87.2° is analyzed. The figure clearly shows that Cu Kα_1 X-ray is penetrated only in the shallow region where the electronic stopping power is relatively high.

Figure 2 shows the evolution of (422) diffraction peak for UO_2 before and after the irradiation with 210 MeV Xe ions. The peak at the lower angle side corresponds to the reflection of Cu Kα_1 X-rays, and that at the higher angle side corresponds to that of Cu Kα_2 X-rays. As a result of least-squares fitting and decomvolution using formulation of the pseudo-Voigt function [2], the observed profile can be separated into 2 peaks even for high fluence samples. It is found that both constituting peaks gradually shift toward lower angle side with increasing fluence, indicating that the lattice parameter increases by the irradiation-induced lattice defects. Figure3(a) shows that the lattice parameter estimated from the shift of peak angle monotonically increases as a function of fluence. Figure 3(b) shows that the full width at half maximum (FWHM) increases with increasing fluence. Figure 3(c) shows that the intensity of the peak decreases with increasing fluence. The present results show that the radiation damage in the crystallographic lattice of UO_2 is detected at relatively low fluence of 10^{12} ions/cm^2, and it accumulates up to high fluence of 10^{15} ions/cm^2. The detection of the damage at relatively low fluence of 10^{12} ions/cm^2 can be explained by the introduction of nm-sized ion-tracks. The occupancy of ion-tracks in the specimen affects the damage evolution.

---

[1] Japan Atomic Energy Agency (JAEA)
[2] Central Research Institute of Electric Power Industry (CRIEPI)
[3] Osaka Prefecture University

In order to estimate the occupancy of accumulated ion-tracks (δ) as a function of fluence, it is important to taken into account the overlapping of ion-tracks. In the present analysis, it is assumed that fluence dependence of the occupancy follows the exponential function expressed by the Poisson law as expressed by $\delta=1-\exp(-A\Phi)$, where A is the cross section of the ion-track and fluence is Φ. The occupancy at 10^{12} ions/cm^2 assuming the typical diameter of 4.9 nm[3] is about 20% of the sample volume. This explains the present result that the decrease in XRD intensity and increase in peak width is detected at relatively low fluence of 10^{12} ions/cm^2.

Part of the present study is the result of "Research of highly accurate evaluation of radiation damage in advanced nuclear reactor fuel ceramics" entrusted to "Japan Atomic Energy Agency" by the Ministry of Education, Culture, Sports, Science and Technology of Japan (MEXT).

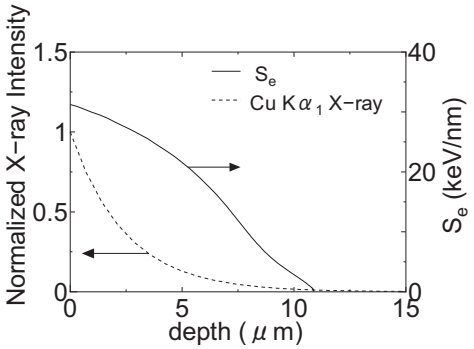

Fig. 1 Depth profile of normalized intensity of CuKα_1 X-ray (8.04 keV) with the incidence angle of 44 degree (dotted line) for UO_2 sample. Depth profile of electronic stopping power, S_e, (solid line) is also shown for comparison.

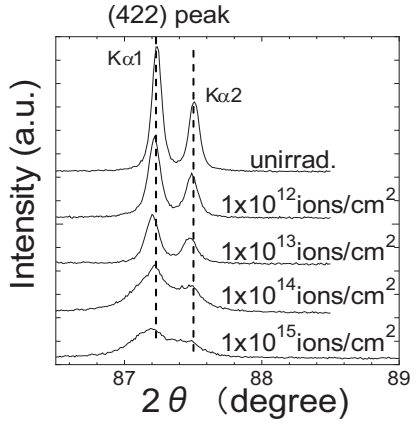

Fig. 2 Evolution of X-ray diffraction peaks assigned for (422) reflection of UO_2 irradiated with 210 MeV Xe ions. The original positions of peaks for unirradiated sample are indicated as dotted lines for guides for the eyes.

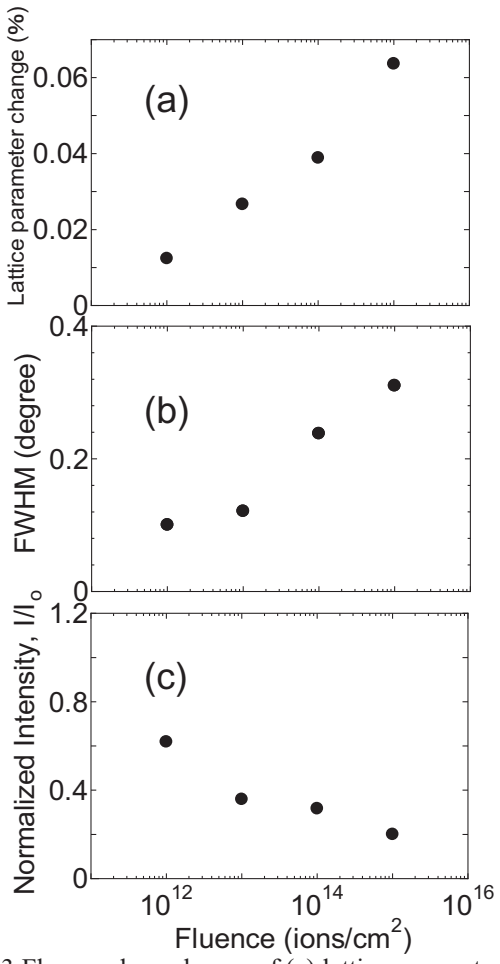

Fig. 3 Fluence dependences of (a) lattice parameter change, (b) full width at half maximum (FWHM) and (c) peak intensity for (422) peak of UO_2 irradiated with 210 MeV Xe ions.

References

[1] Hj. Matzke, P.G. Lucuta and T. Wiss, Nucl. Instrum. Methods, B166-167(2000)920.

[2] H. Toraya, J. Appl. Cryst., 23(1990)485.

[3] T. Sonoda et al., Nucl. Instrum. Methods, B250 (2006)254.

7.2 Study on effects of energetic ion irradiation in Gd_2O_3-doped CeO_2 by means of synchrotron radiation X-ray spectroscopy

Y.Tahara[1], K.Shimizu[1], N.Ishikawa[2], Y.Okamoto[2], F. Hori[1], T. Matsui[1] and A.Iwase[1]

In the present light-water reactors, to control the initial reactivity of enriched UO_2 fuels, Gd_2O_3, which has the high neutron-absorption cross section, has been doped into UO_2. As Gd_2O_3-doped UO_2 fuels are exposed to the irradiation with high energy (~100 MeV) fission products (FPs) during the burning, it is important to study the effects of the FPs irradiation on the Gd_2O_3-doped UO_2.

To study the effects of Gd_2O_3-doping and the irradiation with the FPs in the nuclear fuels (UO_2), Gd_2O_3-doped CeO_2 pellets, which are simulation materials of UO_2, were irradiated with 200 MeV Xe^{14+} ions. During recent years CeO_2 has been used as a simulation material for UO_2 because it has the same fluorite structure as that of UO_2 and its physical properties are similar to those of UO_2 [2]. Effects of Gd_2O_3-doping and the ion irradiation were estimated by using Extended X-ray Fine Structure (EXAFS) measurement.

Figure 1 shows the effects of 200 MeV Xe ion irradiation on Fourier transforms of EXAFS spectra (EXAFS-FT spectra) near Ce L3 edge. The first peak corresponds to the first coordination of the Ce atoms (O atoms) and the second peak corresponds to the second coordination of the Ce atoms (Ce(Gd) atoms). In the case of pure CeO_2 and the specimens doped with 1 mol% and 5 mol% Gd_2O_3, the intensity of first and second peaks decreases by the ion irradiation. In the case of 10 mol%-doped specimen, however, the effect of ion irradiation on EXAFS spectrum is much smaller than the other cases. To analyze the EXAFS spectra in details, we compared the experimental EXAFS-FT spectra and the spectra calculated using the FEFF computer code [2]. By using this computer code, we can determine the value of interatomic distances and Debye-Waller factors. The interatomic distances of Ce-O and Ce-Ce increase by the irradiation and the effect of the ion irradiation on the atomic distances is more pronounced for higher amounts of dopant. The Debye-Waller factors for Ce-O and Ce-Ce pairs increase with increasing the amount of Gd_2O_3 dopant. These results suggest that the lattice binding energy is weakened by Gd_2O_3-doping. The present result reveals that the EXAFS measurement is very useful for the detailed study of the effects of dopant and irradiation on nuclear technology related oxides such as UO_2 fuels and their simulation material CeO_2.

[1] Osaka Prefecture University
[2] Japan Atomic Energy Agency (JAEA)

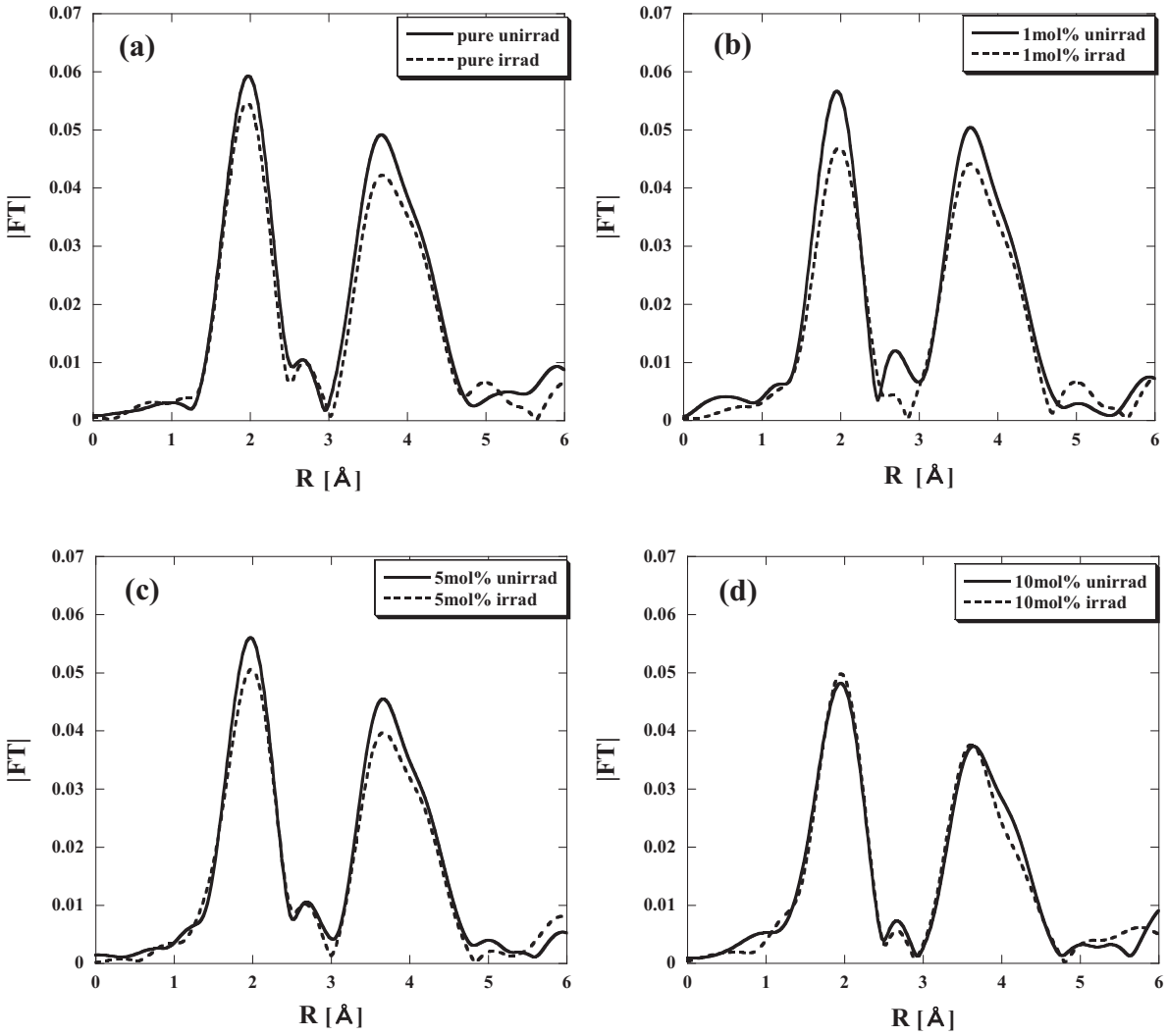

Fig. 1 EXAFS-FT spectra near Ce L3 edge before and after irradiation for (a) pure, (b) 1 mol%-doped, (c) 5 mol%-doped, (d) 10 mol%-doped specimens.

References

[1] M. Kinoshita et al., Nucl. Instrum. Methods, B267 (2009) 960.

[2] S.I. Zabinsky et al., Phys. Rev., B52 (1995) 2995.

7.3 Change in magnetic properties of CeO_2 by swift heavy ion irradiation

K. Shimizu[1], S. Kosugi[1] , Y. Tahara[1], K. Yasunaga[3], N. Ishikawa[2] , Y. Okamoto [3] ,
Y. Baba [3], N. Hirao [3], F. Hori [1], T. Matsui [1] and A. Iwase[1]

Recently, ferromagnetism has been reported in several defective oxides such as HfO_2 thin films[1], ion-irradiated TiO_2[2], and CaO[3] and SrO[4] including nonmagnetic impurities. These reports take it as given that ferromagnetism is induced by lattice defect. In the past, our laboratory showed that the 200 MeV Xe ion irradiation for CeO_2 effectively displaced oxygen atoms and produced their Frenkel pairs through high density electronic excitation[5].

In this study, specimens of CeO_2 pellet with dimension of about 6 mm in diameter and 0.3 mm thick were irradiated room temperature with 200 MeV Xe ions by using a high energy ion accelerator at JAEA-Tokai. After the irradiation, magnetization was measured by using the superconducting quantum interference device (SQUID). The scanning range of the applied magnetic field was from -10000 Oe to 10000 Oe and the measurement temperature was 20 K. The X-ray diffraction (XRD) method and the extended X-ray absorption fine structure (EXAFS) measurement were used to reserch change of lattice structure with difference of magnetism .

Figure 1 shows that the magnetization versus magnetic field curve for CeO_2 specimens irradiated with 200 MeV Xe ions. The value of saturation magnetization, M_s, systematically changes as a function of ion-fluence. The value of M_s increases with increasing the ion-fluence reaches a maximum value at about $2x10^{13}/cm^2$, and then decreases. Figure 2 shows that the change in XRD spectra around (331) peak of unirradiated and irradiated specimens for various ion-fluence. The peak is sifted lower angle on unirradiated samples by irradiation, which means that the lattice constant increases with increasing the ion ion-fluence.

Figure 3 shows that the change in the Fourier transformations of Ce L3-edge EXAFS spectra. When paying attention to the effects of ion irradiation, the intensity of the first and second neighboring peaks decrease with increasing the ion irradiation. It means that the structure around Ce atoms are changed locally by irradiation. The relationship between the irradiation-induced disordering and change in magnetic state still remains uncertain.

[1] Osaka Prefecture University
[2] Japan Atomic Energy Agency (JAEA)
[3] Kyusyu University

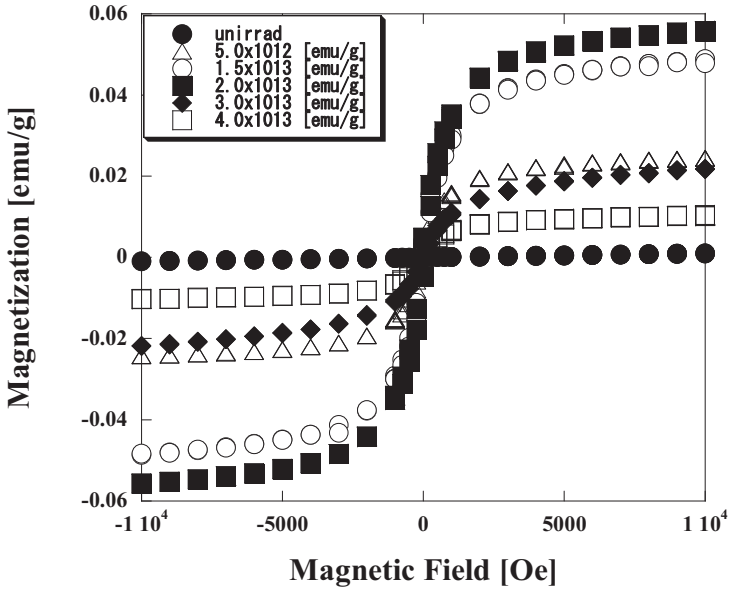

Fig. 1 Irradiation induced magnetic moment at 320K as a function of applied magnetic field for pure CeO_2 irradiated with 200MeV Xe.

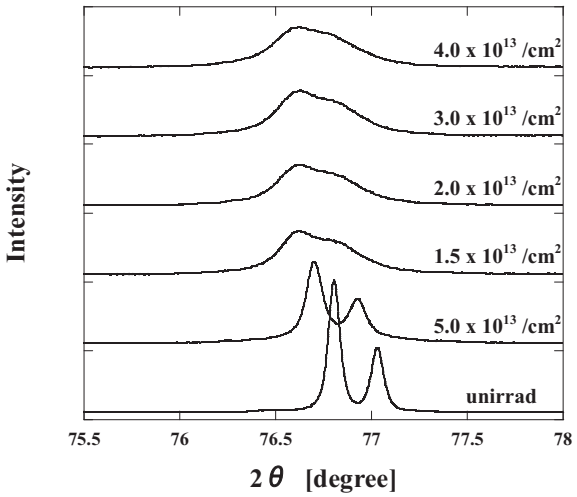

Fig. 2 XRD spectra around (331) of CeO_2 for various ion-fluences.

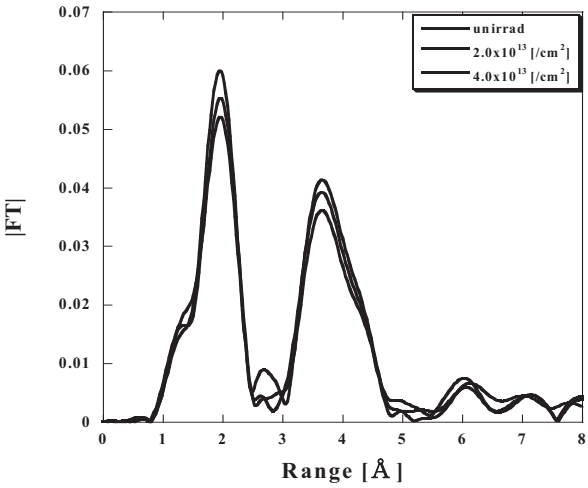

Fig. 3 Fourier transform of Ce L3-edge EXAFS spectra for CeO_2 with ion irradiation.

[1] J.M.D. Cocy et al., Phys. Rev., B72(2005)024450.
[2] S. Zhou et al, Phys. Rev., B79(2009)113201.
[3] K. Kenmochi et al., Jpn. J. Appl. Phys., 43(2004)L934.
[4] K. Kenmochi et al. J. Phys. Soc. Jpn., 73(2004)2952.
[5] A. Iwase at al., Nucl. Instrum. Methods Phys. Res., B267(2009)969.

7.4 Shape and property control of Zn and ZnO nanoparticles by swift heavy ions

H. Amekura[1], N. Ishikawa[2] and N. Okubo[2]

When metal nanoparticles (NPs) embedded in silica glass (SiO_2) are irradiated by swift heavy ions (SHI), elongation of the NPs, i.e., the transformation from spheres to rods along the ion beam direction, is induced. Distinguishable elongation requires irradiation with the fluence of ~1×10^{14} ions/cm^2 or higher, where one NP is subjected to impacts of ~100 SHIs or more. It is an important issue to understand whether the multiple collisions with SHIs are essential for the elongation or simply the elongation induced by a single impact is so small that high fluence is necessary. However, up to the present, the most of past works evaluated the elongation using transmission electron microscopy (TEM). In the annual report of last year [1], we have shown that the optical transmission spectroscopy with linearly-polarized light is a very sensitive method to detect the elongation of metal NPs. In this year the method was applied to evaluate the elongation at low fluence down to 1.0×10^{11} ions/cm^2 [2].

Zn NPs were formed by implantation of Zn ions of 60 keV to silica glass up to a fluence of 1.0×10^{17} Zn^+/cm^2. No post-implantation annealing was carried out. Then the samples were irradiated by the SHI of 200 MeV Xe^{14+} from the tandem accelerator at JAEA-Tokai, with an incident angle of 45 deg from the sample surface. The SHI fluence was varied from 1.0×10^{11} to 2.0×10^{12} ions/cm^2.

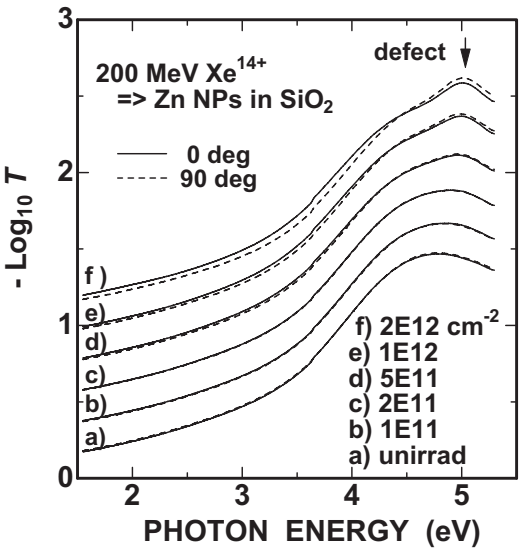

Fig. 1. Optical density spectra of Zn NPs in silica irradiated with 200 MeV Xe^{14+} ions at different fluences. Linearly polarized light with the polarization of 0 and 90 deg was used, which correspond parallel and perpendicular to the elongation direction of the NPs, respectively.

Optical transmission spectroscopy with linearly-polarized light was conducted in the wavelength region of 215 – 800 nm at room temperature. The results are shown in Fig. 1, in the form of the optical density - $\log_{10} T$, where T denotes the transmittance. The polarization angle of 0 deg corresponded to the direction of the major axes of elongated NPs. In unirradiated state, the spectrum of the 0 deg polarization coincided with that of the 90 deg polarization, indicating spherical shapes of NPs. With increasing the SHI fluence, the difference between the spectra of the 0 and 90 deg polarizations increased, indicating the progress of the elongation of

[1] National Institute for Materials Science (NIMS)
[2] Japan Atomic Energy Agency (JAEA)

the NPs. It should be noted that a peak appeared at 5 eV with increasing the fluence. The peak is ascribed to radiation damage of silica matrix.

The difference of the optical densities between the 0 and 90 deg polarization at the photon energy of 3.8 eV was plotted in Fig. 2 with the fluence. All the data points were well fitted by a linear relationship. However, the observed optical-density difference was very small in the unirradiated state but not zero. This was due to experimental uncertainty. From repeated measurements, we determined the experimental uncertainty of ~0.01 for the difference of the optical density with a certain safety margin. Consequently, the result shown in Fig. 2 is interpreted as that the elongation of Zn NPs was observed down to 5.0×10^{11} ions/cm^2. While very small anisotropic signal was observed at 2.0×10^{11} ions/cm^2, the same magnitude of signal can be observed even unirradiated samples because of experimental uncertainty.

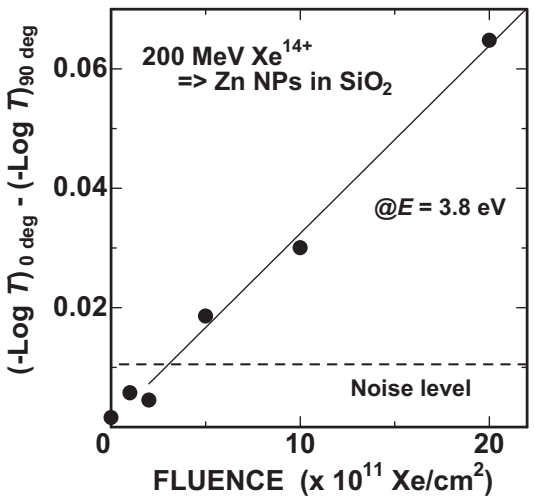

Fig. 2. Differences of optical densities at the photon energy of 3.8 eV between the polarization of 0 deg and that of 90 deg are plotted against the fluence. A horizontal broken line indicates experimental uncertainty.

Using the small angle X-ray scattering (SAXS), Kluth et al. [3] determined the mean radius of the ion tracks in amorphous silica irradiated by Xe and Au as the function of the electronic energy loss. According to their results, the radius of our case (200 MeV Xe) corresponds to r ~4 nm. The fluence $\Phi \sim 5 \times 10^{11}$ ions/cm^2, which is the lowest one that the elongation of NPs was observed, corresponds to the surface coverage ratio (CR) by ion tracks of $\pi r^2 \Phi \sim 0.25$. Thus, 25% of the surface of the sample was covered by ion tracks when superposition of the tracks is negligible.

To elucidate the situation under the condition of CR ~ 0.25, a Monte Carlo simulation of track coverage and overlaps between ion-tracks in a sample including NPs was conducted. The details were shown in Ref [2]. At CR ~ 0.25, 75% of NPs were hit by ion-tracks once or more, and 40% were hit by the tracks more than once. However, overlaps of the tracks occur in only 6% of NPs, i.e., negligible. Consequently, the track overlap does not play an important role in the elongation of Zn NPs in silica.

References

[1] H. Amekura, et al., JAEA-Review, 2010-056, 111-112.
[2] H. Amekura, et al. Phy. Rev., B83 (2011) 205401 (10 pages).
[3] P. Kluth et al. Phys. Rev. Lett., 101(2008) 175503 (4 pages).

7.5 Radiation effects for film formation and nano-structural changes of iron disilicide thin film

M. Sasase[1] and S. Okayasu[2]

Ion irradiation effects on the synthesis and modification of iron disilicide films have been investigated by cross-sectional observation of transmission electron microscope (TEM) in order to fabricate the films, which have better quality or unique properties. It has been observed that the pre-treatment effect of the substrate surface by several keV Ne^{+} irradiation affect the crystal structure of the films and interface. The films which have high orientation and smooth interface with the substrate can be obtained by optimizing the conditions of ion irradiation [1, 2]. We also attempted to perform nano-scale structure change by the high-energy heavy-ion irradiation.

The specimens used in this study were β-$FeSi_2$ films synthesis with the ion beam sputter deposition method by depositing Fe on Si(100) substrate at 973 K after sputter etching treatment. The specimens were irradiated by 95 MeV Ni^{9+} and 240 MeV Au^{24+} ions at room temperature with a fluence of 1.0 x 10^{12} ions/cm^2 using Tandem accelerator at JAEA. Cross sectional observations were performed with β-$FeSi_2$/Si(100) by using a transmission electron microscope (TEM, JEOL JEM-3100F) with a field emission gun operated at 300 keV

[synthesis]: On the basis of our previous reports[1], it has been clarified that the surface treatment of the Si substrate greatly affects the crystal structure of the films. Among several procedures of surface treatment, sputter etching (SE) of the substrate by several keV Ne^{+} with sequential annealing is fairly effective to obtain highly oriented films with epitaxial relationship of β-$FeSi_2$(100) //Si(100) [3]. Sputter etching effect of the substrate is investigated by the cross sectional TEM observation in order to observe nano-structural changes of deposited film and film/substrate interface as a function of Ne^{+} energy and fluence. As the result, the observed TEM images show that the SE at 1 keV (3 x 10^{20} ions/m^2) provides uniform films with few defects and smooth interface (Fig. 1). Better conditions of the SE for the silicidation and uniform film formation will be discussed from the results of the

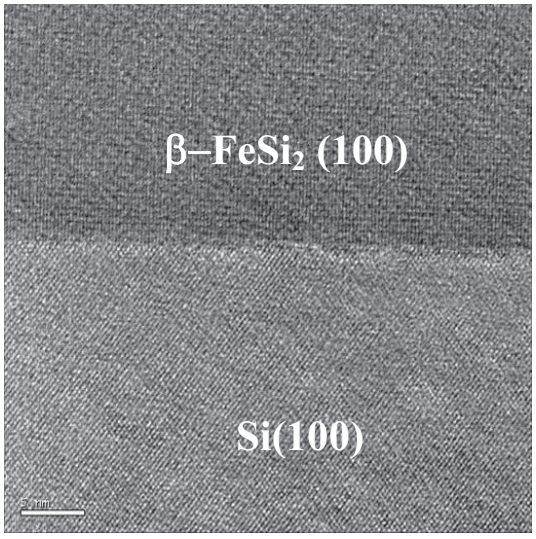

Fig. 1 Cross sectional TEM images of β-$FeSi_2$ (100) // Si(100).

[1] The Wakasa-wan Energy Research Center (WERC)
[2] Japan Atomic Energy Agency (JAEA)

nanostructure changes more precisely in the near future.

[modification]: When the high-energy heavy ions are irradiated into materials, most of their energies are dissipated through an electronic excitation [4]. This leads to strong localization of the dissipated energy along the projectile path. The density of energy deposition is high enough, compared with bond or displacement energy of the target materials, structural changes take place such as amorphization and phase transformation. We attempted to perform nano-scale structure change by the high-energy heavy-ion irradiation. No significant changes were observed in TEM images by 95 MeV Ni^{9+} irradiation. On the other hand, contrast changes corresponded to defects, induced by ion irradiation were observed from TEM images at 240 MeV Au^{24+} (Fig. 2). These defects have an average diameter of 8 nm as a shape of column, which is amorphous. The columnar defects were formed by the thermal spike effect due to the energy dissipation through electronic excitation. Because we clarified that the diameter of columnar defects increased with electronic stopping power (S_e) in the higher energy region [5].

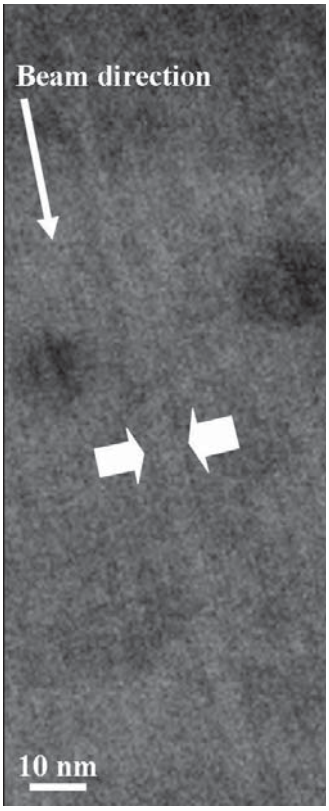

Fig. 2 Columnar defects introduced with 240 MeV Au^{24+} in β-$FeSi_2$ thin films.

We attempted to induce structural changes in nanoscale range by swift heavy ion. Although no phase transition could be confirmed in the β-$FeSi_2$ films, our results showed the structural changes were produced in nano-region by swift heavy ion.

References

[1] M. Haraguchi and M. Sasase et al., Nucl. Instrum. Methods Phys. Res., B206 (2003) 313.
[2] M. Sasase et al., J. Appl. Phys., 45(2006)4929.
[3] M. Sasase et al., Nucl. Instrum. Methods Phys. Res., B257 (2007) 186.
[4] M. Toulemonde and F. Studer, Nucl. Instrum. Methods Phys. Res., B91(1994) 108.
[5] M. Sasase et al., Nucl. Instrum. Methods Phys. Res., 2011 in press.

7.6 Formation of metal microstructures induced by heavy ion irradiation in Ag-zeolite

Y. Sasaki[1] and S. Okayasu[2]

When zeolites containing silver ions (Ag-zeolites) are irradiated with a high-energy electron beam of 200 keV or higher in a transmission electron microscope (TEM), the structure eventually becomes amorphous. We have found that ordered clusters of Ag atoms form in the amorphous regions during irradiation [1] shown in Fig.1. This may be because the breakdown in structure removes the electrostatic attraction binding Ag^+ ions to Al sites in the zeolite framework.

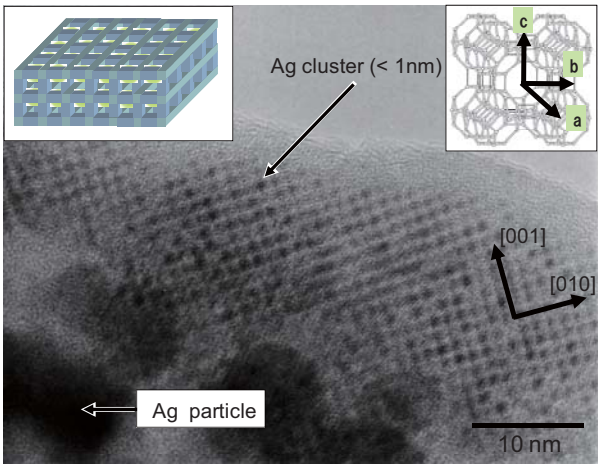

Fig. 1 (main panel) A photo of a cross-section TEM image of e-irradiated Ag-LTA zeoilte. Ag–metal clusters are found in the cages of LTA-zeolite.
(upper left) A schematic drawing of Ag-metal clusters in LTA-zeolite.
(upper right) Crystal structure of LTA-zeolite. A large hole with 1nm in a diameter exists.

Corpuscular irradiation can thus be expected to generate tracks of Ag clusters ordered parallel to the radiation beam. In this study, by analyzing their microstructures we verify that ordered tracks are formed within Ag-LTA (Linde Type A) membranes irradiated with Au ions.

Na-LTA membranes were fabricated on alumina substrates by hydrothermal synthesis, and Ag^+ ions exchanged for Na^+ by soaking the membranes in $AgNO_3$ solution for several days. Next, membranes were irradiated with Au ions at 200 MeV (1×10^{12} ions/cm^2) using the tandem accelerator at the Japan Atomic Energy Agency. After irradiation, membrane microstructures were observed using a TEM (JEOL JEM-2010 DM). Electric stopping powers of LTA were calculated with the SRIM code, and the results compared with cross-sectional TEM images of the membranes.

Fig. 2 shows a typical cross-sectional TEM image of an irradiated Ag-LTA membrane. Several dotted tracks are visible from the surface to the base of the membrane. These dots correspond to Ag-metal clusters; the diameter of the black dots is approximately 8~10 nm. All are oriented along the irradiation ion tracks. Light contrast between the Ag clusters indicates regions where the structure has become amorphous because of radiation damage. The size of the amorphous regions is almost the same as that of the Ag clusters, and is proportional to the energy density of the ion irradiation, as well as the magnitude of the membrane's

[1] Japan Fine Ceramics Center (JFCC)
[2] Japan Atomic Energy Agency (JAEA)

stopping power. The stopping power depends on the irradiation energy, the element being irradiated and the elements in the target material. Hence, the size and spatial distributions of the clusters can be controlled by controlling the irradiation conditions.

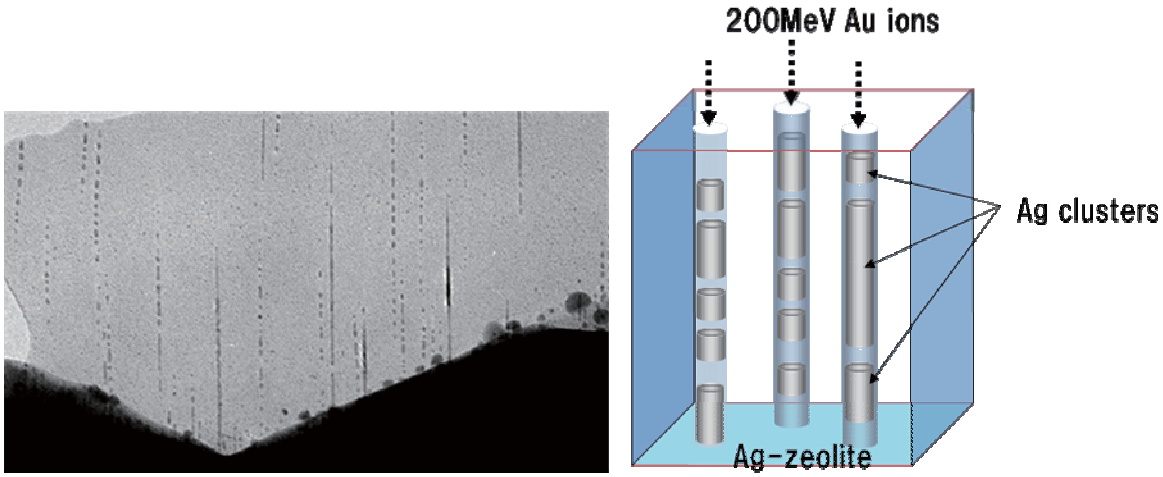

Fig. 2 A cross-sectional TEM image of an Ag-LTA membrane irradiated with an Au 200 MeV beam. Each dotted line corresponds to a track of Ag clusters. The size of each cluster is approximately 8~10 nm.

References

[1] Y. Sasaki and T. Suzuki, Mater. Trans., 50 (2009) 1050.

7.7 Surface amorphization in single crystalline Al_2O_3

N. Okubo[1], N. Ishikawa[1], M. Sataka[1] and S. Jitsukawa[1]

Aluminum oxide is expected as functional materials in a field of nuclear energy e.g. insulating materials, windows used for plasma diagnosis in a fusion reactor and inert matrix materials of geological disposal of high level radioactive waste. Recently, amorphization in ceramics such as the aluminum oxide, which affects the physical and mechanical properties, is attracted as a phenomenon induced by swift heavy ion irradiations with high-density electronic energy depositions (S_e) [1]. In previous studies, we have reported that amorphous phase is caused in polycrystalline aluminum oxide by ion irradiation with high-density electronic energy depositions (S_e), although lattice structure of the aluminum oxide is stable against nuclear energy depositions (S_n) [2]. The amorphization behaviors caused by high-density S_e depend on the specimen depth and grain orientation around the amorphized-crystalline region. We reported that new distorted lattice planes formed in the early stage of irradiation around the fluence of 5.0 x 10^{13} ions/cm^2 for single crystalline Al_2O_3 irradiated with 160 MeV-Xe ions [3]. Detailed mechanism of the amorphization induced by ion irradiation has not been clearly understood. In this report, the microstructures of single crystalline Al_2O_3 specimen irradiated by swift heavy ions are investigated by transmission electron microscope.

Single crystalline Al_2O_3 specimens were irradiated with several energies of Xe ions at ambient temperature, by using the Tandem Accelerator of JAEA. The irradiation energy range was from 70 to 160 MeV. The fluences were in the range from 1.0 x 10^{13} to 1.0 x 10^{15} ions/cm^2. After irradiations, XRD measurements and cross sectional TEM observations were conducted. The sapphire specimen irradiated of 160 MeV-Xe at 3.5 x 10^{14} ions/cm^2 was observed by TEM in order to confirm the cross sectional structure in this report.

An obvious boundary was observed in the cross sectional TEM image as shown in Fig.1 (a). The crystal structure of surface region above the boundary was identified as an amorphous phase and the deeper region as a single crystal by electron diffraction patterns. Distinct ion tracks, induced by passing of high energy particles, were vertically observed in depth of single crystalline region as shown in Fig.1 (b). The TEM contrast of ion tracks were decayed and disappeared as increasing the specimen depth. This result indicates that amorphization could be caused by overlapping of ion tracks. The projected range (R_p) of the 160 MeV Xe ions in the Al_2O_3 was about 10 μm calculated with the SRIM2000 [4]. The microstructure of the 10 μm depth, where the effect of S_n was maximum, was confirmed as a single crystal. The amorphization depth of the specimen irradiated at 3.5 × 10^{14} ions/cm^2 was around 800 nm. The TEM observations for other specimens irradiated at the fluence of 5.0 × 10^{13} and 1.0 × 10^{14} ions/cm^2 are undergoing.

[1] Japan Atomic Energy Agency(JAEA)

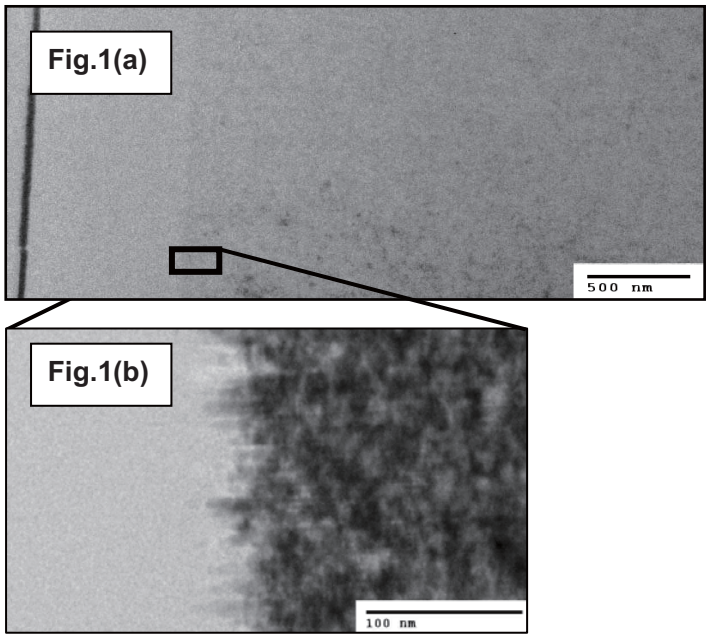

Fig.1 Cross sectional TEM images of single crystalline Al_2O_3 specimen irradiated by 160 MeV Xe ions. Total fluence was 3.5×10^{14} ions/cm^2.

References

[1] G. Szenes, J. Nucl. Mater., 336 (2005) 81-89.

[2] T. Aruga et al., Nucl. Instrum. Methods, B166-167(2000) 913-919.

[3] N. Okubo et al., JAERI TANDEM Annual Report 2004, JAEA-REVIEW 2005-004(2005)90.

[4] J.F. Ziegler, J.P. Biersack, U. Littmark, The Stopping and Range of Ions in Solids, (Pergamon Press, New York, 1985).

CHAPTER 8

Publication in Journal and Proceedings, and Contribution to Scientific Meetings

8.1 Accelerator Operation and Development
8.2 Nuclear Structure
8.3 Nuclear Reaction
8.4 Nuclear Chemistry
8.5 Nuclear Theory
8.6 Atomic Physics and Solid-state Physics
8.7 Radiation Effects in Materials

This is a blank page.

8.1 Accelerator Operation and Development

Journal/Proceedings

M. Matsuda
Present Status of JAEA-Tokai Tandem Accelertor
Proc. 7th Annual Meeting of Particle Accelerator Society of Japan, Himeji (Aug. 4-6, 2010) 15-17.

M. Matsuda, T. Asozu, M. Sataka, S. Hanashima, M. Nakamura, H. Kabumoto and K. Kutsukake
Development of Ion Beam Applications for JAEA-Tokai Tandem Accelerator
Proc. 23rd Meeting for Tandem Accelerators and their Associated Technologies, Tokyo, Univ. of Tokyo (July. 2- 3, 2010)65-68.

T. Asozu, H. Kabumoto, M. Ishizaki, M. Matsuda, T. Nakanoya, S. Abe and T. Ishii
Planning for Constructing the Beam lines at Tokai-Tandem Accelerator
Proc. 23rd Meeting for Tandem Accelerators and their Associated Techonologies, Tokyo, University of Tokyo (July. 2-3, 2010)127-130.

S.C. Jeong, M. Oyaizu, N. Imai, Y. Hirayama, H. Ishiyama, H. Miyatake, K. Niki, M. Okada,
Y.X. Watanabe, Y. Otokawa, A. Osa and S. Ichikawa
Wall-loss distribution of charge breeding ions in an electron cyclotron resonance ion source
Rev. Sci. Instrum., 82(2011)033508.

M. Okada, H. Ishiyama, I. Katayama, H. Miyatake, K. Niki, Y. Watanabe, H. Makii and S. Arai
Beam Test of Sawtooth-wave Pre-buncher Coupled to A Multilayer Chopper
Proc. 1st International Particle Accelerator Conference, Kyoto, Japan (May 23-28, 2010), Proc. IPAC'10 Kyoto, Japan (2010) 3906-3908.

K. Niki, H. Ishiyama, I. Katayama, H. Miyatake, M. Okada, Y. Watanabe, H. Makii and S. Arai
Design and Test of 2-4 MHz Sawtooth-wave Pre-buncher for 26 MHz-RFQ
Proc. 1st International Particle Accelerator Conference, Kyoto, Japan (May 23-28, 2010), Proc. IPAC'10 Kyoto, Japan (2010) 3903-3905.

Meetings

M. Matsuda
Present Status of JAEA-Tokai Tandem Accelertor
7th Annual Meeting of Particle Accelerator Society of Japan, Himeji (Aug. 4-6, 2010).

N. Ishizaki, T. Ishii, S. Abe, S. Hanashima, A. Osa, H. Tayama, M. Matsuda, T. Nakanoya, H. Kabumoto, M. Nakamura, K. Kutsukake, Y. Otokawa, T. Asozu and Y. Tsukihashi
Present Status of JAEA-Tokai Tandem Accelerator facility
23rd Meeting for Tandem Accelerators and their Associated Technologies, Tokyo, Japan (Jul. 2-3, 2010).

M. Matsuda, T. Asozu, M. Sataka, S. Hanashima, M. Nakamura, H. Kabumoto and K. Kutsukake
Development of Ion Beam Applications for JAEA-Tokai Tandem Accelerator
23rd Meeting for Tandem Accelerators and their Associated Technologies, Tokyo, Univ. of Tokyo (July. 2-3, 2010).

T. Asozu, H. Kabumoto, M. Ishizaki, M. Matsuda, T. Nakanoya, S. Abe and T. Ishii
Planning for Constructing the Beam lines at Tokai-Tandem Accelerator
23rd Meeting for Tandem Accelerators and their Associated Techonologies, Tokyo, Japan (July. 2-3, 2010).

M. Nakamura, M. Matsuda, T. Asozu, M. Sataka, K. Takahiro and N. Matsunami
Heavy ion Rutherford back scattering spectroscopy at JAEA-Tokai tandem accelerator
23rd Meeting for Tandem Accelerators and their Associated Technologies, Tokyo, Japan (Jul. 2-3, 2010).

Y. Otokawa, A. Osa, T.K. Sato and M. Matsuda
Development of radioactive ion beam production system at the JAEA-ISOL
23rd Meeting for Tandem Accelerators and their Associated Technologies, Tokyo, Japan (Jul. 2-3, 2010).

M. Okada, H. Ishiyama, I. Katayama, H. Miyatake, K. Niki, Y. Watanabe, H. Makii and S. Arai
Beam test of sawtooth-wave pre-buncher coupled to a multilayer chopper
1st International Particle Accelerator Conference, Kyoto, Japan (May 27, 2010).

K. Niki, H. Ishiyama, I. Katayama, H. Miyatake, M. Okada, Y. Watanabe, H. Makii and S. Arai
Design and test of 2-4 MHz sawtooth-wave pre-buncher for 26 MHz-RFQ
1st International Particle Accelerator Conference, Kyoto, Japan (May 27, 2010).

8.2 Nuclear Structure

Journal/Proceedings

M. Asai, K. Tsukada, H. Haba, Y. Ishii, T. Ichikawa, A. Toyoshima, T. Ishii, Y. Nagame, I. Nishinaka, Y. Kojima and K. Sueki
Neutron one-quasiparticle states in $^{251}Fm_{151}$ populated via the α decay of ^{255}No
Phys. Rev., C83(2011)014315.

H. Hayashi, Y. Kojima, M. Shibata and K. Kawade
Practical Q_β analysis method based on the Fermi-Kurie plot for spectra measured with total absorption BGO detector
Nucl. Instrum. Methods Phys. Res. A 613 (2010) 79-89.

D. Nagae, T. Ishii, R. Takahashi, M. Asai, H. Makii, A. Osa, T.K. Sato, S. Ichikawa, Y.R. Shimizu and T. Shoji
Lifetime measurements for the first 2^+ states in $^{162,164}Gd$ populated by the β decay of $^{162,164}Eu$
Proc. International Symposium on Exotic Nuclei, Sochi, Russia (Sep. 28-Oct. 2, 2009), AIP Conference Proceedings, 1224(2010)156-160.

M. Miyabe, M. Oba, H. Iimura, K. Akaoka, Y. Maruyama and I. Wakaida
Spectroscopy of laser-produced cerium plasma for remote isotope analysis of nuclear fuel
Appl. Phys., A101(2010)65-70.

R. Takahashi, T. Ishii, M. Asai, D. Nagae, H. Makii, K. Tsukada, A. Toyoshima, Y. Ishii, M. Matsuda, A. Makishima, T. Shizuma, T. Kohno and M. Ogawa
In-beam γ-ray spectroscopy of $^{248,250,252}Cf$ by neutron-transfer reactions using a Cf target
Phys. Rev., C81(2010)057303.

Meetings

H. Hayashi, M. Shibata, M. Asai, A. Osa, M. Oshima, A. Kimura, M. Koizumi and T.K. Sato
Development of total absorption detector using clover detector for Q_β measurements
International Conference on Nuclear Data for Science and Technology 2010, Jeju Island, Korea (Apr. 26-30, 2010).

H. Hayashi and M. Shibata
Total absorption detector @KISS
2nd KISS (KEK Isotope Separation System) Project Workshop, Wako, Japan (Mar. 5, 2011).

M. Asai
Strategy for approaching superheavy-nucleus spectroscopy
Fall Meeting of the Physical Society of Japan, Kitakyushu, Japan (Sep. 11-14, 2010).

M. Asai, K. Tsukada, Y. Kasamatsu, A. Toyoshima, T.K. Sato, Y. Nagame, N. Sato and T. Ishii
Systematic measurements of the first excited-state energies in even-even actinide nuclei
Annual Meeting of the Physical Society of Japan, Niigata, Japan (Mar. 25-28, 2011).

H. Iimura, H. Ohba, M. Oba, M. Miyabe and I. Wakaida
Development of resonance fluorescence spectroscopy of rare earth atoms generated by laser ablation
Fall Meeting of the Physical Society of Japan, Sakai, Japan (Sep. 26, 2010).

8.3 Nuclear Reaction

Journal/Proceedings

R. Graeger, D. Ackermann, M. Chelnokov, V. Chepigin, Ch.E. Duellmann, J. Dvorak, J. Even, A. Gorshkov, F,P. Hessberger, D. Hild, A. Huebner, E. Jaeger, J. Khuyagbaatar, B. Kindler, J.V. Kratz, J. Krier, A. Kuznetsov, B. Lommel, K. Nishio, H. Nitsche, J.P. Omtvedt, O. Petrushkin, D. Rudolph, J. Runke, F. Samadani, M. Schaedel, B. Schausten, A. Tueler, A. Yakushev and Q. Zhi
Experimental Study of the $^{238}U(^{36}S,3\text{-}5n)^{269\text{-}271}Hs$ reaction leading to the observation of ^{270}Hs
Phys. Rev., C81(2010)061601R.

K. Nishio, S. Hofmann, F. P. Heßberger, D. Ackermann, S. Antalic, Y. Aritomo, V. F. Comas, Ch. E. Düllmann, A. Gorshkov, R. Graeger, K. Hagino, S. Heinz, J. A. Heredia, K. Hirose, H. Ikezoe, J. Khuyagbaatar, B. Kindler, I. Kojouharov, B. Lommel, R. Mann, S. Mitsuoka, Y. Nagame, I. Nishinaka, T. Ohtsuki, A.G. Popeko, S. Saro, M. Schädel, A. Türler, Y. Watanabe, A. Yakushev and A. V. Yeremin
Nuclear orientation in the reaction $^{34}S+^{238}U$ and synthesis of the new isotope ^{268}Hs
Phys. Rev., C82(2010)024611.

K. Nishio, H. Ikezoe, I. Nishinaka, S. Mitsuoka, K. Hirose, T. Ohtsuki, Y. Watanabe, Y. Aritomo and S. Hofmann
Evidence for quasifission in the sub-barrier reaction of $^{30}Si+^{238}U$
Phys. Rev., C82(2010)044604-1-5.

J. Khuyagbaatar, F.P. Hessberger, S. Hofmann, D. Ackermann, V.S. Comas, S. Heinz, J.A. Heredia, B. Kindler, I. Kojouharov, B. Lommel, R. Mann, K. Nishio and A. Yakushev
The new isotope ^{236}Cm and new data on ^{233}Cm and $^{237,238,240}Cf$
Eur. Phys. J., A46(2010 59-67.

F.P. Hessberger, S. Antalic, B. Sulignano, D. Ackermann, S. Heinz, S. Hofmann, B. Kindler, J. Khuyagbaatar, I. Kojouharov, P. Kuusiniemi, M. Leino, B. Lommel, R. Mann, K. Nishio, A.G. Popeko, S. Saro, B. Streicher, J. Uusitalo, M. Venhart and A.V. Yeremin
Decay studies of K isomers in ^{254}No
Eur. Phys. J., A43(2010)55-56.

A.N. Andreyev, J. Elseviers, M. Huyse, P. Van Duppen, S. Antalic, A. Barzakh, N. Bree, T.E. Cocolios, V.F. Comas, J. Diriken, D. Fedorov, V. Fedosseev, S. Franchoo, J.A. Heredia, O. Ivanov, U. Koester, B.A. Marsh, K. Nishio, R.D. Page, N. Patronis, M. Seliverstov, I. Tsekhanovich, P. Van den Bergh, J. Van De Walle, M. Venhart, S. Vermote, M. Veselsky, C. Wagemans, T. Ichikawa, A. Iwamoto, P. Moeller and A.J. Sierk,
A new Type of Asymmetric Fission in Proton-Rich Nuclei
Phys. Rev. Lett., 105(2010) 52502-1-5.

K. Hirose, T. Ohtsuki, Y. Shibasaki, N. Iwase, J. Hori, K. Takamiya, H. Yashima, K. Nishio and Y. Kiyanagi
Multi-layered parallel plate ionization chamber for cross-section measurement of minor actinides
Nucl. Instrum. Methods Phys. Res., A621(2010)379-382.

K. Nishio
Effects of nuclear deformation on fusion process in heavy-element synthesis (in Japanense)
Nuclear Data News, 98(2011)34-43.

K. Nishio
Study for fusion-fission and quasifission in reactions using ^{238}U target nucleus
Proc. International Symposium on Quasifission Process in Heavy Ion Reactions, Messina, Italy, November 8-9, 2010. Journal of Physics: Conference Series 282(2011)012011(11pages).

I. Nishinaka, M. Tanikawa, Y. Nagame and H. Nakahara
Nuclear-charge polarization at scission in proton-induced fission of ^{233}U
Eur. Phys. J., A47(2009)9-1-8.

H. Makii, H. Ueda, Y. Temma, Y. Nagai, T. Shima, S. Fujimoto, M. Segawa, K. Mishima, J. Nishiyama and M. Igashira
E1 and E2 cross sections of the $^{12}C(\alpha,\gamma)^{16}O$ reaction at E_{eff} = 1.2 MeV using pulsed α beams
Proc. 10th International Symposium on Origin of Matter and Evolution of Galaxies, Osaka, Japan (Mar. 8-10, 2010), AIP Conference Proceedings, 1269(2010)283-288.

S. Mitsuoka, H. Ikezoe, K. Nishio, Y. Watanabe, S.C. Jeong, H. Ishiyama,
Y. Hirayama, N. Imai and H. Miyatake
Barrier distribution of quasi-elastic backward scattering in very heavyreaction systems
J. Modern Phys., E19(2010)989-996

Meetings

K. Nishio, I. Nishinaka, S. Mitsuoka, H. Makii, K. Furutaka, Y. Wakabayashi, R. Takahashi, T. Ishii, S. Chiba, K. Hirose and T. Ohtsuki
Fission fragment mass distribution for actinide nuclei produced by nucleon transfer reaction
Fall meeting of the Atomic Energy Society of Japan, Sapporo (Sept.15-17, 2010).

K. Nishio
Multiplicity and energy of neutrons from $^{233}U(n_{th},f)$ fission fragments
Workshop of the Espace de Structure Nucleaire Theorique, The scission process : the last stage of nuclear fission, Cedex, France (Apr. 12-16, 2010).

K. Nishio
Effects of nuclear orientation on fusion and fission process for reactions using ^{238}U target nucleus
24th International Nuclear Physics Conference 2010, Vancouver, Canada (Jul. 4-9, 2010).

K Nishio, H. Ikezoe, I. Nishinaka, S. Mitsuoka, K. Hirose, T. Ohtsuki, Y. Watanabe, Y. Aritomo and S. Hofmann
Fission dynamics in heavy ion collisions on ^{238}U
Scientific Workshop on Nuclear Fission and Dynamics and the Emission of Prompt Neutrons and Gamma Rays, Sinaia, Romania (Sept. 27-29, 2010).

K. Nishio
Fundamental Study for neutron-induced Fission
Workshop for ANNRI, Tokai, Japan (Feb. 24, 2011).

H. Makii, H. Miyatake, Y.X. Watanabe, N. Imai, H. Ishiyama, Y. Hirayama, K. Niki, M. Okada, S.C. Jeong, S. Chiba, S. Mitsuoka, K. Nishio and Y. Wakabayashi
Preparation of the measurement of the $^{12}C(\alpha,\gamma)^{16}O$ reaction at TRIAC
3rd International Conference of “Frontiers in Nuclear Structure, Astrophysics, and Reaction”, Rhodes Island, Greece (Aug. 23, 2010).

8.4 Nuclear Chemistry

Journal/Proceedings

A. Toyoshima, Y. Kasamatsu, K. Tsukada, M. Asai, Y. Ishii, H. Toume, I. Nishinaka, T.K. Sato, Y. Nagame, H. Haba, S. Goto, H. Kudo, K. Akiyama, Y. Oura, K. Ooe, A. Shinohara, K. Sueki, M. Schädel and J.V. Kratz
Extraction Chromatographic Behavior of Rf, Zr, and Hf in HCl Solution with Styrene-divinylbenzene Copolymer Resin Modified by TOPO (trioctylphosphine oxide)
J. Nucl. Radiochem. Sci., 11(2010)7.

H. Haba, D. Kaji, H. Kikunaga, Y. Kudou, K. Morimoto, K. Morita, K. Ozeki, T. Sumita, A. Yoneda, Y. Kasamatsu, Y. Komori, K. Ooe and A. Shinohara
Production and decay properties of the 1.9-s isomeric state in ^{261}Rf
Phys. Rev., C83(2011)034602.

Meetings

M. Schädel
Chemistry of Superheavy Elements – Experimental Achievements and Perspectives
54th Symposium on Radiochemistry, Suita, Japan (Sept. 27-29, 2010).

M. Schädel
Chemistry of superheavy elements: Experimental achievements and perspectives
International Chemical Congress of Pacific Basin Societies, Honolulu, Hawaii (Dec. 15-20, 2010).

Y. Nagame
The recent superheavy element chemistry at JAEA
2nd International Conference on Application of Radiotracers in Chemical, Environmental and Biological Sciences, Kolkata, India (Nov. 7-13, 2010).

A. Toyoshima
Electrochemistry of the heaviest elements
International Chemical Congress of Pacific Basin Societies, Honolulu, Hawaii (Dec. 15-20, 2010).

T. Kikuchi, A. Toyoshima, Z.J. Li, K. Tsukada, M. Asai, T.K. Sato, N. Sato, Y. Nagame, Y. Kasamatsu and F.L. Fan
α-HiB complexation and ion-exchange behavior of the group-4 elements as homologues of Rf
54th Symposium on Radiochemistry, Suita, Japan (Sept. 27-29, 2010).

N. Sato, M. Asai, K. Tsukada, T. Sato, A. Toyoshima, Z.J. Li, T. Kikuchi, Y. Kaneya, S. Ichikawa, Y. Nagame and M. Schädel
Development of a gas-jet surface ionizer coupled to a gas-jet transport system for the measurement of the first ionization potential for Lr
54th Symposium on Radiochemistry, Suita, Japan (Sept. 27-29, 2010).

N. Sato, M. Asai, K. Tsukada, T.K. Sato, A. Toyoshima, Z.J. Li, Y. Nagame, S. Ichikawa and M. Schädel
Measurement of the first ionization potential of Lr
International Chemical Congress of Pacific Basin Societies, Honolulu, Hawaii, USA (Dec. 15-20, 2010).

T.K. Sato, K. Tsukada, M. Asai, A. Toyoshima, N. Sato, Z.J. Li, Y. Kasamatsu, T. Kikuchi, X. Liang, Y. Kaneya, Y. Nagame and M. Schädel
On-line isothermal gas chromatographic behavior of the group-5 elements Nb and Ta as homologue of Db
54th Symposium on Radiochemistry, Suita, Japan (Sept. 27-29, 2010).

T.K. Sato, K. Tsukada, M. Asai, A. Toyoshima, Y. Kasamatsu, Y. Ishii, Z.J. Li, N. Sato, T. Kikuchi, S. Liang, Y. Nagame and M. Schädel
On-line isothermal gas chromatographic behavior of group-5 elements as homologues of Db
International Chemical Congress of Pacific Basin Societies, Honolulu, Hawaii (Dec. 15-20, 2010).

T.K. Sato, M. Asai, K. Tsukada, A. Toyoshima, N. Sato, Z.J. Li, T. Kikuchi, Y. Kaneya, Y. Nagame and M. Schädel
On-line isothermal gas chromatography of oxychlorides of Db (Z=105) and homologues Nb and Ta
Spring Meeting of the Chemical Society of Japan, Yokohama, Japan (Mar. 26-29, 2011).

S. Goto, H. Murayama, T. Kojima, M. Murakami, S. Goto, H. Kudo, K. Tsukada, M. Asai, T. K. Sato, A. Toyoshima, N. Sato and Y. Nagame
Studies on isothermal chromatographic behavior of Zr and Hf chlorides for the gas phase chemistry of Rf
Annual Meeting of the Chemical Society of Japan (Mar. 11, 2011).

S. Ikarashi, K. Sueki, K. Tsukada and Y. Nagame
Study on the adsorption rate of Zr and Hf as homologues of element 104, Rutherfordium, on the cation-exchange resin in H_2SO_4 solutions
54th Symposium on Radiochemistry, Suita, Japan (Sept. 27-29, 2010).

X. Liang, Z. Li, K. Tsukada, A. Toyoshima, M. Asai, T.K. Sato, N. Sato, T. Kikuchi, Y. Kaneya and Y. Nagame
Anion-exchange behavior of the group-6 elements in HF/HNO_3 mixed solutions - Towards the study of ion-exchange behavior of $_{106}Sg$ -
54th Symposium on Radiochemistry, Suita, Japan (Sept. 27-29, 2010).

K. Tsukada, Y. Kasamatsu, M. Asai, A. Toyoshima, Y. ishii, Z.J. Li, T.K. Sato, Y. Nagame, M. Schädel, S. Goto, T. Hasegawa, H. Kudo, H. Haba, Y. Kudou, H. Kikunaga, K. Ooe, H. Fujisawa, W. Sato, A. Shinohara, Y. Oura, K. Akiyama, T. Nanri, M. Araki and A. Yokoyama
Anion-exchange behavior of Db in HF and HNO_3 mixed solution using an on-line chemical apparatus
International Chemical Congress of Pacific Basin Societies, Honolulu, Hawaii (Dec. 15-20, 2010).

Z.J. Li, A. Toyoshima, K. Tsukada, M. Asai, Y. Kasamatsu, T. Sato, N. Sato, T. Kikuchi, X. Liang, Y. Nagame, H. Haba, S. Goto, K. Akiyama, M. Nishikawa, T. Takeda, M. Murakami, S. Igarashi and K. Sueki
Cation-exchange behavior of rutherfordium, $_{104}Rf$, in H_2SO_4/HNO_3 mixed solutions ($[H^+] = 1.0$ M)
International Chemical Congress of Pacific Basin Societies, Honolulu, Hawaii (Dec. 15-20, 2010).

Z.J. Li, A. Toyoshima, M. Asai, K. Tsukada, T.K. Sato, N. Sato, T. Kikuchi, M. Schädel, Y. Nagame, X.H. Liang, Y. Kasamatsu, Y. Komori, K. Ooe, A. Shinohara, S. Goto, H. Murayama, M. Murakami, H. Kudo, H. Haba, Y. Takeda, M. Nishikawa, A. Yokoyama, S. Ikarashi, K. Sueki and K. Akiyama
Sulfate complexation of element 104, Rf, in H_2SO_4/HNO_3 mixed solution ($[H^+] = 1.0$ M)
54th Symposium on Radiochemistry, Suita, Japan (Sept. 27-29, 2010).

K. Tsukada, Y. Kasamatsu, M. Asai, A. Toyoshima, Y. Ishii and Y. Nagame
New apparatus AIDA-II for aqueous chemistry of the heaviest elements
International Chemical Congress of Pacific Basin Societies, Honolulu, Hawaii (Dec. 15-20, 2010).

H. Murayama, T. Kojima, M. Murakami, S. Goto, H. Kudo, K. Tsukada, M. Asai, A. Toyoshima, T. K. Sato, N. Sato and Y. Nagame
Research on gas phase chemistry for chloride of the group-4 elements
54th Symposium on Radiochemistry, Osaka, Japan (Sept. 27, 2010).

H. Murayama, M. Murakami, S. Goto, H. Kudo, K. Tsukada, M. Asai, A. Toyoshima, T. K. Sato and Y. Nagame
Gas chromatographic behavior of chloride compounds of group-4 elements
International Chemical Congress of Pacific Basin Societies, Hawaii, USA (Dec. 18, 2010).

I. Nishinaka, K. Nishio, M. Tanikawa, H. Makii, Y. Wakabayashi, S. Mitsuoka, and M. Asai
Fission fragment anisotropy in heavy-ion-induced fission of actinides
Annual Meeting of the Japan Society of Nuclear and Radiochemical Sciences, Osaka, Japan, (Sept. 27, 2010).

8.5 Nuclear Theory

Journal/Proceedings

A. N. Deacon, J. F. Smith, S. J. Freeman, R. V. F. Janssens, M. P. Carpenter, B. Hadinia, C. R. Hoffman, B. P. Kay, T. Lauritsen, C. J. Lister, D. O'Donnell, J. Ollier, T. Otsuka, D. Seweryniak, K.-M. Spohr, D. Steppenbeck, S. L. Tabor, V. Tripathi, Y. Utsuno, P. T. Wady and S. Zhu
Cross-shell excitations near the "island of inversion": Structure of ^{30}Mg
Phys. Rev., C82(2010)034305-1-7.

N. Shimizu, Y. Utsuno, T. Mizusaki, T. Otsuka. T. Abe and M. Honma
Novel extrapolation method in the Monte Carlo shell model
Phys. Rev., C82 (2010)061305(R)-1-5.

Y. Utsuno and S. Chiba
Multiparticle-multihole states around ^{16}O and correlation-energy effect on the shell gap
Phys. Rev., C83(2011)021301(R)-1-5.

R. Kanungo, A. Prochazka, W .Horiuchi, C. Nociforo, T. Aumann, D. Boutin, D. Cortina-Gil, B. Davids, M. Diakaki, F. Farinon, H. Geissel, R. Gernhauser, J. Gerl, R. Janik, B. Jonson, B. Kindler, R. Knobel, R. Krucken, M. Lantz, H. Lenske, Y. Litvinov, B. Lommel, K. Mahata, P. Maierbeck, A. Musumarra, T. Nilsson, C. Perro, C. Scheidenberger, B. Sitar, P. Strmen, B. Sun, Y .Suzuki, I. Szarka, I. Tanihata, Y. Utsuno, H .Weick and M. Winkler
Matter radii of $^{32-35}$Mg
Phys. Rev., C83(2011)021302(R)-1-4.

K. Oyamatsu, K. Iida and H. Koura
Neutron drip line and the equation of state of nuclear matter
Phys. Rev., C 82(2010) 027301.

H. Koura
Symmetry energy of nuclear masses and Wigner term
Genshikaku-Kenkyu, 55(2010) 3-63 (in Japanese).

T. Tachibana, H. Koura and J. Katakura
Chart of the Nuclides 2010
Japanese Nuclear Data Committee and Nuclear Data Center, Japan Atomic Energy Agency (2010).

H. Koura and S. Chiba (ed.)
Proceeding of the 2009 Annual Symposium on Nuclear Data (NDS 2009),
JAEA-Conf 2010-005(2010).

Meetings

Y. Utsuno, T. Otsuka, B.A. Brown, M. Honma, T. Mizusaki, and N. Shimziu
Shell-model approach to exotic nuclei—description by monopole-based universal interaction and development of a new MCSM code
ECT Workshop "Reactions and Nucleon Properties in Rare Isotopes", Trento, Italy (Apr. 6, 2010).

Y. Utsuno, N. Shimizu, T. Abe, and T. Otsuka
Fast computation of two-body matrix elements in the Monte Carlo shell model
Fall Meeting of the Physical Society of Japan, Kitakyushu, Japan (Sept. 11, 2010).

Y. Utsuno
Advances in the study of unstable nuclei with the shell model
Workshop on "Advances in the Nuclear-Structure Study and Its Application," Tokyo, Japan (Oct. 16, 2010).

Y. Utsuno
Structure of unstable nuclei around N=28 described by a shell model with the monopole-based universal interaction
International Symposium "New Faces of Atomic Nuclei", Okinawa, Japan (Nov. 17, 2010).

Y. Utsuno
Shell-model study on the island of inversion: what has been clarified and what should be
RIKEN RIBF Workshop "Towards the Understanding of "Island of Inversion" via Electromagnetic Moment and Direct Reaction," Wako, Japan (Dec. 20, 2010).

Y. Utsuno
Towards petascale nuclear-structure calculation: shell-model case
French-Japanese Symposium on Nuclear Structure Problems, Wako, Japan (Jan. 6, 2011).

Y. Utsuno, T. Otsuka, S. Chiba, M. Honma, T. Mizusaki, N. Shimizu and N. Tsunoda
Half-life calculation of ^{79}Se
Workshop on "Nuclear Physics and Atomic Energy," Tokyo, Japan (Mar. 10, 2011).

H. Koura
Calculation of fission barrier in the heavy and super-heavy mass region by using spherical-basis method
3rd International Conference on Current Problems in Nuclear Physics and Atomic Energy, Kyiv, Ukraine (Jun. 7 - 12, 2010).

H. Koura
Global properties of nuclear masses and decays in the neutron-richmass region - influence to the r-process nucleosynthesis -
2nd OMEG Institute seminar, RIKEN (Wako) (Jul. 15, 2010).

H. Koura
Alchemy in Universe ---Origin of atoms and nuclei---
Summer seminarin 'Deru-kui' program promoted by Waseda University,sponsored by the JST program:'Training for future scientists', Kamogawa, Japan (Jul. 27, 2010).

H. Koura
Why does the nuclei decay? ---Stability and decay modes of nuclei ---
49th Summer School of Nuclear Chemistry, Miharu, Fukushima, Japan (Aug. 30, 2010).

H. Koura, O. Iwamoto and S. Chiba
Approval condition of the surrogate ratio method and its verification
Fall Meeting of Atomic Energy Society of Japan, Sapporo, Japan (Sept. 16, 2010).

Y. Aritomo, S. Chiba and S. Hashimoto
Analysis of surrogate reaction with unified model
Annual meeting of the Physical Society of Japan, Okayama, Japan (Mar. 20, 2010).

Y. Aritomo, S. Chib, S. Hashimoto, Y. Utsuno and H. Koura
Description of surrogate reaction with unified model
Annual Meeting of the Atomic Energy Society of Japan, Mito, Japan (Mar. 27, 2010).

S. Hashimoto, K. Ogata, S. Chiba and M. Yahiro
Systematic analysis of reaction cross section for deuteron induced reaction
Second EMMI-EFES Workshop on Neutron-Rich Exotic Nuclei, Wako (Jun. 16, 2010).

S. Hashimoto, K. Ogata, S. Chiba and M. Yahiro
Determination of critical radius and systematic analysis of total reaction cross section with Continuum-Discretized Coupled-Channel method
RCNP workshop on nuclear reaction, Ibaraki, Japan (Aug. 2-4, 2010).

S. Hashimoto, K. Ogata, S. Chiba and M. Yahiro
Systematic analysis of reaction cross section for deuteron induced reaction with Continuum-Discretized Coupled-Channel method
Fall meeting of the physical society of Japan, Kitakyushu, Japan (Sept. 11-14, 2010).

K. Ogata, S. Hashimoto and S. Chiba
Investigation on the Surrogate method with the Continuum-Discretized Coupled-Channel method
Fall meeting of the physical society of Japan, Kitakyushu, Japan (Sept. 11-14, 2010).

Y. Watanabe, T. Ye, S. Hashimoto, K. Ogata and M. Yahiro
Systematic analysis of (d,xn) and (d,xp) breakup reactions for energies up to 100 MeV
Fall meeting of the Atomic energy society of Japan, Sapporo, Japan (Sept. 15-17, 2010).

S. Hashimoto and M. Kohno
Analysis of (K^-,K^+) reaction and Ξ-nucleus potential with semi-classical distorted wave model
KEK theory center workshop on Strangeness nuclear physics 2010, Tsukuba, Japan (Dec. 2-4, 2010).

S. Hashimoto, K. Ogata, S. Chiba and M. Yahiro
Analysis of incomplete and complete fusion in deuteron induced reaction with eikonal reaction theory
Annual meeting of the physical society of Japan, Niigata, Japan (Mar. 25-28, 2011).

8.6 Atomic Physics and Solid-state Physics

Journal/Proceedings

N. Matsunami, J. Fukushima, M. Sataka, S. Okayasu H. Sugai and H. Kakiuchida
Electrical property modifications of In-doped ZnO films by ion irradiation
Nucl. Instrum. Methods, B268(2010)3071.

N. Matsunami, M. Sataka, S. Okayasu and H. Kakiuchida
Ion irradiation effects on tungsten-oxide films and charge state effect on electronic erosion
Nucl. Instrum. Methods, B268(2010)3167.

Meetings

M. Imai, M. Sataka, K. Kawatsura, K. Takahiro, K. Komaki, H. Shibata, H. Sugai and K. Nishio
Equilibrium and non-equilibrium Charge State Distribution of 2 MeV/u Carbon Ions Passing through Carbon Foils
24th International Conference on Atomic Collisions in Solids, Krakow, Poland (Jul. 18-23, 2010).

N. Matsunami, J. Fukushima, M. Sataka, S. Okayasu H. Sugai and H. Kakiuchida,
Modification of In-doped ZnO properties by high-energy ions
Fall Meeting, Japan Physical Society, Okayama, Japan (Sept. 23, 2010).

N. Matsunami, M. Katoh, M. Sataka, and S. Okayasu
Effects of incident charge of high-energy ions on decomposition of copper nitride
24th International Conference on Atomic Collision in solids, Krakou, Poland (Jul. 18-23,2010).

8.7 Radiation Effects in Materials

Journal/Proceedings

N. Ishikawa, K. Ohhara, Y. Ohta and O. Michikami
Binomial distribution function for intuitive understanding of fluence dependence of non-amorphized ion-track area
Nuclear Instrum. Methods, B268(2010)3273.

T. Sonoda, M. Kinoshita, N. Ishikawa, M. Sataka, A. Iwase and K. Yasunaga
Clarification of high density electronic excitation effects on the microstructural evolution in UO_2
Nuclear Instrum. Methods, B268(2010)3277.

Y. Tahara, B. Zhu, S. Kosugi, N. Ishikawa, Y. Okamoto, F. Hori, T. Matsui and A. Iwase
Study on effects of swift heavy ion irradiation on the crystal structure in CeO_2 doped with Gd_2O_3
Nuclear Instrum. Methods Phys. Res., B269(2011)886-889.

B. Zhu, H. Ohno, S. Kosugi, F. Hori, K. Yasunaga, N. Ishikawa and A. Iwase
Effects of swift heavy ion irradiation on the structure of Er_2O_3-doped CeO_2
Nuclear Instrum. Methods Phys. Res., B268(2010)3199-3202.

H. Amekura, N. Ishikawa, N. Okubo, M. C. Ridgway, R. Giulian, K. Mitsuishi, Y. Nakayama, C. Buchal, S. Mantl, and N. Kishimoto
Zn nanoparticles irradiated with swift heavy ions at low fluences: Optically-detected shape elongation induced by nonoverlapping ion tracks
Phys. Rev., B83(2011)205401.

Meetings

N. Ishikawa and K. Takegahara
Irradiation damage due to electronic excitation in CeO_2 irradiated with high-energy heavy ions
International conference on ion beam modification in materials, Montreal, Canada (Aug. 22, 2010).

N. Ishikawa
Electronic excitation and formation of lattice defects due to high-energy particle irradiation
Lattice defect forum, Osaka, Japan (Sept.21, 2010).

K. Takegahara and N. Ishikawa
Radiation effects by high-density electronic excitation in CeO_2 irradiated with high-energy ions
11th meeting on surface analysis using ion beam, Nagoya, Japan (Nov. 3, 2010).

N. Ishikawa, T. Sonoda, Y. Okamoto, T. Sawabe, K. Takegahara, S. Kosugi and A. Iwase
X-ray study of radiation damage in UO_2 irradiated with high-energy heavy ions
International conference on nuclear materials: NuMat 2010, Karlsruhe, Germany (Oct. 4, 2010).

K. Takegahara and N. Ishikawa
Radiation effects by high-density electronic excitation in CeO_2 irradiated with high-energy ions
Fall Meeting of the Physical Society of Japan, Osaka, Japan (Sept. 23, 2010).

K. Shimizu, Y. Tahara, S. Kosugi, N. Fujita, T. Matsui, F. Hori, A. Iwase, Yasunaga and N. Ishikawa
Magnetism of CeO_2 induced by energetic heavy swift ion irradiation
KUR Workshop on materials irradiation effects and application, Osaka Japan (Dec. 17, 2010).

Y. Tahara, K. Shimizu, N. Ishikawa, Y. Okamoto, F. Hori, T. Matsui and A. Iwase
Study on Effects of Energetic Ion Irradiation in Gd_2O_3-doped CeO_2 by Means of Synchrotron Radiation X-ray Spectroscopy
Spring Meeting of European Material Research Society, Nice France (May 10, 2011).

Y. Tahara, B. Zhu, S. Kosugi, N. Ishikawa, Y. Okamoto, F. Hori, T. Matsui and A. Iwase
Study on effects of swift heavy ion irradiation on the crystal structure in CeO_2 doped with Gd_2O_3
24th International Conference on Atomic Collisions in Solids, Krakow, Poland (Jul. 25, 2010).

H. Amekura, N. Ishikawa, R. Giulian, M.C. Ridgway, Ch. Buchal, S. Mantl and N. Kishimoto
Elongation of Metal Nanoparticles Embedded in Silica Induced by a Single Ion Impact
24th International Conference on Atomic Collisions in Solids, Krakow, Poland (Jul. 20, 2010).

H. Amekura, N. Ishikawa, N. Okubo, R. Giulian, M.C. Ridgway, Ch. Buchal, S. Mantl and N.Kishimoto
Single-ion-impact Induced Elongation of Zn Nanoparticles Embedded in Silica
17th International Conference on Ion Beam Modification of Materials, Montreal, Canada (Aug. 23, 2010).

H. Amekura
Optical Detection of Irradiation effects of Swift Heavy Ions on Zn and ZnO Nanoparticles in Silica
Conference on Swift Heavy Ions in Materials engineering and Characterization, New Delhi, India (Oct. 7, 2010).

H. Amekura, N. Ishikawa, N. Okubo, R. Giulian, M.C. Ridgway and N. Kishimoto
Elongation of Embedded Nanoparticles Induced by Non-overlapped Impacts of Swift Heavy Ions Detected by Optical Dichroism
20th MRS-J Academic Symposium, Yokohama, Japan (Dec. 21, 2010).

M. Sasase, S. Okayasu and H. Yamamoto
Radiation effects for film formation and nano-structural changes of iron disilicide thin film
17th International Conference on Ion Beam Modification of Materials, Montreal, Canada (Aug. 23, 2010).

Y.Sasaki、M. Kobayashi, H. Kita and S. Okayasu
Formation of metal microstructures induced by heavy ion irradiation in Ag-zeolite
2nd International Symposium on Advanced Microscopy and Theoretical Calculations(Jun. 24-26, 2010).

CHAPTER 9

Personnel and Committee

9.1 Personnel
9.2 Research Planning and Assessment Committee

This is a blank page.

9.1 Personnel

Department of Research Reactor and Tandem Accelerator

Kiyonobu	Yamashita	Director
Takeshi	Maruo	Deputy Director
Tetsuro	Ishii	Deputy Director
Shuji	Yoshinari	Manager of Administration Section
Masao	Sataka	(temporary staff)
Suehiro	Takeuchi	(temporary staff)

Department of Research Reactor and Tandem Accelerator

Tandem Accelerator Section *(* General Manager)*

Scientific Staff

Tetsuro	Ishii*
Makoto	Matsuda

Technical Staff

Susumu	Hanashima	
Shin-ichi	Abe	
Nobuhiro	Ishizaki	
Hidekazu	Tayama	
Takamitsu	Nakanoya	
Hiroshi	Kabumoto	
Masahiko	Nakamura	
Ken-ichi	Kutsukake	
Yoshinori	Otokawa	
Takuhiro	Asozu	
Yoshihiro	Tsukihashi	(temporary staff)

Entrusted Operators

Takahiro	Yoshida
Takayuki	Ishiguro
Kazushi	Yamaguchi
Nobuo	Seki
Teruo	Onodera
Hikaru	Nisugi

Department of Radiation Protection

Facility Radiation Control Section I

Kunio	Kawarai	
Hayato	Hiraga	
Tomoyo	Fukami	
Daisuke	Higashi	
Susumu	Kinase	

Advanced Science Research Center

Sadamichi	Maekawa	Director
Yuichiro	Nagame	Deputy Director
Hiroshi	Ikezoe	(temporary staff)

Advanced Science Research Center

Research Group for Shell Structure and Reaction Properties of Heavy Nuclei far from Stability *(* Group Leader)*

Satoshi	Chiba*	
Toshiki	Maruyama	
Shin-ichi	Mitsuoka	
Katsuhisa	Nishio	
Hiroyuki	Koura	
Yutaka	Utsuno	
Ichiro	Nishinaka	
Hiroyuki	Makii	
Yoshihiro	Aritomo	(Special Topic Researcher)
Shintaro	Hashimoto	(Post Doc.)
Yasuo	Wakabayashi	(Post Doc.)
Ryuta	Takahashi	(Student)

Advanced Science Research Center

Research Group for Superheavy Elements *(* Group Leader)*

Matthias	Schädel*	
Kazuaki	Tsukada	
Masato	Asai	
Tetsuya K.	Sato	
Atsushi	Toyoshima	(Senior Postdoc.)
Zi Jie	Li	(Post Doc.)
Nozomi	Sato	(Postdoc.)
Takahiro	Kikuchi	(Student)
Yusuke	Kaneya	(Student)

Advanced Science Research Center

Research Group for Mechanical Control of Materials and Spin Systems

Satoru Okayasu (Deputy Group Leader)

Nuclear Technology and Education Center

Nobuo Shinohara

Hiroyuki Sugai

Nuclear Science and Engineering Directorate

Innovative Nuclear Science Research Group *(* Group Leader)*

Hideo Harada*

Hideki Iimura

Mitsuo Koizumi

Kazuyoshi Furutaka

Fumito Kitatani

Shoji Nakamura

Yosuke Toh

Atsushi Kimura

Kaoru Hara (Senior Post Doc.)

Tadahiro Kin (Senior Post Doc.)

Futoshi Minato (Post Doc.)

Masumi Oshima (temporary staff)

Nuclear Science and Engineering Directorate

Research Group for Radiation Materials Engineering

Shiro Jitsukawa

Norito Ishikawa

Nariaki Okubo

Nuclear Engineering Research Collaboration Center,

Nuclear Science and Engineering Directorate

Special group for RI generation technology using accelerator neutrons(* *Group Leader*)

Yasuki Nagai*

Quantum Beam Science Directorate

Gamma-ray Non-Destructive Assay Research Group

Toshiyuki Shizuma

Takehito Hayakawa

Quantum Beam Science Directorate

Neutron Imaging and Activation Analysis Group

Yuichi Hatsukawa

High Energy Accelerator Research Organization (KEK)
- Institute of Particle and Nuclear Studies –

Radioactive Nuclear Beams Project Group *(* Group Leader)*

Sun-Chan Jeong*
Hiroari Miyatake
Hironobu Ishiyama
Yutaka Watanabe
Nobuaki Imai
Yoshikazu Hirayama
Michihiro Oyaizu
Shoji Suzuki

High Energy Accelerator Research Organization (KEK)
- Accelerator Laboratory -

Kazuaki Niki
Masashi Okada

9.2 Research Planning and Assessment Committee

Chairman	Kouichiro	Asahi	(Professor, Tokyo Institute of Technology)
Member	Tadashi	Kambara	(Senior Scientist, RIKEN)
	Kenji	Kimura	(Professor, Kyoto University)
	Shigeo	Tomita	(Associate Professor, Tsukuba University)
	Toshiaki	Kaneko	(Professor, Okayama University of Science)
	Hisaaki	Kudo	(Professor, Niigata University)
	Eiji	Ideguchi	(Lecturer, The University of Tokyo)
	Hitoshi	Nakata	(Professor, Chiba University)
	Koichi	Hagino	(Associate Professor, Tohoku University)
	Tomotsugu	Sawai	(Nuclear Science and Engineering Directorate, JAEA)
	Hideo	Harada	(Nuclear Science and Engineering Directorate, JAEA)
	Yuichi	Hatsukawa	(Quantum Beam Science Directorate, JAEA)
	Tetsuro	Ishii	(Dep. Research Reactor and Tandem Accelerator, JAEA)
	Masao	Sataka	(Dep. Research Reactor and Tandem Accelerator, JAEA)
	Kiichi	Hojo	(Advanced Science Research Center, JAEA)
Organizer Secretary			
	Shin-ichi	Mitsuoka	(Advanced Science Research Center, JAEA)
	Norito	Ishikawa	(Nuclear Science and Engineering Directorate, JAEA)
	Masato	Asai	(Advanced Science Research Center, JAEA)
	Hiroshi	Ikezoe	(Advanced Science Research Center, JAEA)

This is a blank page.

CHAPTER 10

Cooperative Researches and Common Use in JAEA

10.1 Cooperative Research Programs
10.2 Common Use Programs in JAEA

This is a blank page.

10.1 Cooperative Research Programs

Title	Contact Person & Organization
1. In-beam g-ray spectroscopy of neutron- deficient actinide nuclei using heavy-ion induced transfer reactions	Toshiyuki KOHNO Tokyo Institute of Technology
2. Reduction of mendelevium using an electrochemistry apparatus	Atsushi SHINOHARA Osaka University
3. Barrier distribution derived from quasi-electric backscattering in heavy nucleus-nucleus collision leading to superheavy element production	Sun-Chan JEONG High Energy Accelerator Research Organization
4. Development of gas-cell laser spectroscopy for the measurement of nuclear radii of unstable tungsten isotopes	Takayoshi HORIGUCHI Hiroshima International Univ.
5. Experimental assignment of single-particle configurations in superheavy nuclei by means of α fine structure spectroscopy	Keisuke SUEKI Univ. of Tsukuba
6. Coulomb excitation experiment of ^{126}Xe	Eiji IDEGUCHI Univ. of Tokyo
7. Fission fragment anisotropy in heavy-ion-induced fission of actinides.	Akihiko YOKOYAMA Kanazawa Univ.
8. Study for quasi-fission process in the heavy-ion reactions using ^{238}U target nucleus	Tsutomu OHTSUKI Tohoku University
9. Development and generation of ^{211}Rn/^{211}At generator for long-distance shipping of short-lived radioisotope ^{211}At for medical use	Akihiko YOKOYAMA Kanazawa Univ.
10. Study of damage formation process under high-energy fission fragment irradiation fields	Takeshi SONODA Central Research Institute of Electric Power Industry
11. Control of electronic and magnetic properties of heavy element oxides by using high density electroonic excitation due to swift heavy ions	Akihiro IWASE Osaka Prefecture University
12. Electronic excitation effects and material modifications of non-metallic ceramics by high-energy ions	Noriaki MATSUNAMI Nagoya University

13. Charge state evolution of heavy ions passing through solid targets	Makoto IMAI Kyoto University
14. Metal-semiconductor transition control on a FeSi2 thin film with high energy heavy ion irradiations	Masato SASASE The Wakasa-wan Energy Research Center
15. Nano-fabrication of zeolite with high energy ion irradiations	Yukichi SASAKI Japan Fine Ceramics Center

10.1 Cooperative Research Programs (contd.) using TRIAC

Title	Contact Person & Organization
1. Development of accelerator technology for short-lived radioactive nuclear beam	Sun-Chan JEONG High Energy Accelerator Research Organization
2. Measurement of the $^{12}C(\alpha,\gamma)^{16}O$ cross sections by using TRIAC	Hiroari MIYATAKE High Energy Accelerator Research Organization (KEK)
3. Development of spin-polarized radioactive nuclear beam for nuclear spectroscopy through b-delayed decay of spin-polarized nuclei around doubly magic nucleus ^{132}Sn	Yoshikazu HIRAYAMA High Energy Accelerator Research Organization
4. Extremely safe Coulomb excitation of ^{142}Ba	Nobuaki IMAI High Energy Accelerator Research Organization

10.2 Common Use Programs in JAEA

Title	Contact Person & Organization
1. Shape and property control of Zn and ZnO nanoparticles by Swift Heavy Ions	Hiroshi AMEKURA National Institute for Materials Science (NIMS)
2. Study on effects of energetic ion irradiation in Gd_2O_3-doped CeO_2 by means of synchrotron radiation X-ray spectroscopy heavy ion irradiation induced ferromagnetism in FeRh alloys	Akihiro IWASE Osaka Prefecture University
3. Morphological change in metal nano-particles induced by swift heavy ion irradiation	Syo MATSUMURA Kyushu University
4. Studies on volatile behavior of Zr and Hf chlorides	Shin-ichi GOTO Niigata University

This is a blank page.

国際単位系（SI）

表１．SI 基本単位

基本量	SI 基本単位	
	名称	記号
長さ	メートル	m
質量	キログラム	kg
時間	秒	s
電流	アンペア	A
熱力学温度	ケルビン	K
物質量	モル	mol
光度	カンデラ	cd

表２．基本単位を用いて表されるSI組立単位の例

組立量	SI 基本単位	
	名称	記号
面積	平方メートル	m^2
体積	立法メートル	m^3
速さ，速度	メートル毎秒	m/s
加速度	メートル毎秒毎秒	m/s^2
波数	毎メートル	m^{-1}
密度，質量密度	キログラム毎立方メートル	kg/m^3
面積密度	キログラム毎平方メートル	kg/m^2
比体積	立方メートル毎キログラム	m^3/kg
電流密度	アンペア毎平方メートル	A/m^2
磁界の強さ	アンペア毎メートル	A/m
量濃度(a)，濃度	モル毎立方メートル	mol/m^3
質量濃度	キログラム毎立法メートル	kg/m^3
輝度	カンデラ毎平方メートル	cd/m^2
屈折率(b)	（数字の） 1	1
比透磁率(b)	（数字の） 1	1

(a) 量濃度（amount concentration）は臨床化学の分野では物質濃度（substance concentration）ともよばれる。
(b) これらは無次元量あるいは次元１をもつ量であるが、そのことを表す単位記号である数字の１は通常は表記しない。

表３．固有の名称と記号で表されるSI組立単位

組立量	SI 組立単位			
	名称	記号	他のSI単位による表し方	SI基本単位による表し方
平面角	ラジアン(b)	rad	1 (b)	m/m
立体角	ステラジアン(b)	sr(c)	1 (b)	m^2/m^2
周波数	ヘルツ(d)	Hz		s^{-1}
力	ニュートン	N		m kg s^{-2}
圧力，応力	パスカル	Pa	N/m^2	m^{-1} kg s^{-2}
エネルギー，仕事，熱量	ジュール	J	N m	m^2 kg s^{-2}
仕事率，工率，放射束	ワット	W	J/s	m^2 kg s^{-3}
電荷，電気量	クーロン	C		s A
電位差（電圧），起電力	ボルト	V	W/A	m^2 kg s^{-3} A^{-1}
静電容量	ファラド	F	C/V	m^{-2} kg^{-1} s^4 A^2
電気抵抗	オーム	Ω	V/A	m^2 kg s^{-3} A^{-2}
コンダクタンス	ジーメンス	S	A/V	m^{-2} kg^{-1} s^3 A^2
磁束	ウエーバ	Wb	Vs	m^2 kg s^{-2} A^{-1}
磁束密度	テスラ	T	Wb/m^2	kg s^{-2} A^{-1}
インダクタンス	ヘンリー	H	Wb/A	m^2 kg s^{-2} A^{-2}
セルシウス温度	セルシウス度(e)	℃		K
光束	ルーメン	lm	cd sr(c)	cd
照度	ルクス	lx	lm/m^2	m^{-2} cd
放射性核種の放射能(f)	ベクレル(d)	Bq		s^{-1}
吸収線量, 比エネルギー分与, カーマ	グレイ	Gy	J/kg	m^2 s^{-2}
線量当量, 周辺線量当量, 方向性線量当量, 個人線量当量	シーベルト(g)	Sv	J/kg	m^2 s^{-2}
酸素活性	カタール	kat		s^{-1} mol

(a)SI接頭語は固有の名称と記号を持つ組立単位と組み合わせても使用できる。しかし接頭語を付した単位はもはやコヒーレントではない。
(b)ラジアンとステラジアンは数字の１に対する単位の特別な名称で、量についての情報をつたえるために使われる。実際には、使用する時には記号radおよびsrが用いられるが、習慣として組立単位としての記号である数字の１は明示されない。
(c)測光学ではステラジアンという名称と記号srを単位の表し方の中に、そのまま維持している。
(d)ヘルツは周期現象についてのみ、ベクレルは放射性核種の統計的過程についてのみ使用される。
(e)セルシウス度はケルビンの特別な名称で、セルシウス温度を表すために使用される。セルシウス度とケルビンの単位の大きさは同一である。したがって、温度差や温度間隔を表す数値はどちらの単位で表しても同じである。
(f)放射性核種の放射能（activity referred to a radionuclide）は、しばしば誤った用語で"radioactivity"と記される。
(g)単位シーベルト（PV,2002,70,205）についてはCIPM勧告2（CI-2002）を参照。

表４．単位の中に固有の名称と記号を含むSI組立単位の例

組立量	SI 組立単位		
	名称	記号	SI 基本単位による表し方
粘度	パスカル秒	Pa s	m^{-1} kg s^{-1}
力のモーメント	ニュートンメートル	N m	m^2 kg s^{-2}
表面張力	ニュートン毎メートル	N/m	kg s^{-2}
角速度	ラジアン毎秒	rad/s	m m^{-1} s^{-1}=s^{-1}
角加速度	ラジアン毎秒毎秒	rad/s^2	m m^{-1} s^{-2}=s^{-2}
熱流密度，放射照度	ワット毎平方メートル	W/m^2	kg s^{-3}
熱容量，エントロピー	ジュール毎ケルビン	J/K	m^2 kg s^{-2} K^{-1}
比熱容量，比エントロピー	ジュール毎キログラム毎ケルビン	J/(kg K)	m^2 s^{-2} K^{-1}
比エネルギー	ジュール毎キログラム	J/kg	m^2 s^{-2}
熱伝導率	ワット毎メートル毎ケルビン	W/(m K)	m kg s^{-3} K^{-1}
体積エネルギー	ジュール毎立方メートル	J/m^3	m^{-1} kg s^{-2}
電界の強さ	ボルト毎メートル	V/m	m kg s^{-3} A^{-1}
電荷密度	クーロン毎立方メートル	C/m^3	m^{-3} sA
表面電荷	クーロン毎平方メートル	C/m^2	m^{-2} sA
電束密度，電気変位	クーロン毎平方メートル	C/m^2	m^{-2} sA
誘電率	ファラド毎メートル	F/m	m^{-3} kg^{-1} s^4 A^2
透磁率	ヘンリー毎メートル	H/m	m kg s^{-2} A^{-2}
モルエネルギー	ジュール毎モル	J/mol	m^2 kg s^{-2} mol^{-1}
モルエントロピー, モル熱容量	ジュール毎モル毎ケルビン	J/(mol K)	m^2 kg s^{-2} K^{-1} mol^{-1}
照射線量（X線及びγ線）	クーロン毎キログラム	C/kg	kg^{-1} sA
吸収線量率	グレイ毎秒	Gy/s	m^2 s^{-3}
放射強度	ワット毎ステラジアン	W/sr	m^4 m^{-2} kg s^{-3}=m^2 kg s^{-3}
放射輝度	ワット毎平方メートル毎ステラジアン	$W/(m^2$ sr)	m^2 m^{-2} kg s^{-3}=kg s^{-3}
酵素活性濃度	カタール毎立方メートル	kat/m^3	m^{-3} s^{-1} mol

表５．SI 接頭語

乗数	接頭語	記号	乗数	接頭語	記号
10^{24}	ヨタ	Y	10^{-1}	デシ	d
10^{21}	ゼタ	Z	10^{-2}	センチ	c
10^{18}	エクサ	E	10^{-3}	ミリ	m
10^{15}	ペタ	P	10^{-6}	マイクロ	μ
10^{12}	テラ	T	10^{-9}	ナノ	n
10^9	ギガ	G	10^{-12}	ピコ	p
10^6	メガ	M	10^{-15}	フェムト	f
10^3	キロ	k	10^{-18}	アト	a
10^2	ヘクト	h	10^{-21}	ゼプト	z
10^1	デカ	da	10^{-24}	ヨクト	y

表６．SIに属さないが、SIと併用される単位

名称	記号	SI 単位による値
分	min	1 min=60s
時	h	1h =60 min=3600 s
日	d	1 d=24 h=86 400 s
度	°	1°=(π/180) rad
分	’	1’=(1/60)°=(π/10800) rad
秒	”	1”=(1/60)’=(π/648000) rad
ヘクタール	ha	$1ha=1hm^2=10^4m^2$
リットル	L, l	$1L=11=1dm^3=10^3cm^3=10^{-3}m^3$
トン	t	$1t=10^3$ kg

表７．SIに属さないが、SIと併用される単位で、SI単位で表される数値が実験的に得られるもの

名称	記号	SI 単位で表される数値
電子ボルト	eV	$1eV=1.602\ 176\ 53(14)\times10^{-19}J$
ダルトン	Da	$1Da=1.660\ 538\ 86(28)\times10^{-27}kg$
統一原子質量単位	u	1u=1 Da
天文単位	ua	$1ua=1.495\ 978\ 706\ 91(6)\times10^{11}m$

表８．SIに属さないが、SIと併用されるその他の単位

名称	記号	SI 単位で表される数値
バール	bar	1 bar=0.1MPa=100kPa=10^5Pa
水銀柱ミリメートル	mmHg	1mmHg=133.322Pa
オングストローム	Å	1 Å=0.1nm=100pm=10^{-10}m
海里	M	1 M=1852m
バーン	b	$1\ b=100fm^2=(10^{-12}cm)2=10^{-28}m^2$
ノット	kn	1 kn=(1852/3600)m/s
ネーパ	Np	SI単位との数値的な関係は、対数量の定義に依存。
ベル	B	
デジベル	dB	

表９．固有の名称をもつCGS組立単位

名称	記号	SI 単位で表される数値
エルグ	erg	$1\ erg=10^{-7}$ J
ダイン	dyn	$1\ dyn=10^{-5}$N
ポアズ	P	1 P=1 dyn s cm^{-2}=0.1Pa s
ストークス	St	1 St =$1cm^2$ s^{-1}=$10^{-4}m^2$ s^{-1}
スチルブ	sb	1 sb =1cd cm^{-2}=10^4cd m^{-2}
フォト	ph	1 ph=1cd sr cm^{-2} 10^4lx
ガル	Gal	1 Gal =1cm s^{-2}=$10^{-2}ms^{-2}$
マクスウェル	Mx	1 Mx = 1G cm^2=10^{-8}Wb
ガウス	G	1 G =1Mx cm^{-2} =10^{-4}T
エルステッド(c)	Oe	1 Oe≙ $(10^3/4\pi)$A m^{-1}

(c) ３元系のCGS単位系とSIでは直接比較できないため、等号「 ≙ 」は対応関係を示すものである。

表10．SIに属さないその他の単位の例

名称	記号	SI 単位で表される数値
キュリー	Ci	$1\ Ci=3.7\times10^{10}Bq$
レントゲン	R	$1\ R = 2.58\times10^{-4}C/kg$
ラド	rad	$1\ rad=1cGy=10^{-2}Gy$
レム	rem	$1\ rem=1\ cSv=10^{-2}Sv$
ガンマ	γ	1γ=1 nT=10-9T
フェルミ		1フェルミ=1 fm=10-15m
メートル系カラット		1メートル系カラット = 200 mg = 2×10-4kg
トル	Torr	1 Torr = (101 325/760) Pa
標準大気圧	atm	1 atm = 101 325 Pa
カロリー	cal	1cal=4.1858J（「15℃」カロリー），4.1868J（「IT」カロリー）4.184J（「熱化学」カロリー）
ミクロン	μ	1 μ =1μm=10^{-6}m

（第8版，2006年改訂）

この印刷物は再生紙を使用しています